Università degli Studi di Padova

DIPARTIMENTO DI TECNICA E GESTIONE DEI SISTEMI INDUSTRIALI
Corso di Laurea Magistrale in Ingegneria Meccatronica

Tesi di Laurea Magistrale

Analysis and Design of Synchronous Motors for Exoskeleton Joints

Candidato:
Daniele De Gregorio
Matricola 2058883

Relatore:
Prof. Nicola Bianchi

Correlatrice:
Dott.ssa Chiara Contò

Anno Accademico 2023–2024

Sommario

Gli Esoscheletri per gli arti inferiori sono dispositivi di supporto per persone che, a causa dell'età o di infortuni, soffrono di ridotta mobilità. Essi possono essere principalmente divisi in due tipi: Assistivi e di Supporto. Gli Esoscheletri Assistivi hanno la potenza necessaria per aiutare una persona con ridotta mobilità o forza a compiere alcuni movimenti di routine, mentre gli Esoscheletri di Supporto hanno abbastanza potenza per implementare il completo movimento e aiutare persone che altrimenti non potrebbero stare in piedi o camminare.

Un Esoscheletro è "un dispositivo robotico indossabile in grado di fornire coppia alle articolazioni per controllare o assistere i movimenti dell'utente". La parte fondamentale di un Esoscheletro è infatti l'attuatore dell'articolazione, composto da un Motore Elettrico, una Trasmissione Meccanica e una Scheda di Controllo.

Lo scopo di questo lavoro è quello di provare a migliorare o trovare soluzioni alternative per l'integrazione del Motore Elettrico nell'attuatore. La ricerca è condotta studiando diverse topologie di motori e confrontandole per raggiungere il miglior risultato possibile in termini di prestazioni. Il focus principale è sulla coppia di picco del motore (e dell'attuatore) e sul peso totale e le dimensioni (principalmente assiali) dell'articolazione risultante.

Tra le diverse soluzioni, quelle con le prestazioni migliori sono i Motori Sincroni a Magneti Permanenti Superficiali a Rotore Esterno e le Macchine di Vernier a Magneti Permanenti a Rotore Esterno.

Abstract

Lower-Limb Exoskeletons are supporting devices for people who, due to age or injury, suffer from reduced gait mobility. They can be mainly divided in two different types: Assistive and Supportive. Assistive Exoskeletons have as much power as it is needed to help a person with reduced mobility or strength perform some routine movements, instead Supportive Exoskeletons have enough power to implement full movement and help people who could not stand or walk otherwise.

An Exoskeleton is "a wearable robotic device capable of providing joint torque to control or assist user motions". The fundamental part of an Exoskeleton is indeed the Joint Actuator which is composed of an Electric Motor, a Mechanical Transmission and a Control Board.

The goal of this work is to try and upgrade or find different solutions for the integration of an Electric Motor in the actuator. Research is carried out by studying different motor topologies and comparing them to reach the best result possible performance wise. Main focus is on the peak output torque of the motor (and of the actuator) and on the total weight and size (mainly axial) of the resulting joint.

Among different solutions, the best performing ones are Outer Rotor Superficial Permanent Magnet Motors and Outer Rotor Permanent Magnet Vernier Machines.

Contents

List of Figures i

List of Tables iii

1 Introduction 1

1.1 Lower-Limb Exoskeleton Devices 1
1.2 Exoskeleton Applications 1
1.2.1 Industry and Military 1
1.2.2 Healthcare 3
1.3 Engineering Challenges 4
1.4 Structure of a Joint Actuator 4
1.4.1 Preliminary Joint Actuator Design 5
1.4.2 Desired Joint Actuator Improvements 7
1.5 Thesis Outline 8

2 Permanent Magnet Machines 9

2.1 Permanent Magnet Synchronous Machines 9
2.1.1 Permanent Magnet Materials 9
2.1.2 Permanent Magnet Machine Types 10
2.1.3 Permanent Magnet Machine Design 10
2.1.4 Permanent Magnet Machine Winding Design 11
2.1.5 Fractional Slot Concentrated Winding Machines 14
2.1.6 Permanent Magnet Machine Model and Control 15
2.2 Permanent Magnet Machines with Magnetic Gearing Effect 17
2.2.1 Permanent Magnet Magnetically Geared Machines 18
2.2.2 Permanent Magnet Vernier Machines 19

3 Analysis and Design of Outer Rotor SPM Motors 21

3.1 Flipsky 6354 Analysis 21
3.1.1 Flipsky 6354 Drawing 23
3.1.2 Flipsky 6354 FEA 24
3.2 Outer Rotor SPM Motor Prototypes 29

3.2.1 1214 MkI: 12 slots 14 poles with stack length reduction 29
3.2.2 3624 MkI: 3/2 configuration 35
3.2.3 1214 MkII: 12 slots 14 poles with halbach configuration 41
3.3 Outer Rotor SPM Motors Comparison 46
3.4 Lightweight SPM Motor Design 48
3.4.1 2428 MkI Design 48
3.4.2 2428 MkI Analysis 52

4 Analysis and Design of Outer Rotor Vernier Motors 57
4.1 SPM and Vernier Analysis and Comparison 57
4.2 Outer Rotor Vernier Motor Prototypes 64
4.2.1 1238 MkI: Vernier Machine without flux modulator 64
4.2.2 1270 MkI: Vernier Machine with flux modulator 69
4.3 Vernier Motors Comparison 74
4.4 Lightweight Vernier Motor Design 76

Conclusions 81

Appendix A: Axial Flux Machines 85
Slotless Axial Flux Analytical Design 85
Slotted Axial Flux Analytical Design 86

Appendix B: Materials 89

Bibliography 91

List of Figures

1.1 Lower-Limb Exoskeleton applications **(a)** Industrial **(b)** Military . . 2
1.2 Lower-Limb Exoskeleton healthcare commercial applications **(a)** ReWalk **(b)** Ekso 2
1.3 **(a)** Laifual LSG-20 Harmonic Drive **(b)** Flipsky 6354 motor 6
1.4 Detailed view of the Powered Joint designed in [8] **1)** Motor **2)** Harmonic Drive **3)** Washer **4)** Holding screw **5)** Key **6)** Spacer ring **7)** Coupling flange 7
1.5 Side view of the total preliminary joint designed in [8] 7

2.1 PM rotors types **(a)** SPM **(b)** IPM **(c)** Spoke 10
2.2 $Q_s = 24$ and $2p = 4$ **(a)** Star of slots **(b)** Winding scheme 12
2.3 $Q_s = 12$ and $2p = 14$ **(a)** Star of slots **(b)** Winding scheme 12
2.4 Star of slots of a $Q_s = 12$ and $2p = 10$ machine with resulting double-layer Fractional Slot Concentrated Winding [10] 14
2.5 Fractional Slot Concentrated Winding Motors [11] **(a)** Single-layer **(b)** Double-Layer 14
2.6 High torque dense magnetic gears [13] **(a)** Concentric **(b)** Harmonic **(c)** Planetary 17
2.7 Magnetically Geared Machines [14] **(a)** Outer Rotor **(b)** Inner Rotor 18
2.8 Vernier Machines [13] **(a)** Outer Rotor PM Vernier Machine **(b)** Outer Rotor PM Vernier Machine with modulator **(c)** Inner Rotor PM Vernier Machine with modulator 19

3.1 Flipsky 6354 catalog drawing 22
3.2 Flipsky 6354 details 22
3.3 Flipsky 6354 drawing 24
3.4 FEA analysis **(a)** No load conditions **(b)** FOC Overload conditions . 25
3.5 No load induction **(a)** Zero and First order harmonics comparison **(b)** Harmonic spectrum 25
3.6 No load fluxes **(a)** In abc reference frame **(b)** In dq reference frame . 26
3.7 MTPA in nominal and overload conditions 26

3.8 **(a)** Cogging torque **(b)** Torque ripple in nominal conditions 27
3.9 Current range up to $1.5 \cdot I_n$ **(a)** Flux linkage with current vector on d-axis **(b)** Flux linkage with current vector on q-axis 28
3.10 1214 MkI drawing 30
3.11 FEA analysis **(a)** No load conditions **(b)** FOC Overload conditions . 30
3.12 No load induction **(a)** Zero and First order harmonics comparison **(b)** Harmonic spectrum 31
3.13 No load fluxes **(a)** In abc reference frame **(b)** In dq reference frame . 31
3.14 MTPA in nominal and overload conditions 32
3.15 **(a)** Cogging torque **(b)** Torque ripple in nominal conditions 33
3.16 Current range up to $1.5 \cdot I_n$ **(a)** Flux linkage with current vector on d-axis **(b)** Flux linkage with current vector on q-axis 33
3.17 3624 MkI drawing 36
3.18 FEA analysis **(a)** No load conditions **(b)** FOC Overload conditions . 37
3.19 No load induction **(a)** Zero and First order harmonics comparison **(b)** Harmonic spectrum 37
3.20 No load fluxes **(a)** In abc reference **(b)** In dq reference 38
3.21 MTPA in nominal and overload conditions 38
3.22 **(a)** Cogging torque **(b)** Torque ripple in nominal conditions 39
3.23 Current range up to $1.5 \cdot I_n$ **(a)** Flux linkage with current vector on d-axis **(b)** Flux linkage with current vector on q-axis 40
3.24 Halbach magnets disposition 41
3.25 Halbach mangets disposition for an Outer Rotor Motor 41
3.26 1214 MkII drawing 42
3.27 FEA analysis **(a)** No load conditions **(b)** FOC Overload conditions . 42
3.28 No load induction **(a)** Zero and First order harmonics comparison **(b)** Harmonic spectrum 43
3.29 No load fluxes **(a)** In abc reference **(b)** In dq reference 43
3.30 MTPA in nominal and overload conditions 44
3.31 **(a)** Cogging torque **(b)** Torque ripple in nominal conditions 44
3.32 Current range up to $1.5 \cdot I_n$ **(a)** Flux linkage with current vector on d-axis **(b)** Flux linkage with current vector on q-axis 45
3.33 dq torque comparison of SPM Outer Rotor Motors designed 46
3.34 2428 MkI drawing 48
3.35 FEA analysis **(a)** No load conditions **(b)** FOC Overload conditions . 49
3.36 No load induction **(a)** Zero and First order harmonics comparison **(b)** Harmonic spectrum 49
3.37 MTPA in nominal and overload conditions 50
3.38 **(a)** Cogging torque **(b)** Torque ripple in nominal conditions 50

3.39 No load fluxes **(a)** In abc reference **(b)** In dq reference 51
3.40 Mechanical characteristics reached in nominal current conditions . . . 51
3.41 **(a)** Torque map in [Nm] **(b)** Current density map in $\left[\frac{\text{A}}{\text{mm}^2}\right]$ 52
3.42 Losses map in [W] **(a)** Iron **(b)** Joule **(a)** Total 53
3.43 Torque versus speed characteristics in both nominal and overload conditions 54
3.44 Power versus speed characteristics in both nominal and overload conditions 54
3.45 Currents versus speed characteristics in both nominal and overload conditions 55
3.46 Current trajectory of MTPA in both nominal and overload conditions 55
3.47 Efficiency map 56

4.1 **(a)** 3612 MkI SPM Motor with overlapped winding **(b)** 3660 MkI Vernier Machine with overlapped winding 58
4.2 Teeth and magnets detail **(a)** 3612 MkI SPM Motor with overlapped winding **(b)** 3660 MkI Vernier Machine with overlapped winding . . 58
4.3 FEA analysis in FOC overload conditions **(a)** 3612 MkI **(b)** 3660 MkI 59
4.4 No load induction of 3612 MkI **(a)** Zero and First order harmonics comparison **(b)** Harmonic spectrum 59
4.5 No load induction of 3660 MkI **(a)** Zero and First order harmonics comparison **(b)** Harmonic spectrum 60
4.6 MTPA comparison of 3612 MkI and 3660 MkI in nominal conditions . 60
4.7 MTPA comparison of 3612 MkI and 3660 MkI in overload conditions 61
4.8 Electric loading harmonics of $Q_s = 36$ and $2p = 12$ winding 62
4.9 Harmonics and subharmonics of 3660 MkI in overload conditions . . . 62
4.10 Harmonics and subharmonics of 3660 MkI in different electric and magnetic load conditions 63
4.11 1238 MkI drawing 64
4.12 FEA analysis **(a)** No load conditions **(b)** FOC Overload conditions . 65
4.13 No load induction **(a)** Zero and First order harmonics comparison **(b)** Harmonic spectrum 65
4.14 MTPA in nominal conditions and overload conditions 66
4.15 Electric loading harmonics of a $Q_s = 12$ and $2p = 14$ winding 66
4.16 **(a)** Cogging torque **(b)** Torque ripple in nominal conditions 67
4.17 Harmonics and subharmonics of 1238 MkI in overload conditions . . . 67
4.18 Harmonics and subharmonics of 1238 MkI in different electric and magnetic load conditions 68
4.19 1270 MkI drawing 69
4.20 FEA analysis **(a)** No load conditions **(b)** FOC Overload conditions . 70

4.21 No load induction **(a)** Zero and First order harmonics comparison **(b)** Harmonic spectrum 70
4.22 MTPA in nominal conditions and overload conditions 71
4.23 **(a)** Cogging torque **(b)** Torque ripple in nominal conditions 71
4.24 Harmonics and subharmonics of 1270 MkI in overload conditions . . . 72
4.25 Harmonics and subharmonics of 1270 MkI in different electric and magnetic load conditions 72
4.26 dq torque comparison of designed Vernier Outer Rotor Motors 74
4.27 1238 MkII drawing 76
4.28 FEA analysis **(a)** No load conditions **(b)** FOC Overload conditions . 77
4.29 No load induction **(a)** Zero and First order harmonics comparison **(b)** Harmonic spectrum 77
4.30 MTPA in nominal and overload conditions 78
4.31 **(a)** Cogging torque **(b)** Torque ripple in nominal conditions 78
4.32 No load fluxes **(a)** In abc reference **(b)** In dq reference 79
4.33 Mechanical characteristics reached in nominal current conditions . . . 79

List of Tables

1.1 Maximum absolute joint torque for a healthy 80 kg, 180 cm person reported in [9] . . . 5
1.2 Harmonic Drive datasheet features . . . 6
1.3 Motor datasheet features . . . 6

3.1 Size of Flipsky 6354 . . . 21
3.2 Flipsky 6354 datasheet features . . . 21
3.3 Stator dimentions of Flipsky 6354 . . . 24
3.4 Stator dimensions of 1214 MkI . . . 29
3.5 Size of 1214 MkI . . . 29
3.6 Stator dimensions of 3624 MkI . . . 36
3.7 Size of 3624 MkI . . . 36
3.8 Stator dimensions of 1214 MkII . . . 41
3.9 Size of 1214 MkII . . . 42
3.10 SPM Outer Rotor Motors Designed Comparison . . . 47
3.11 Stator dimensions of 2428 MkI . . . 48
3.12 Size of 2428 MkI . . . 48

4.1 Stator dimensions of 3612 MkI . . . 57
4.2 Size of 3612 MkI . . . 58
4.3 Stator dimensions of 3660 MkI . . . 58
4.4 Size of 3660 MkI . . . 59
4.5 Stator dimensions of 1238 MkI . . . 64
4.6 Size of 1238 MkI . . . 64
4.7 Stator dimensions of 1270 MkI . . . 69
4.8 Size of 1270 MkI . . . 69
4.9 Designed Vernier Outer Rotor Machines Comparison . . . 74
4.10 Stator dimensions of 1238 MkII . . . 76
4.11 Size of 1238 MkII . . . 76
4.12 Resulting Joint Actuator Sizes Comparison . . . 82

Chapter 1

Introduction

1.1 Lower-Limb Exoskeleton Devices

An Exoskeleton is a wearable robotic device capable of improving or enhancing the mobility, strength and stamina of a human being [1]. More precisely, an Exoskeleton is a wearable mechanism able to implement limbs motion through the power supplied by the actuators, which are controlled through electronic boards that receive data from feedback sensors. In general, Exoskeletons can be built to help a user with motion of upper or lower limbs. Robotic Exoskeletons for both upper and lower limbs have the potential to enhance human capabilities in healthy individuals, aid movement for those with neurological impairments, or deliver therapeutic interventions for individuals with neurological disabilities. The devices that assist the motion of the lower part of human body are generally referred to as Lower-Limb Exoskeletons (LLEs).

1.2 Exoskeleton Applications

Exoskeletons are devices that can be used in a wide range of applications in military, industrial and, more importantly, healthcare.

1.2.1 Industry and Military

Manual material handling in industrial settings includes lifting, lowering, and carrying heavy items. These actions impose significant strain on the lumbar spine, increasing the likelihood of lower-back injuries. Work-related injuries not only incur substantial industrial costs but also severely impact the quality of life for workers. Several prototypes of lower-back Exoskeletons have been developed to offer back support to industrial workers engaged in manual handling of heavy materials. It

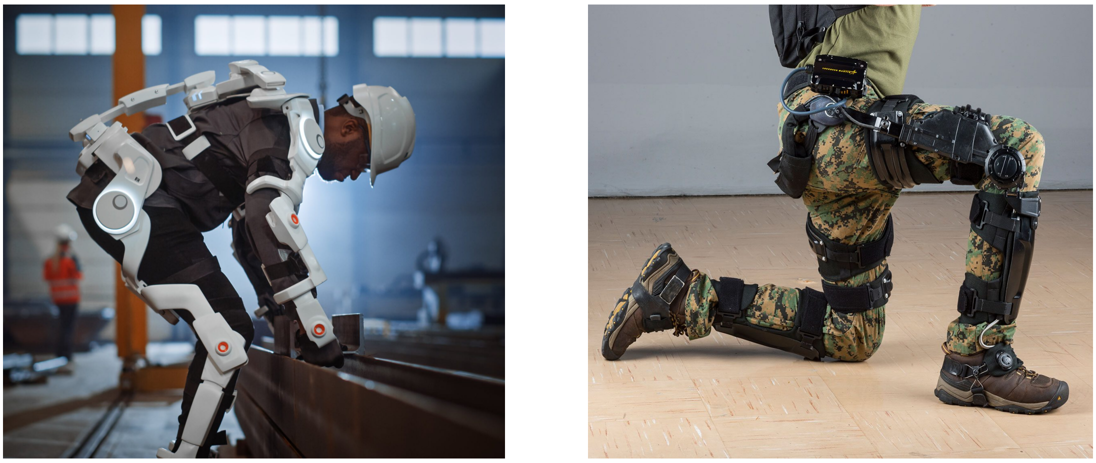

(a) (b)

Figure 1.1: Lower-Limb Exoskeleton applications **(a)** Industrial **(b)** Military

has been demonstrated that the risk of work-related back injuries can be reduced by alleviating spinal loads during these tasks. Most existing back-support Exoskeletons generate supportive forces between the torso and thighs to minimize muscular strain in the lower back and reduce the risk of associated injuries. Designs incorporating Series Elastic Actuators (SEAs) have been suggested for such purposes (e.g. [2], [3]).

While Industrial Exoskeletons primarily aim to enhance human capabilities and prevent injuries during repetitive tasks (Figure 1.1(a)), military-grade Exoskeletons focus on improving strength and reducing fatigue for soldiers that are carrying heavy loads over extended distances. An example may be ONYX, developed by Lockheed Martin and shown in Figure 1.1(b).

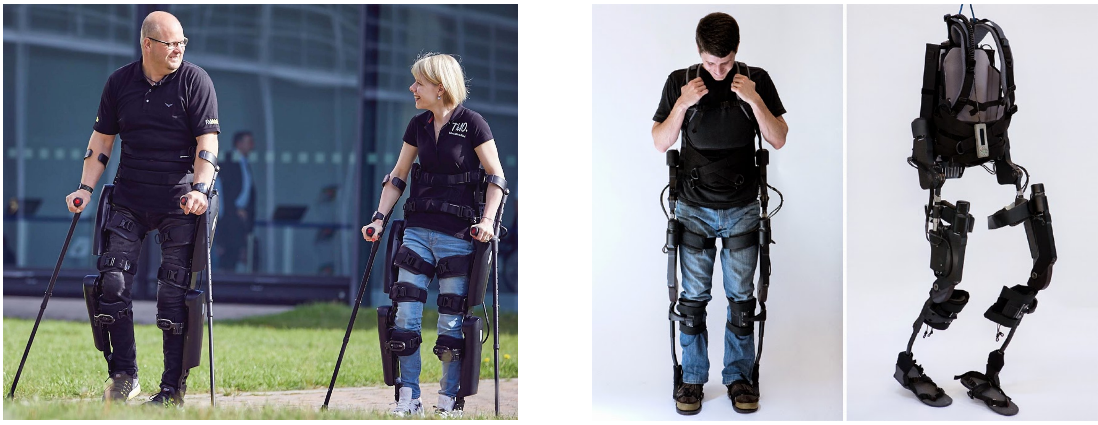

(a) (b)

Figure 1.2: Lower-Limb Exoskeleton healthcare commercial applications **(a)** ReWalk **(b)** Ekso

1.2.2 Healthcare

Despite the increasing importance of industrial applications for Exoskeletons, which can prevent injuries and guarantee a better quality of work for those who have wearing jobs, the most important application of Powered Exoskeletons is the medical one.

Cerebral Palsy, Spina Bifida, and Spinal Cord Injury are main causes of motor function disabilities in children. Conditions such as stroke and neuromusculoskeletal dysfunctions like tetraplegia, cerebral palsy, muscular dystrophy, and amyotrophic lateral sclerosis disrupt limb movement in adults, causing reduced range of motion and diminished strength in affected limbs. Apart from them, the constant aging of the population is an another reason for gait impairment presence.

Medical Lower-Limb Exoskeletons offer the potential to regain walking ability and provide therapeutic exercise to address physical challenges. Powered lower limb orthoses, or Exoskeletons, have been designed to aid in the rehabilitation of individuals with gait impairments. These devices alleviate physical strain on therapists, increase the repeatability of walking tasks through robotic precision, and often result in more productive therapy sessions for patients.

Although research on powered mobility or rehabilitation is not extremely large, recent studies on progressive resistance exercises for adolescents with MMC have shown improvements in gait speed, improved performance on functional tests, better walking and standing abilities, enhanced hip kinematics, reduced metabolic cost of walking, correction of gait abnormalities, and postural improvements, comparable to outcomes seen with orthopedic surgery, despite neurological impairments. For this reason, there has been a surge in powered devices and research into the benefits of Robotic Assisted Gait Therapy, as it is reported in [4]. In addition, Exoskeletons can facilitate mobility and walking assistance outside of the therapy sessions, as shown in Figure 1.2.

Due to the diversity of mobility disorders among patients, medical Exoskeletons face unique challenges compared to consumer and industrial ones. Addressing these challenges requires tailored design approaches. One approach involves body weight support systems combined with a treadmill to ensure safety for individuals lacking lower limb strength, although their large size limits use to rehabilitation centers and hospitals. Alternatively, another design approach shifts all weight to the ground, offering certain advantages but requiring additional stability measures, such as therapist assistance or integrated balance control.

An another important aspect of Exoskeletons in rehabilitation or medical applications is merely linked to the cost of such devices. As reported in [5] apart from weight, assistance and capability problems of commercial Exoskeletons, cost is probably the most repulsive feature for both privates and public hospitals. If Exoskeletons are so expensive, nobody can afford to buy and employ them.

1.3 Engineering Challenges

Exoskeletons should be engineered to optimize assistive torque while minimizing mass. In this way torque density is maximized. Both mass and maximum assistance of an Exoskeleton depend significantly on the Exoskeleton Actuator. Thus, a fundamental tradeoff exists between the mass of a Powered Exoskeleton and the assistance it can offer to the user. A heavier actuator is capable of achieving a greater assistance, so the problem is maximizing the assistance while minimizing the mass. Experiments suggest minimizing the mass of the Exoskeleton and positioning it proximally to the trunk mitigates the negative weight impact. However, this solution entails additional transmission elements like cables or parallelograms to transfer assistance from the actuators to the joints of the user. Consequently, locating actuators on the trunk often leads to increased mass and reduced efficiency. Thus, Exoskeletons with trunk-located ctuators do not necessarily yield superior outcomes compared to those with actuators on the user's legs.

Researchers suggest employing custom motors and gearboxes with relatively low transmission ratios. These actuators are typically compact, lightweight, and quiet but offer relatively low torque, in the range of 12–20 Nm. In many researches, elastic elements have been incorporated in series with geared motors to obtain higher maximum torque (i.e. 30–90 Nm), without worsening output impedance. Series Elastic Actuators (SEAs) can achieve remarkable efficiency and mechanical power output while reducing actuator impedance and enhancing intrinsic safety. In addition, SEAs can serve as reliable and precise torque sensors. The main drawback is that SEAs need additional actuation and sensing components, often resulting in heavier Powered Exoskeletons. Therefore, Powered Exoskeletons with elastic elements do not necessarily exhibit higher torque density than those without elastic elements.

1.4 Structure of a Joint Actuator

From a functional standpoint, the fundamental part of the Exoskeleton is the Joint Actuator, composed of some sort of Electric Motor and Mechanical Transmission (e.g. [6] [7]). It is the active part of the Exoskeleton, with the task to apply torque on the joints to be assisted. The combination of the torque generated by the motor and the mechanical advantage produced by the Mechanical Transmission allows to act on the joint with the torque needed to sustain human gait.

Motors used for Exoskeleton applications must be torque-dense, reliable and com-

pact whereas they do not need an high flux-weakening capability. For these reasons, Permanent Magnet Motors are the most suitable solution.
The Mechanical Transmission part is a more complex choice. In fact, many transmission topologies may be decent and sensible solutions for the Joint Actuator problem. Among them Planetary Gearboxes, Cycloidal Drives and Harmonic Drives. Therefore, the choice is usually constrained by the working cycles of the single specific Exoskeleton.

1.4.1 Preliminary Joint Actuator Design

In [8] a rigid and supportive Lower-Limb Exoskeleton is designed. The Joint Actuators are located both on the hips and on the knees of the user, whereas the feet joints are not actuated and so they are passive, both to reduce the total weight and cost of the Exoskeleton and not to complicate too much the design.
The designed Joint Actuators must produce enough torque to support and assist gait cycle in a normal weight adult. The mentioned demanded torques are displayed in Table 1.1. Each joint is powered by the same Joint Actuator which is designed using a Permanent Magnet Synchronous Motor and an Harmonic Drive transmission.

Task [Nm]	Hip max.	Knee max.	Ankle max.
level walking	65	40	125
stair ascent	40	90	105
stair descent	50	105	90
sit-to-stand	50	70	45

Table 1.1: Maximum absolute joint torque for a healthy 80 kg, 180 cm person reported in [9]

The Mechanical Transmission chosen is a Harmonic Drive with a gear ratio of 100 and with the features of Table 1.2. An epyciclic gearbox may not have been rigid enough to transmit the torque without falling apart and it would have been too bulky to reach the same performance of the Harmonic gear.
The Electric Motor is a Permanent Magnet Synchronous Motor Flipsky 6354, whose features are summarized in Table 1.3 and are described more into detail in the next Chapters.
Using the datasheets, the total actuator performance can be computed showing a nominal torque of 200 Nm which may rise to a value of 700 Nm exerted on each joint in overload conditions. However, considering the values of Table 1.1, and the peak torque tolerated by the Harmonic Drive shown in Table 1.2, the motor oversize is evident. In addition, the total weight of the actuator reaches a value of 1.62 kg, considering both the motor and the Harmonic Drive and without taking any fittings

Features	Laifual LSG-20
Peak torque [Nm]	191
Peak torque [Nm] (at start/stop)	107
Nominal torque [Nm]	52
Nominal speed [rpm] (at input)	2000
Peak speed [rpm] (at input)	7000
Reducing ratio	100
Weight [kg]	0.98
Price [€]	350
Hole diameter [mm]	8
Dimensions [mm] (radial x axial)	93 x 41

Table 1.2: Harmonic Drive datasheet features

Features	Flipsky 6354
Peak torque [Nm]	7
Nominal torque [Nm]	2
Nominal speed [rpm]	3620
Nominal voltage [V]	24/48
Nominal Power [W]	850
Weight [kg]	0.64
Price [€]	95
Shaft diameter [mm]	8
Dimensions [mm] (radial x axial)	63 x 54

Table 1.3: Motor datasheet features

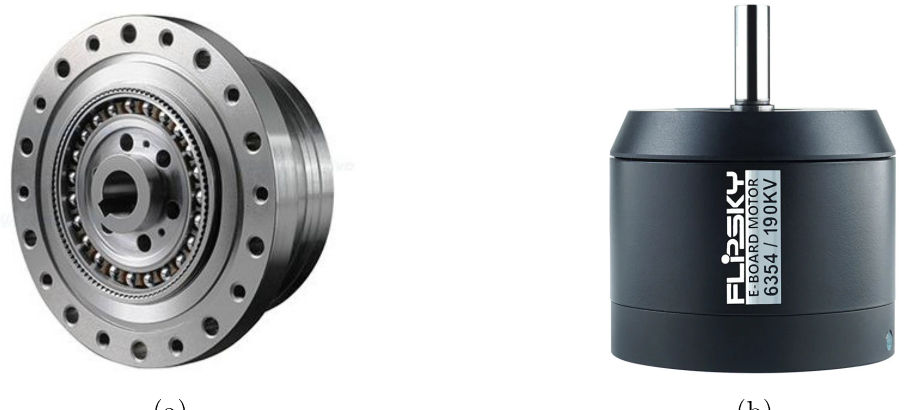

(a) (b)

Figure 1.3: **(a)** Laifual LSG-20 Harmonic Drive **(b)** Flipsky 6354 motor

into consideration. The axial length of the joint is in total equal to 95 mm. Currently the Exoskeleton is being built and tested in the Intelligent Autonomous System Laboratory (IAS-Lab) at the University of Padova.

The integration of the motor, shown in Figure 1.3(a), and the Harmonic Drive, shown in Figure 1.3(b), is displayed in Figure 1.4. In the picture it is possible to

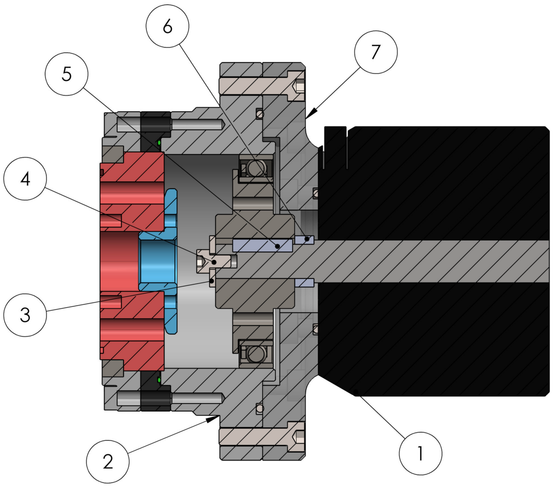

Figure 1.4: Detailed view of the Powered Joint designed in [8] **1)** Motor **2)** Harmonic Drive **3)** Washer **4)** Holding screw **5)** Key **6)** Spacer ring **7)** Coupling flange

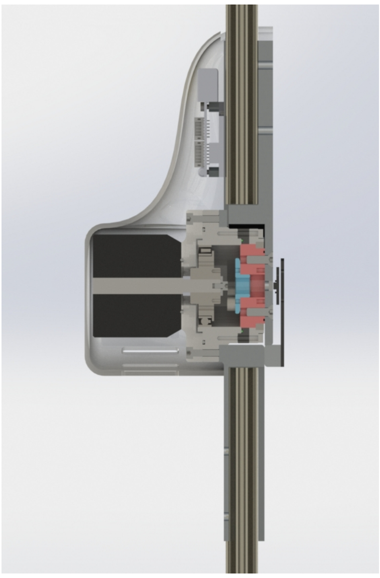

Figure 1.5: Side view of the total preliminary joint designed in [8]

discern every component of the actual mechanical integration between the motor and the reducer such as the key or the coupling flange. Figure 1.5 shows a side view of the total Joint Actuator with the control board and the case.

1.4.2 Desired Joint Actuator Improvements

As it can be seen in Figure 1.4 and Figure 1.5, the biggest improvements are minimizing the axial size of the actuator and its weight. Reducing the axial length of the motor should slightly reduce the axial length of the joint. Reducing the axial size of the motor should reduce the total weight of the actuator as well. Moreover, increasing the weight and power of the motor, it may be interesting to totally remove

the Harmonic Drive using a lighter gearbox as it may reduce the total weight of the joint. However, it is challenging.
Reducing the weight is important because each hip and each knee have to sustain an actuator, meaning that a small weight saved on each joint can make a huge difference in terms of comfort for the user.
From Table 1.1 some requirements to design a tailored motor can be extrapolated. In general, taking into account that the actuator with the 1:100 Harmonic Drive reducer works with a lot of breaklines, it is safe enough to choose functioning torques that can go beyond nominal torque output of the Harmonic Drive, but that stay under the maximum values. A motor with a nominal torque value of 0.8 Nm and an overload torque value of 1.2 Nm delivers enough torque for the main part of the working cycle, allowing also to reach the maximum values of Table 1.1. Basically, considering as the most stressful working point for the actuator the stair descent on the knee with a peak (not continous) of 105 Nm, the maximum torque produced by the Joint Actuator can be 120 Nm, considering a safety margin of approximately 15%.

1.5 Thesis Outline

In Chapter 2 the fundamentals of Electric Machines and in particular Permanent Magnet Machines are briefly explained. Structure, advantages, disadvantages, design features, models and control features are described. In Chapter 3 the analysis of the Flipsky 6354 is reported. From the commercial motor some configurations are derived, designed and anayzed to understand if they meet with the problem requirements. In Chapter 4 a comparison of classic SPM Motors and Vernier Permanent Magnet Machines is carried out. Some Vernier Motors are then designed and analyzed to see if they meet the requirements.

Chapter 2

Permanent Magnet Machines

Permanent Magnet Synchronous Motors (PMSM) are high torque and high power density machines. These motors are composed of a three phase stator that produces a rotating magnetic field able to drag a rotor on which Permanent Magnets are embedded. The magnetic field produced by the stator and the rotor have the same speed and this is the reason why these are called *Synchronous Machines*.
It has to be mentioned that, being these Synchronous Motors, there is the need of an inverter managed by a control system that has to feed the correct tension to the three phases of the motor, otherwise this is not able to move properly.
This kind of motors are thus quite expensive because of Permanent Magnet materials involved and because of the inverter.
Despite being expensive PM Machines have great advantages. Thanks to PM magnetization it is possible to build machines that are efficient, have high power factor and have a high torque and power density. In particular, without the need to excitate the rotor, there is no need for brushes. This is why they are commonly called *Brushless Motors*.

2.1 Permanent Magnet Synchronous Machines

2.1.1 Permanent Magnet Materials

The most common Permanent Magnet materials are Ferrite, NdFeB and SmCo. The first is a Permanent Magnet material used in cheap applications as it is more easy to demagnetize and has a low residual magnetization (about 0.2-0.4 T). The other two instead are more expensive and employed when high torque density and high power density are required. These materials are more difficult to demagnetize and have a high residual magnetization, in the range of 1.1-1.2 T. Dysprosium is usually added to protect Permanent Magnets from high temperatures that could cause demagnetization.

The cost of Permanent Magnet materials is linked to the fact that this high performance magnets are made with rare earths and both their mining and the chemical processes to which they are subjected are quite expensive and, unfortunately, damaging to the environment.

2.1.2 Permanent Magnet Machine Types

Permanent Magnets are put on the rotor in such a way to generate a sinusoidal magnetic field. Thus, they are displaced in a north-south configuration as in Figure 2.1. The number of magnets that are put on the rotor is equal to the number of poles of the motor.
As it can be seen in Figure 2.1, there are different kinds of Permanent Magnet rotors. They are divided by the magnet disposition they have. First of all the Superficial Permanent Magnet rotor (SPM), shown in Figure 2.1(a), where Permanent Magnets are put on the superficial part of the rotor. Then the Interior Permanent Magnet rotor (IPM), in Figure 2.1(b), characterized by PMs inserted in the rotor core. The spoke type rotor where magnetizing direction is along the spokes of the rotor is shown in Figure 2.1(c).

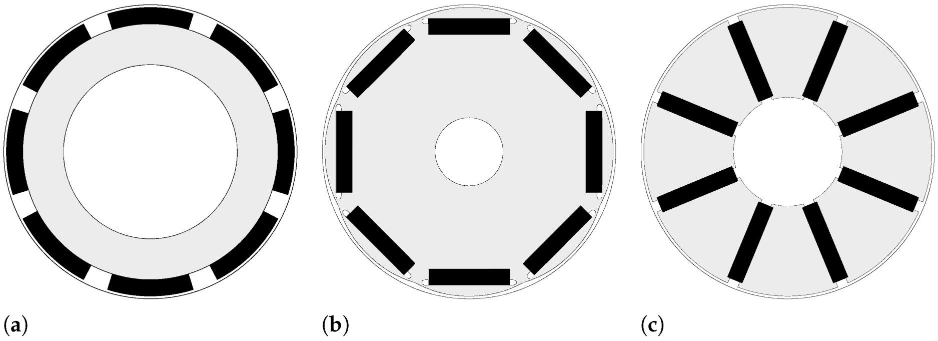

Figure 2.1: PM rotors types **(a)** SPM **(b)** IPM **(c)** Spoke

2.1.3 Permanent Magnet Machine Design

Usually to design any kind of Electric Machine it is useful to begin with some simple analytical equations that allow to carry out a fast and approximated design of the main dimensions. Then the machine geometry can be defined and improved iteratively until a satisfactory performance is reached.
From a design standpoint the machine is approximated as an ideal machine where the stator magnetomotive force is produced by a cosinusoidal distribution of current along the air-gap, the rotor is approximated as a cosinusoidal magnetic field and the permeance of the iron is limitless.
The size of the Electric Machine is related to the amount of torque that it delivers.

With the same absorbed power, a machine with high torque and low speed is larger than a machine with low torque and high speed.
Using the approximations allows, after some steps, to write to electromagnetic torque of the motor as:

$$T_{em} = \frac{\pi}{4} \cdot D_s^2 \cdot L_{stk} \cdot \hat{K}_s \cdot \hat{B}_g \tag{2.1}$$

where D_s is the air-gap diameter, L_{stk} is the stack length of the motor, $\hat{K}_s$ is the electric loading of the machine, related to stator winding field generated by three-phase supply and $\hat{B}_g$ is the air-gap magnetic induction, related to magnetizing flux generated by PMs.
From (2.1) it is possible to highlight that torque depends highly on electric and magnetic loading of the machine. The higher the electric loading of the machine the higher the torque, and the higher the air-gap flux density the higher the torque. Moreover it is easy to see that an important influence on the electromagnetic torque depends on the air-gap volume of the machine. More air-gap volume means an higher torque.
As a consequence increasing the loading of the machine helps to reduce the size of the machine, usually increasing both the iron and the joule losses. Therefore the final design is the result of a tradeoff.

2.1.4 Permanent Magnet Machine Winding Design

A rotating field must be generated to make a Synchronous Machine work. The rotating field, which is produced by the three-phase stator, must have the number of poles of the machine. So the stator winding has to be designed properly.
The design of an Electric Machine winding is carried out by means of the star of slots. It is a diagram of phasors of the electro motive force induced in a conductor of each stator slot. The hyphotesis is that the air-gap flux density is sinusoidal. Each phasor gets the number of the slot in which the corresponding conductor is placed. It is possible to compute the number of slots per pole and phase from the pole pairs of the machine p, the motor number of phases m and the stator slots Q_s.

$$q = \frac{Q_s}{2p \cdot m} \tag{2.2}$$

If a motor has a number of slots per pole and phase that is not an integer the winding is referred to as *fractional slot winding*. An example of both an integral slot winding and a fractional slot winding is displayed in Figure 2.2 and in Figure 2.3.
It is now possible to compute the mechanical slot angle α_s. The electrical slot angle α_s^e can be computed thanks to the mechanical slot angle and the pole pairs of the

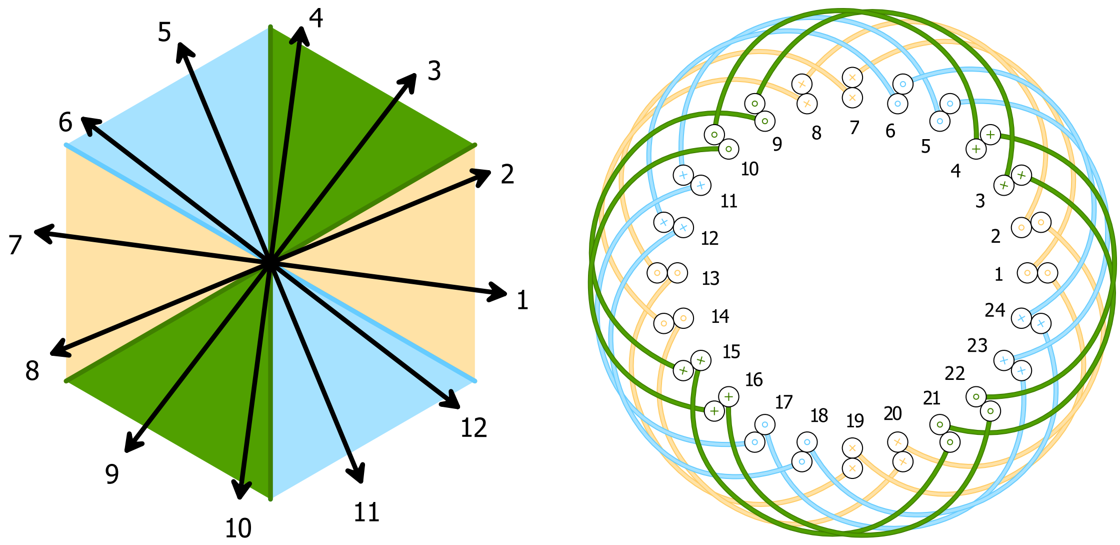
5
4
3
6
2
7
1
8
12
9
11
10
9
8
7
6
5
4
10
3
11
2
12
1
13
24
14
23
15
22
16
21
17
18
19
20

(a) (b)

Figure 2.2: $Q_s = 24$ and $2p = 4$ **(a)** Star of slots **(b)** Winding scheme

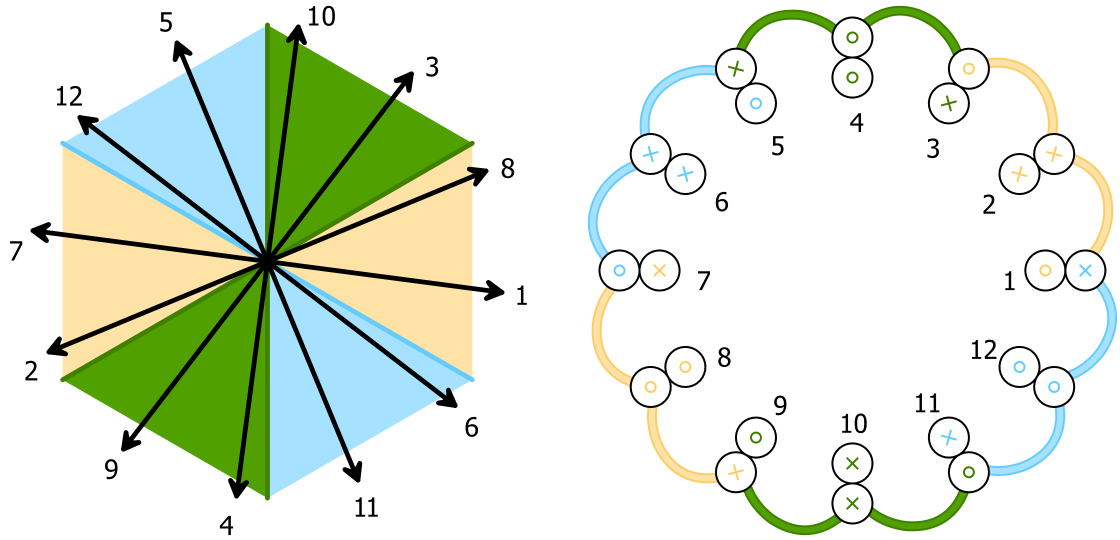
5
10
3
12
8
7
1
2
6
9
11
4
4
5
3
6
2
7
1
8
12
9
10
11

(a) (b)

Figure 2.3: $Q_s = 12$ and $2p = 14$ **(a)** Star of slots **(b)** Winding scheme

motor. It is the angle between two consequent phasors.

$$\alpha_s = \frac{360^\circ}{Q_s} \tag{2.3}$$

$$\alpha_s^e = p \cdot \alpha_s \tag{2.4}$$

The electrical periodicity of the machine can be computed as the greatest common divisor of the number of slots and the pole pairs of the machine. This number describes how many times a same winding pattern is replicated in the totality of the machine.

$$t = G.C.D.\{Q_s, p\} \tag{2.5}$$

The number of phasors is equal to the number of slots, but this phasors are disposed on a number of spokes equal to:

$$\frac{Q_s}{t} \tag{2.6}$$

It is then possible to compute the coil pitch y_q as.

$$y_q = \frac{Q_s}{2p} \tag{2.7}$$

From the obtained values the distribution coefficient k_d can be computed. The distribution coefficient somehow measures the quality of the armature field generated by the designed winding.

$$k_d = \frac{sin\left(q \cdot \frac{\alpha_s^e}{2}\right)}{q \cdot sin\left(\frac{\alpha_s^e}{2}\right)} \tag{2.8}$$

If y_q is greater than 1 (usually it is) it is possible to shorten the winding of an integer number of slots n, this results in a chording of an electrical slot angle β_r^e. With the chording some specific harmonics are eliminated or reduced and a lower copper volume is employed, reducing costs.

$$\beta_r^e = n \cdot \alpha_s^e \tag{2.9}$$

The effect of chording is taken into consideration by using the pitch factor k_p.

$$k_p = cos\left(\frac{\beta_r^e}{2}\right) \tag{2.10}$$

The winding factor k_w is computed from these coefficients. It describes the effect of the winding configuration on torque quality production.

$$k_w = k_d \cdot k_p \tag{2.11}$$

An high winding factor means a higher electric loading, thus a higher torque. In addition an high winding factor implies a lower harmonic content.

2.1.5 Fractional Slot Concentrated Winding Machines

Fractional slot windings are tipically realised with copper conductors wrapped around teeth. Such a winding is called *Fractional Slot Concentrated Winding* (*FSCW*). In particular if all teeth are wound the winding is a double layer winding, otherwise it is a single layer winding.

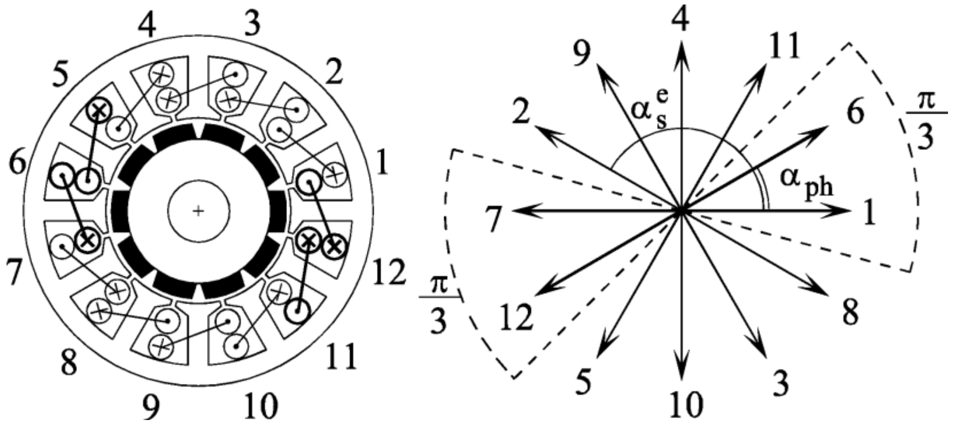

Figure 2.4: Star of slots of a $Q_s = 12$ and $2p = 10$ machine with resulting double-layer Fractional Slot Concentrated Winding [10]

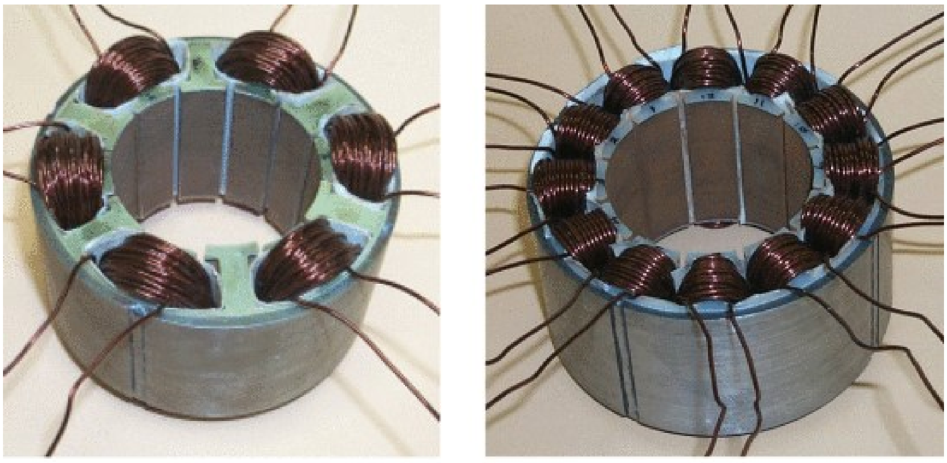
(a)
(b)

Figure 2.5: Fractional Slot Concentrated Winding Motors [11] **(a)** Single-layer **(b)** Double-Layer

In general, distributed overlapped windings produce both a sinusoidal magneto motive force (MMF) and an electro motive force (EMF) with a better harmonic content. This results in a smoother torque production.
FSCWs often produce a low k_w, but they offer great advantages as well. In addition, a double-layer FSCW helps in producing a better harmonic content and improve the winding factor k_w at the same time, as in [12].

Among the advantages using FSCW means that the teeth are wound one by one, with short end windings. Shortening the end windings means decreasing copper losses and this results in a more efficient machine. In addition, the axial length is reduced, so the machine is more compact. The concentrated winding manufacturing can be implemented through an industrial automation that can wrap each tooth consequently. In this way it is possible to obtain a more accurate work with a shorter process that results in a larger amount of motors produced with a lower manufacturing cost.

Using FSCW improves flux weakening capabilities of PM Motors that usually exhibit limited speed range in the torque-speed plane.

FSCW improves the fault-tolerance of the machine as well. In fact non-overlapped coils wound around a single tooth manage to reduce the contact among the phases and in particular the single layer winding minimize it. Moreover FSCWs have an higher leakage inductance and a low mutual inductance that limit short-circuit currents and improve fault-tolerance.

FSCW are usually used whenever a motor with high torque and low speed is to be designed.

2.1.6 Permanent Magnet Machine Model and Control

The model of a Permanent Magnet Motor can be obtained starting by the voltage equations on the three phases:

$$\begin{cases} u_a(t) = Ri_a(t) + \frac{d\lambda_a(t)}{dt} \\ u_b(t) = Ri_b(t) + \frac{d\lambda_b(t)}{dt} \\ u_c(t) = Ri_c(t) + \frac{d\lambda_c(t)}{dt} \end{cases} \tag{2.12}$$

where u is the total winding voltage, i is the winding current, R is the winding resistance and λ is the flux linkage.

These equations can be then expanded as in (2.13).

$$\begin{cases} u_a(t) = R_s i_a(t) + L_s \frac{di_a(t)}{dt} + e_a \\ u_b(t) = R_s i_b(t) + L_s \frac{di_b(t)}{dt} + e_b \\ u_c(t) = R_s i_c(t) + L_s \frac{di_c(t)}{dt} + e_c \end{cases} \tag{2.13}$$

where the flux linkage has been divided in two parts: the variations of the flux caused by the current and the *back electromotive force* (*bemf*) caused by the relative movement of the magnets with respect to the winding. In the equations R_s stands for synchronous resistance, L_s stands for synchronous inductance.

Through Park transformation it is possible to write the previous equations in the

dq reference system, where direct axis is aligned with the centre of the Permanent Magnet and the quadrature axis is aligned with rotor iron where there is no Permanent Magnet.
It is possible to write the equations (dropping time for a more straightforward comprension of the equations) as in (2.14).

$$\begin{cases} u_d = R_s i_d + L_s \frac{di_d}{dt} + e_d \\ u_q = R_s i_q + L_s \frac{di_q}{dt} + e_q \end{cases} \tag{2.14}$$

Then *bemf* can be rewritten as in (2.15).

$$\begin{cases} u_d = R_s i_d + L_s \frac{di_d}{dt} - \omega_{me} L_s i_q \\ u_q = R_s i_q + L_s \frac{di_q}{dt} + \omega_{me} L_s i_d + \omega_{me} \Lambda_{mg} \end{cases} \tag{2.15}$$

The equations shown in (2.15) are the ultimate model of a Permanent Magnet Synchronous Motor in the dq reference frame. The voltage on both axis is related to the resistance drop ($R_s i$), to the flux variations caused by the dynamics of the currents ($L_s \frac{di}{dt}$), to a term of cross-coupling ($\omega_{me} L_s i$) and to the flux on the Permanent Magnet present only on the q-axis ($\omega_{me} \Lambda_{mg}$).
Under the hypothesys of a conservative system it is possible to write an energy balance with the equations in the synchronous reference frame as in (2.16).

$$(u_d i_d + u_q i_q)dt = (R_s i_d^2 + R_s i_q^2)dt + L_s i_d di_d + L_s i_q di_q + \omega_{me} \Lambda_{mg} i_q dt \tag{2.16}$$

Recognizing in the energy balance the electric energy fed to the motor ($u\ i\ dt$), the joule losses ($R_s\ i^2\ dt$) and the magnetic energy stored in the system ($L_s\ i\ di$) what is left is the mechanical energy transferred to the load ($\omega_{me} \Lambda_{mg} i_q dt$).
From the mechanical energy trasferred to the system it is possible to obtain the mean torque equation that is represented as follows:

$$T_{dq} = \frac{3}{2} \cdot p \cdot \Lambda_{mg} \cdot i_q \tag{2.17}$$

where p stands for pole pairs and $\frac{3}{2}$ is a correction term added because of Park transformation. The torque, apart from motor parameters, depends on q-axis current. This is why the torque control of PM Motors is called Field Oriented Control (FOC): the generated current vector will be aligned with the q-axis and will be in this way ortogonal with the field of the magnet.

2.2 Permanent Magnet Machines with Magnetic Gearing Effect

Magnetic gears offer the same features as mechanical gears, reducing though the major drawbacks such as wear, overheat and need for periodic lubrication and maintenance.

Basically any form of mechanical gear can be reinvented using the magnetic gearing effect and building so a magnetic gear with the same use. Generally from an intuitive point a view magnetic gears are similar to mechanical gears with teeth replaced by magnets.

The general trend of publications and research is increasing focus on magnetic gears and it may make their commercial application closer and closer, as it is showed in [13]. This might be because of the high energy modern PM materials that also renewed interest in PM Synchronous Machines.

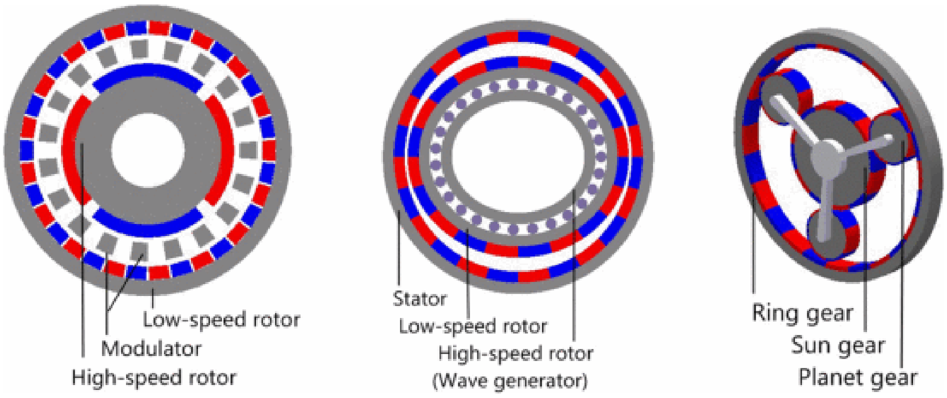

Figure 2.6: High torque dense magnetic gears [13] **(a)** Concentric **(b)** Harmonic **(c)** Planetary

In Figure 2.6 some popular torque dense magnetic gears are shown. In particular Figure 2.6(a) reminds of a classic gear wheel, Figure 2.6(b) shows an harmonic magnetic drive and Figure 2.6(c) shows an epicyclic magnetic gearbox.

The working principle of a concentric magnetic gear is that the central rotor (with low number of magnets) produces a rotating field that, also by the means of the flux modulating grill, has harmonics that synchronize with the field produced by the rotor (with high number of magnets). Thanks to this principle, the output shaft rotates at a lower speed but has a proportional increase in torque. A similar working principle is the basis of the other magnetic gears.

The concept of magnetic gears can also be applied directly to Rotary Machines. If the gearbox is magnetic, it may be possible to embed it in the Electric Motor rather than link it through a shaft. This helps making the total device more compact and perhaps even lighter.

2.2.1 Permanent Magnet Magnetically Geared Machines

The most easy way to implement Permanent Magnet Mechanically Geared Machines is by moving all the parts of the rotor and of the magnetic gear into a single volume: by this way a Magnetically Geared Machine is built. Main design features are the following:

- A stator which generates a rotating field with p_s pole pairs
- A rotor of with the same number of poles p_s of the field (reminds of a mechanical sun gear) produced by the stator that will move with a synchronous speed
- A flux modulating grill that will implement the magnetic gear effect, composed of z_g elements (what is called modulator)
- A rotor with p_r pole pairs (reminds of a mechanical ring gear)

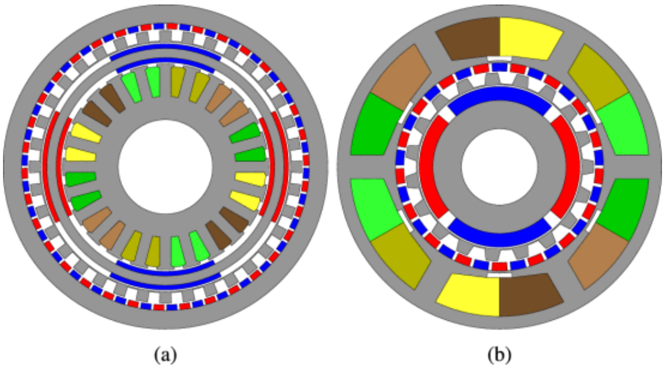

Figure 2.7: Magnetically Geared Machines [14] **(a)** Outer Rotor **(b)** Inner Rotor

The working principle is that the stator produces a magnetic field that drags a classic Superficial Permanent Magnet high speed rotor, which has Permanent Magnets both on the inside and outside sides. Exploiting rotation produced by the motor, the high speed rotor generates a magnetic gearing effect interacting with the grill modulator and the low speed rotor. Basically, the induction that is generated by the high speed rotor is modulated and produces a higher poles induction that drags the low speed rotor. A Magnetically Geared Machine is a sum of a classic motor and a magnetic gear that are embedded together. The number of modulator segments must be computed as:

$$z_g = p_s + p_r \tag{2.18}$$

MGMs can be classified as coupled or decoupled. The difference between them is on the fact that the Eletric Machine and the gear share or less the same flux paths.

Like in planetary gears MGMs can work in different ways depending on the part of the machine's movement is kept still. The most common functioning is when the ring gear is kept constrained, instead the sun gear and the modulator are free to move, as in [14].

Magnetically Geared Machines can be built with an inner or outer stator as it is shown in Figure 2.7.

2.2.2 Permanent Magnet Vernier Machines

Researchers have proposed topologies that do not implement a full magnetic gear as well. This is the case of Vernier type machines. Vernier Machines are MGMs where the high speed inner rotor is omitted.

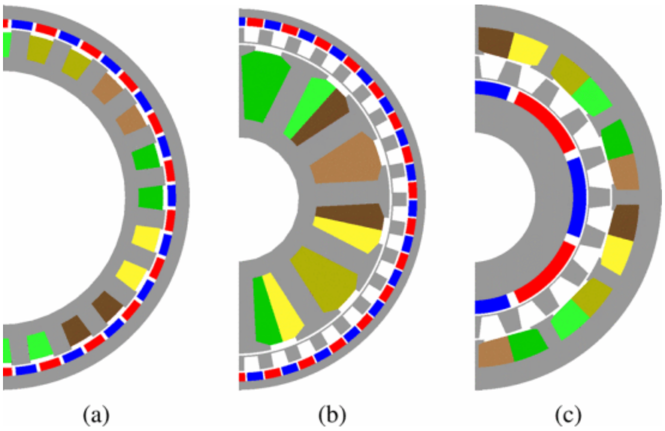

Figure 2.8: Vernier Machines [13] **(a)** Outer Rotor PM Vernier Machine **(b)** Outer Rotor PM Vernier Machine with modulator **(c)** Inner Rotor PM Vernier Machine with modulator

In general they can be described as motors with:

- A stator which generates a rotating field with p_s pole pairs
- A rotor with p_r pole pairs
- Sometimes a flux modulating grill that will implement the magnetic gearing effect, composed of z_g elements

So most common Vernier Machines are similar to PM Machines where the number of rotor poles is different from the stator poles. They can be built with an inner or outer stator, also it can be present a flux modulator or not.

Vernier Machines attract much attention because of their simple structure that allows a lower cost and a way larger freedom in terms of design.

If the machine is built with no flux modulator the flux modulating effect that generates the magnetic gearing effect is carried out by the stator teeth. Thus, teeth replace the modulator elements, as it is explained in [15], and so the number of teeth must check:

$$p_r = Q_s \pm p_s \tag{2.19}$$

Otherwise if the modulator is present, the number of stator slots is free and the modulator segments are chosen as described in the previous Section.
The working principle, explained in [16], is based on the fact that the stator produces p_s and multiple harmonics, but if p_r is chosen properly, the stator produces a harmonic with p_r pole pairs that produces torque. The rotor synchronizes on the correct harmonic.
To have a proper increase of torque the pole ratio (ratio between p_r and p_s) must be higher than 3 or 4, as reported in [17]. The equation of the average torque for Vernier Machine is the same of the PM Machine:

$$T_{dq} = \frac{3}{2} \cdot p_r \cdot \Lambda_{mg} \cdot i_q \tag{2.20}$$

where the pole pairs used are the rotor ones.

Chapter 3

Analysis and Design of Outer Rotor SPM Motors

The design of an improved motor for the Exoskeleton application began trying to investigate characteristics and performance of the motor which was chosen by the Exoskeleton design research group and in particular in [8].

3.1 Flipsky 6354 Analysis

The chosen candidate was Flipsky 6354, which is an Outer Rotor Superficial Permanent Magnet Motor with the following size characteristics:

D_e	L_{stk}	G_{tot}
63 mm	54 mm	640 g

Table 3.1: Size of Flipsky 6354

Configuration	Q_s	12
	2p	14
	G_{tot}	640 g
Nominal conditions	n	3620 rpm
	T_n	2 Nm
	P_n	850 W
	V_n	24/48 V
OL conditions	T_{max}	7 Nm
	P_{max}	2450 W
	I_{max}	65 A

Table 3.2: Flipsky 6354 datasheet features

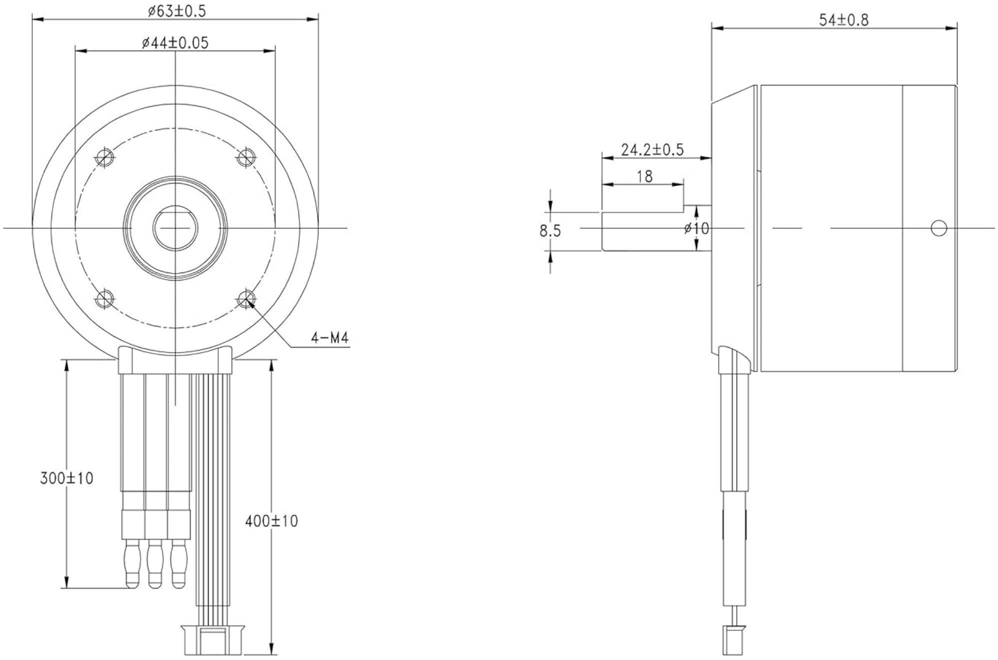
ø63±0.5
ø44±0.05
4-M4
300±10
400±10
54±0.8
24.2±0.5
18
8.5
ø10

Figure 3.1: Flipsky 6354 catalog drawing

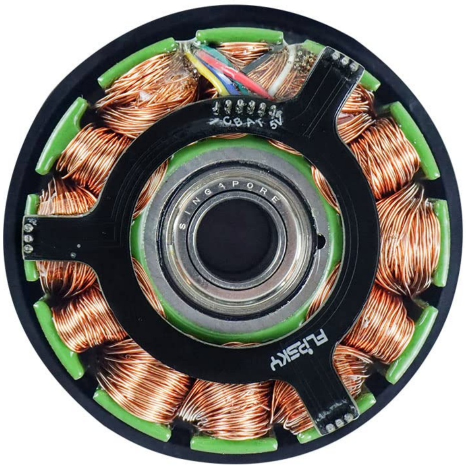
SINGAPORE
FLIPSKY

Figure 3.2: Flipsky 6354 details

As it is shown in Table 3.1, the motor has a pretty small size and is really light, usually it is employed in electric skateboards applications.
Flipsky provides some useful pictures of the inside part of the machine. From this pictures it can be seen that this is an SPM (Superficial Permanent Magnet) Motor.

The chosen configuration is 12 slots and 14 poles which, as highlighted in [18] [19], is very good in terms of output torque and torque ripple.
Having 12 slots and 14 poles the motor has a fractional slot winding allowing high efficiency and small axial size. This is due to the short end winding that minimizes copper. Unfortunately this winding also leads to an increase in magneto motive force harmonics and air gap flux sub harmonics.
Moreover, being this an External Rotor Motor, it has a higher air-gap diameter that provides higher output torque, so power and torque density can be increased. This is one of the best solutions for the design of motors with light weight requirements and the performance results is remarkable.
From data sheet, shown in Table 3.2, it can be understood this is almost a torque motor. The electric power absorbed is converted in mechanical power with low speed and high torque. In particular, this is a very slow motor for its size but it can provide quite an high torque, especially in overload functioning. Comparing nominal and overload working points it is computed an overload coefficient of $k_{OL} = 3.5$. The overload coefficient is pretty high but this is not an issue if the overload current flows for a short time, as it is well described in [20]. This is the factor that with the nominal current computes the overload working point that in the perspective of this work is perhaps the most important feature.
Being Flipsky 6354 a commercial motor many of the geometrical features are unknown. Some hypothesis are made and an analytical approximated design is carried out to try and understand which is the current density used and what is the preferred working point. This may help upgrade or change the features of the motor shifting them to what is more suitable for this application.

3.1.1 Flipsky 6354 Drawing

A total design of Flipsky 6354 can be carried out from the few known geometrical details. The aim is reaching a good approximated drawing of the real motor so it is possible to analyze it. First of all a sensible air-gap g is chosen:

$$g = 0.5 \text{ mm}$$

The magnet thickness t_m is chosen as a multiple of this dimension to ensure a high air-gap magnetization but avoiding magnet demagnetization, giving so:

$$t_m = 4 \cdot g = 2 \text{ mm}$$

From this point, knowing external motor diameter D_e and supposing an external back iron thickness h_e, a first approximation of air-gap diameter D can be computed:

$$D = D_e - 2(h_e + g + t_m) = 64 - 2(3 + 0.5 + 2) = 52 \text{ mm}$$

The computed dimensions allow a first drawing that is carried out and iteratively upgraded until the result in Table 3.3 is reached.
The drawing, which can be seen in Figure 3.3, is then analyzed to see if the performance requirements are reached.

D_e	D	w_t	h_s	h_{wed}	h_{so}	w_{so}	S_{slot}	L_{stk}
63 mm	52 mm	4.3 mm	13 mm	1.5 mm	0.4 mm	2 mm	65.17 mm^2	54 mm

Table 3.3: Stator dimentions of Flipsky 6354

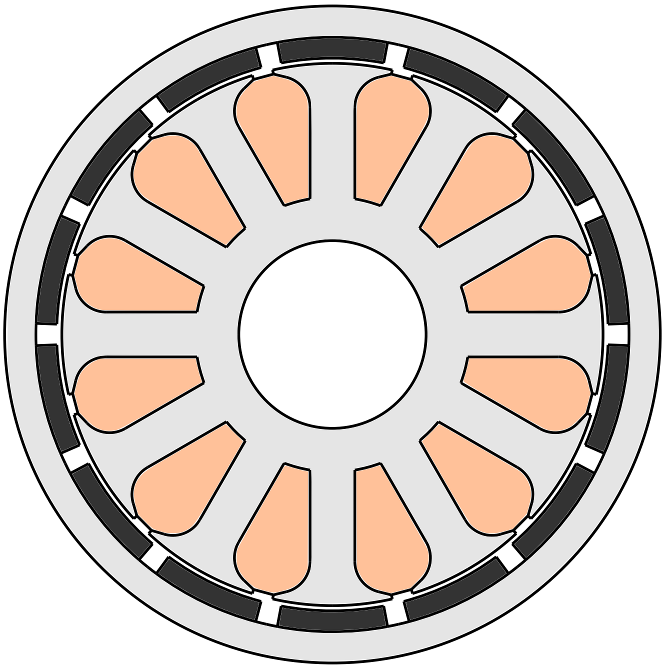

Figure 3.3: Flipsky 6354 drawing

3.1.2 Flipsky 6354 FEA

The resulting motor is analyzed via FEA with FEMM program and the magnetization of the machine in different operating conditions is displayed in Figure 3.4. The result of the analysis confirms the good approximation of the design. It can be seen that torque performance is as good as expected with low error and the max torque is at the current vector degree that was expected, without any saturation.

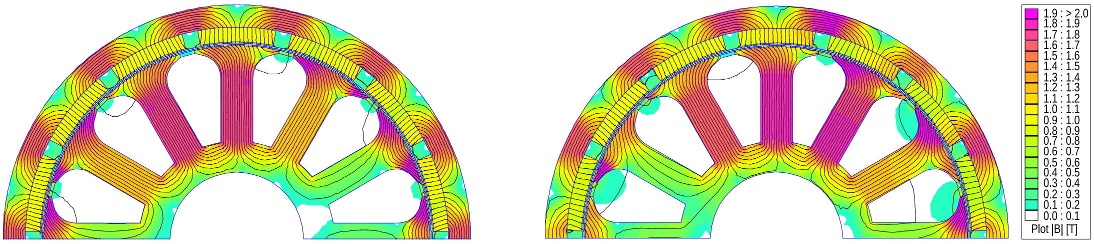

(a) (b)

Figure 3.4: FEA analysis **(a)** No load conditions **(b)** FOC Overload conditions

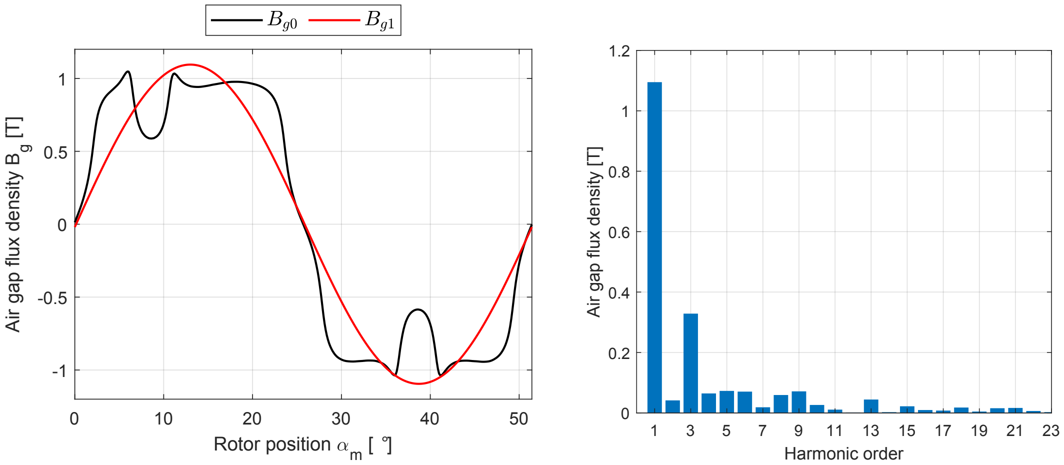

(a) (b)

Figure 3.5: No load induction **(a)** Zero and First order harmonics comparison **(b)** Harmonic spectrum

As it can be observed in Figure 3.4 both in no load and in overload conditions the machine is near saturation without any excessive flux leakages. The result is a good exploitation of the motor without loss of performance. In Figure 3.5 the flux density can be observed. There is low harmonics presence, which translates in pretty clean flux linkages, as can be seen in Figure 3.6. Furthermore it can be highlighted that the third harmonic present in Figure 3.5(b) is not related to the presence of the stator teeth.

Peak value of the first harmonic of the no load air-gap flux density is:

$$\hat{B}_{g1} = 1.113 \text{ T}$$

In Figure 3.7 the torque performance is shown in detail, highlighting a motor that with $J_N = 7 \ \frac{\text{A}}{\text{mm}^2}$ can produce the nominal torque of 2 Nm with very low ripple. What is very interesting though is the peak torque in overload conditions, which is huge for the size of the motor. Altogether with the reduction provided by the Harmonic Drive chosen in [8], the motor could provide, working in nominal conditions,

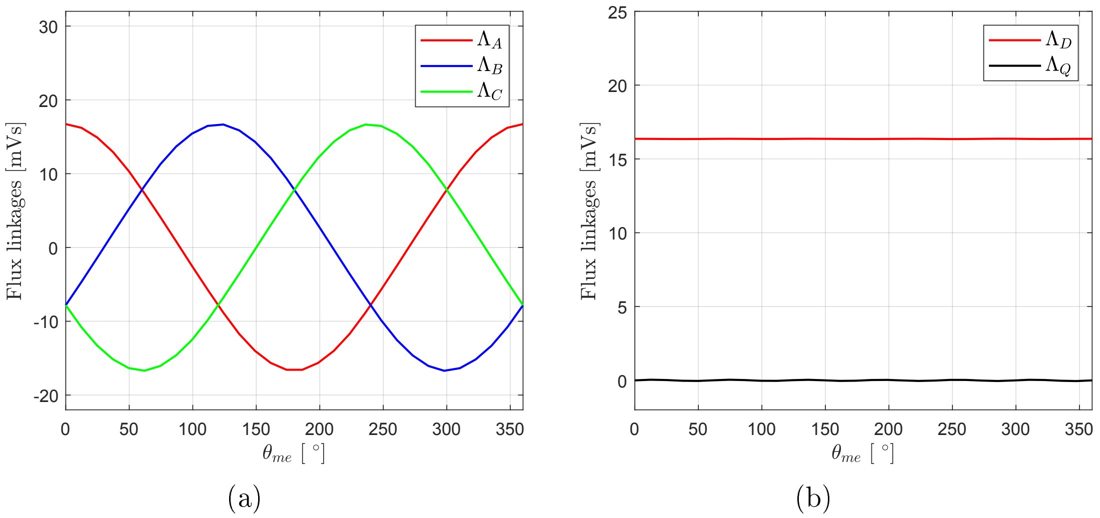

Figure 3.6: No load fluxes **(a)** In abc reference frame **(b)** In dq reference frame

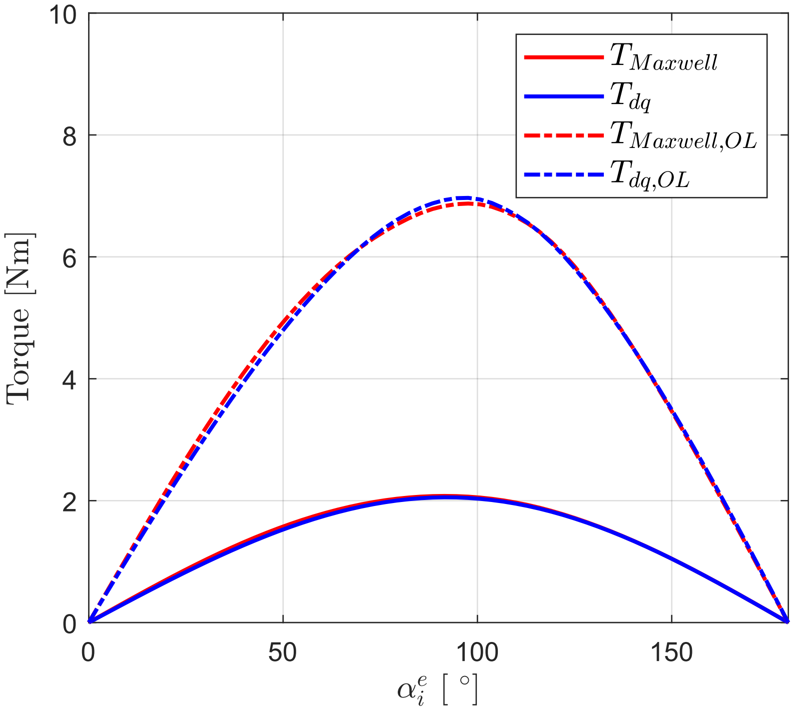

Figure 3.7: MTPA in nominal and overload conditions

a total output torque of 200 Nm, that would already be more than the maximum output torque of the reducer. Nominal and overload torque are again in range with what was expected. Going more into detail the mean torque results:

$$\overline{T}_{Maxwell} = 2.051 \text{ Nm}$$

$$\overline{T}_{dq} = 2.050 \text{ Nm}$$

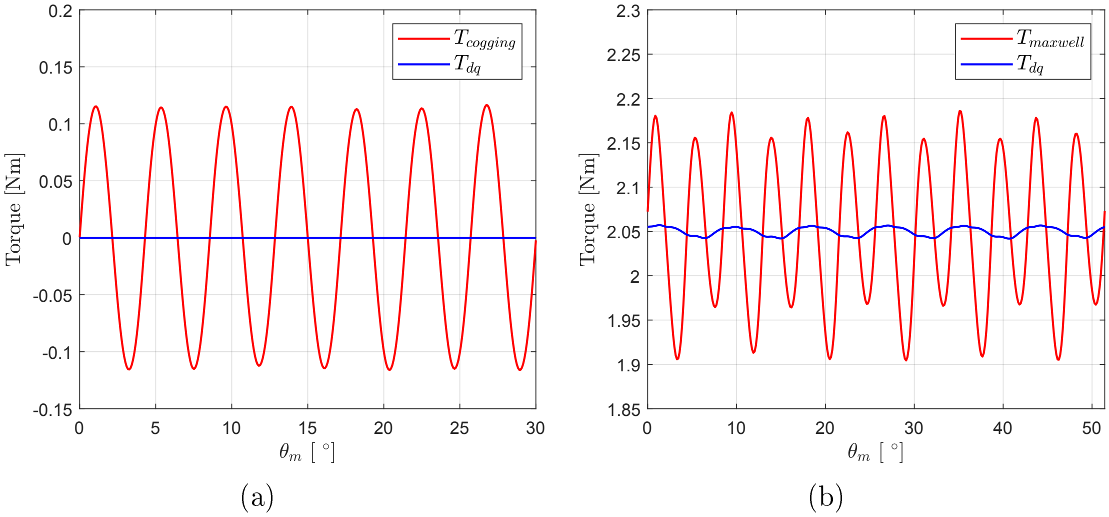

(a) (b)

Figure 3.8: **(a)** Cogging torque **(b)** Torque ripple in nominal conditions

They are both the torque computed using Maxwell stress tensor and the torque computed with the classic dq method using power balance equations.

It is now possible to focus on the cogging torque, reported in Figure 3.8(a), estimated as:

$$\Delta T_{Maxwell} = 0.2325 \text{ Nm}$$

Percentage wise the cogging torque is:

$$\frac{\Delta T_{Maxwell}}{\overline{T}} = 11.3\%$$

Regarding torque ripple, reported in Figure 3.8(b), the maximum oscillations are estimated as:

$$\Delta T_{Maxwell} = 0.2814 \text{ Nm}$$

Which in other words is:

$$\frac{\Delta T_{Maxwell}}{\overline{T}} = 13.7\%$$

This is not a very low torque ripple considering the 12 slots 14 poles configuration chosen, but it is in range with a generic motor torque ripple. To reduce it some design details could be modified.

Focusing on torque control the machines confirms as expected a Maximum Torque Per Ampere point at around 90°, highlighted in Figure 3.7 in both nominal and overload conditions.

In the end as it is shown in Figure 3.9 the motor is pretty far from saturation (even though a bit of saturation can be appreciated on d axis), with an almost linear behavior also in overload conditions. This means that the machine could be saturated even more and so the teeth and both the stator and the rotor back iron could be tightened.

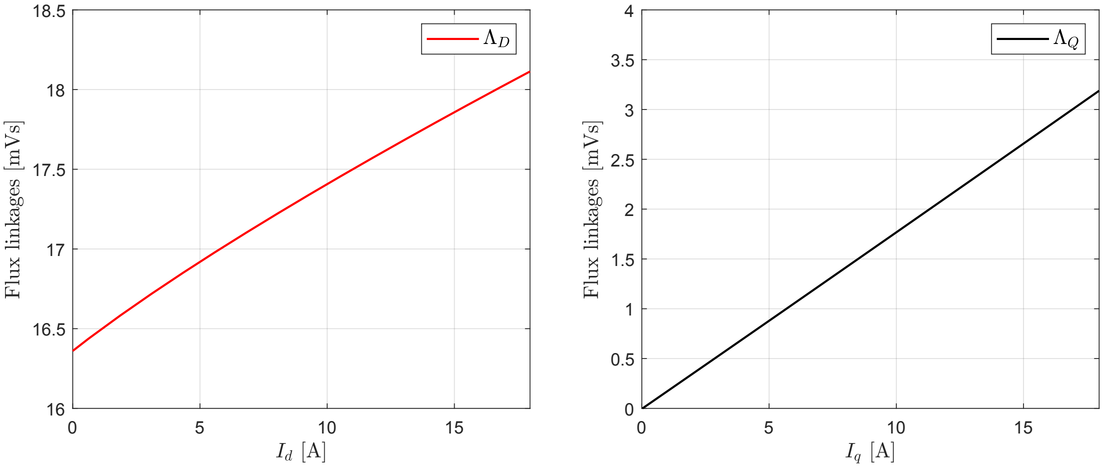

(a) (b)

Figure 3.9: Current range up to $1.5 \cdot I_n$ **(a)** Flux linkage with current vector on d-axis **(b)** Flux linkage with current vector on q-axis

3.2 Outer Rotor SPM Motor Prototypes

Since the size of the joint is the main focus, an upgrade in the design should reduce the total weight. In the joint the most heavy part is the Harmonic Drive which provides a reduction ratio of 100. From the point of view of the actuator an interesting aspect may be to try and design a motor that can provide enough torque to allow a switch from the Harmonic Drive to an epicyclic gearbox or a cycloidal drive with a lower reduction ratio. This may perhaps result in a higher motor weight but in a lower total weight of the joint. The reduction of the axial size is an another desired feature.

Then the idea is to shorten the stack size, increasing the total diameter and the weight in order to have a higher output torque. As already explained in Chapter 2 the motor torque depends on the stack size length and on the square of the diameter. Increasing the diameter should produce an increase in torque that allows to decrease massively the stack size.

3.2.1 1214 MkI: 12 slots 14 poles with stack length reduction

Keeping the same current density of the Flipsky 6354 and his overload working point as well, a variation in the dimensions is carried out. An improvement in the properties of interest such as nominal and max torque is looked into.

The first option is to cut the stack length to half and to increase the external diameter to 100 mm to have an higher air-gap diameter which results in a higher output torque.

D_e	D	w_t	h_s	h_{wed}	h_{so}	w_{so}	S_{slot}	L_{stk}
100 mm	83 mm	7 mm	24 mm	4.5 mm	1.25 mm	1.5 mm	155.8 mm^2	27 mm

Table 3.4: Stator dimensions of 1214 MkI

D_e	L_{stk}	G_{tot}
100 mm	27 mm	1265 g

Table 3.5: Size of 1214 MkI

As it is shown in Table 3.4, the external diameter is increased, the stack length is half in respect with Flipsky 6354 and so all the dimensions are remodulated. The designed motor is shown in Figure 3.10. Size wise the weight is doubled and so a considerable increase in torque should be found. Details on the size of the motor are displayed in Table 3.5.

A FEA of the designed motor is carried out and the magnetization of the machine

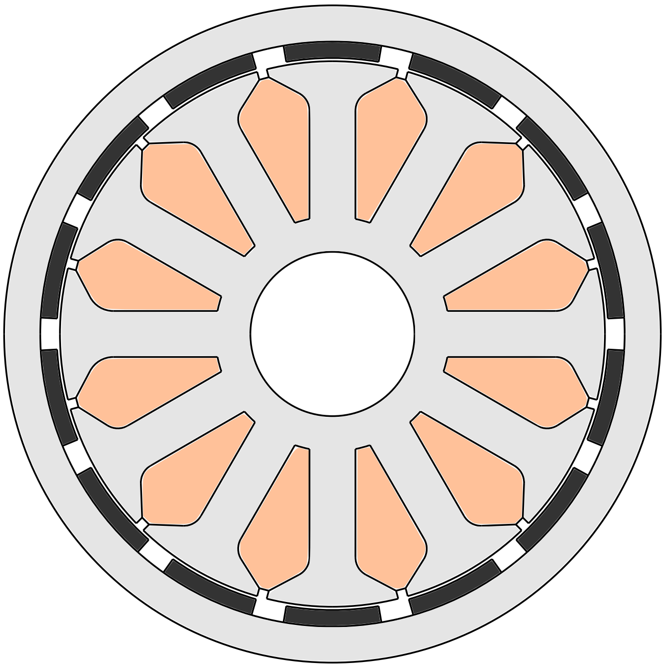

Figure 3.10: 1214 MkI drawing

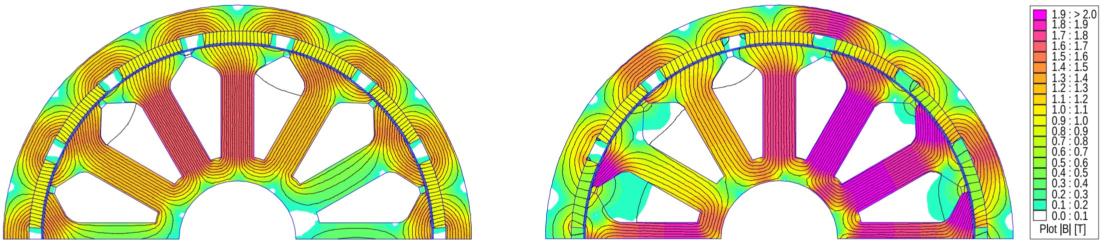

(a) (b)

Figure 3.11: FEA analysis **(a)** No load conditions **(b)** FOC Overload conditions

in both no load and overload conditions can be seen in Figure 3.11. There is an increase in the saturation of the motor, in particular in the teeth as well as in some parts of the back iron.

It is important to stress that, even though a relevant saturation is reached, this happens in an extreme overload condition that is kept for a very short amount of time and so there are not any functioning issues.

A no load flux density analysis is carried out and the results are available in Figure 3.12. Such do not differ much from what was expected, with only a slight loss in peak value of the first harmonic compared to the original motor. It is estimated:

$$\hat{B_{g1}} = 1.099 \text{ T}$$

A slight increase in harmonics, that can be seen in Figure 3.12(b), is also proven looking at no load fluxes induced in the winding both in abc and dq reference frame,

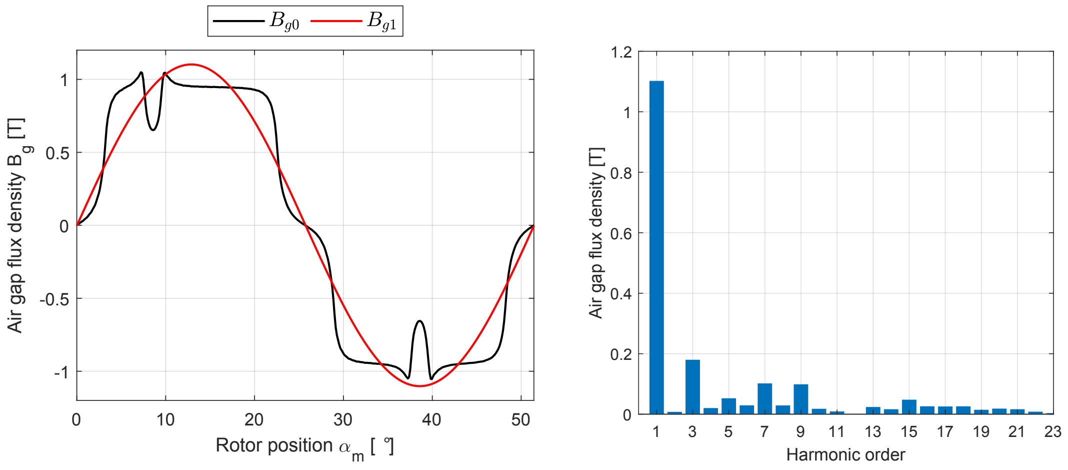

(a) (b)

Figure 3.12: No load induction **(a)** Zero and First order harmonics comparison **(b)** Harmonic spectrum

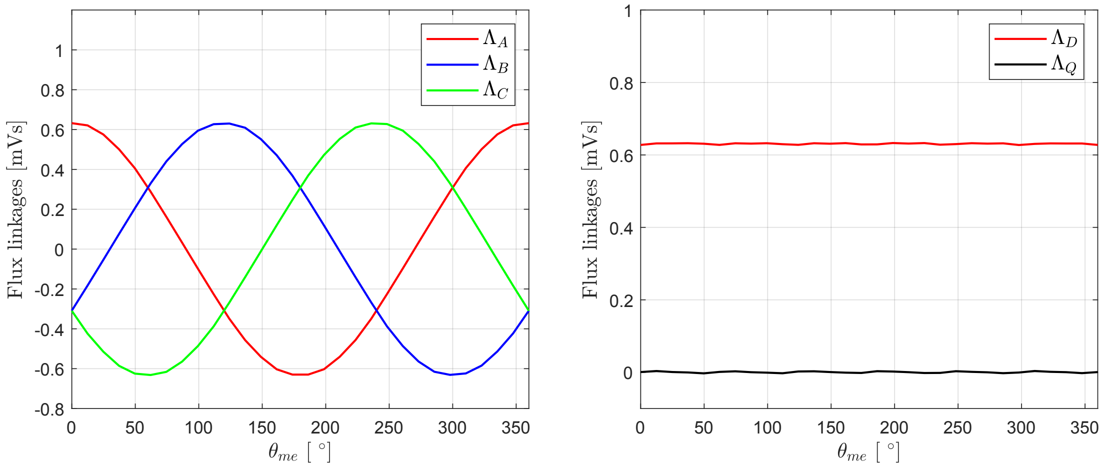

(a) (b)

Figure 3.13: No load fluxes **(a)** In abc reference frame **(b)** In dq reference frame

as it is shown in Figure 3.13.

At this point to understand if the motor reaches the right amount of nominal and max torque it is possible to look at Figure 3.14, where torque performance is investigated.

What it is shown in Figure 3.14 is a situation where there is some saturation in the MTPA curve of the overload functioning. This happens as the current in overload functioning is quite high and so is the magnetomotive force.

That is not a great problem as the motor is usually used in FOC conditions and what happens is just a slight loss compared to maximum torque that can be produced. If this motor was to be prototyped a test to spot the perfect MTPA point in overload

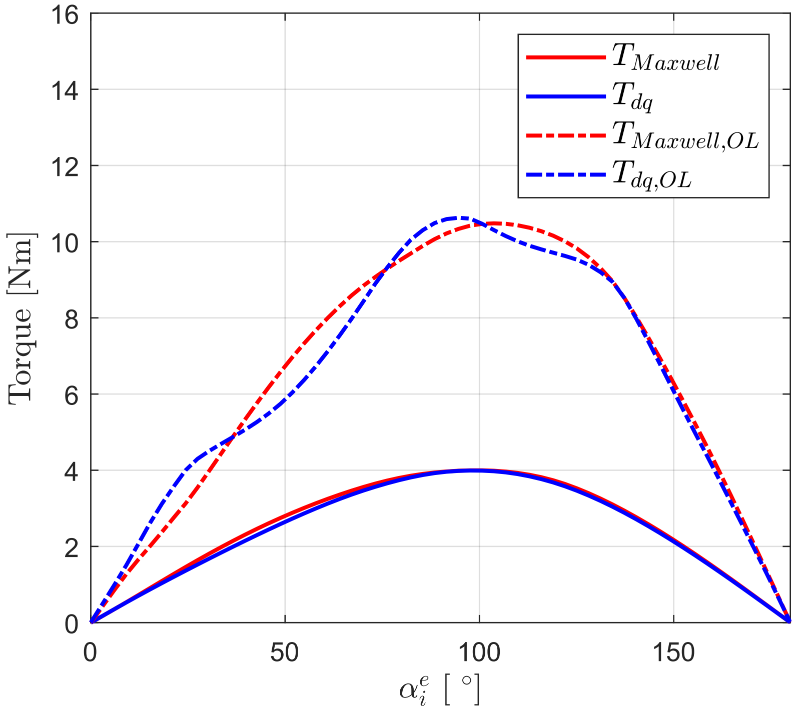

Figure 3.14: MTPA in nominal and overload conditions

conditions should be carried out.
The motor nominal mean torque appears to be:

$$\overline{T}_{Maxwell} = 3.971 \text{ Nm}$$
$$\overline{T}_{dq} = 3.973 \text{ Nm}$$

While the cogging torque amplitude, as it is shown in Figure 3.15, appears to be:

$$\Delta T_{Maxwell} = 0.2843 \text{ Nm}$$

Which means that in terms of percentage the cogging torque is not pretty different from the original motor situation, as it follows:

$$\frac{\Delta T_{Maxwell}}{\overline{T}} = 7.2\%$$

If a rotor rotation is done while the MTPA current angle is kept, it is computed via FEA the torque ripple of 1214 MkI that has a maximum amplitude of:

$$\Delta T_{Maxwell} = 0.3745 \text{ Nm}$$

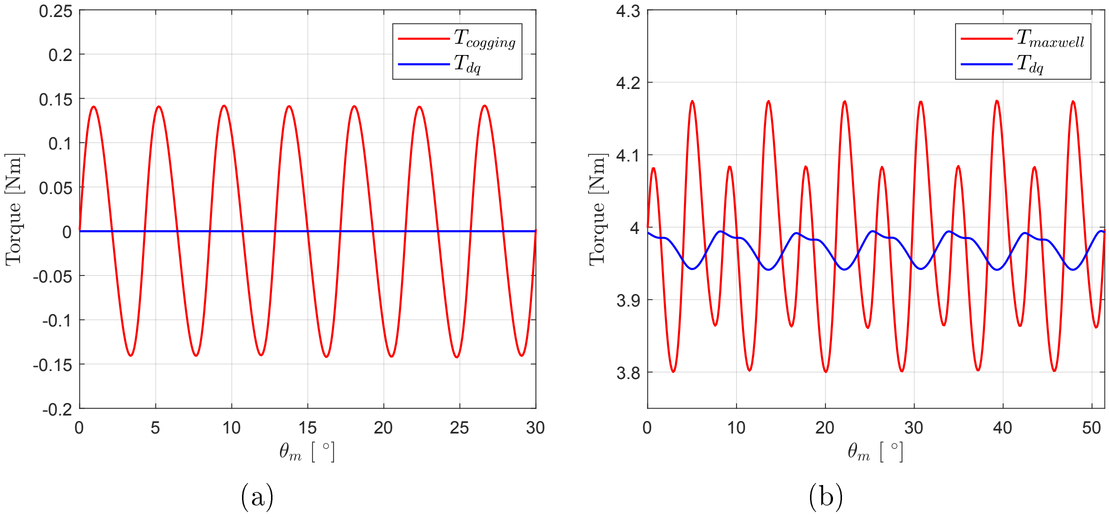

(a) (b)

Figure 3.15: **(a)** Cogging torque **(b)** Torque ripple in nominal conditions

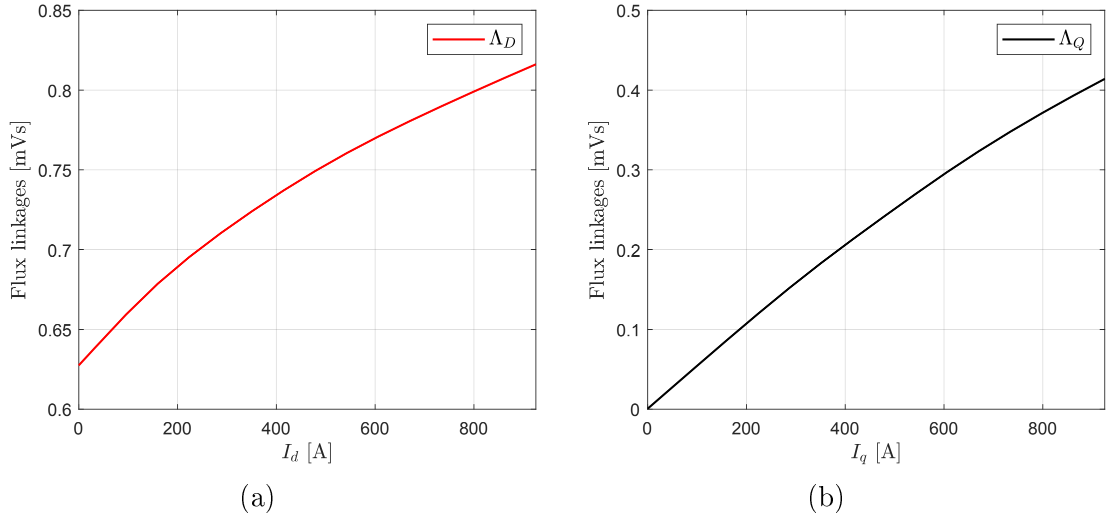

(a) (b)

Figure 3.16: Current range up to $1.5 \cdot I_n$ **(a)** Flux linkage with current vector on d-axis **(b)** Flux linkage with current vector on q-axis

Which percentage wise gives:

$$\frac{\Delta T_{Maxwell}}{\overline{T}} = 9.4\%$$

In conclusion with the designed motor it is possible to reach a maximum torque in overload operations equal to:

$$T_{max,OL} = 10.63 \text{ Nm}$$

From the collected data it can be observed a slight increase of air-gap flux density, flux linkage harmonics, saturation and torque ripple in respect with Flipsky 6354. In addition, nominal torque is increased of 94%, whereas max torque is 52% higher. Resizing the motor could result in an increase in output torque that could lead towards an integration with an epyciclic gearbox or a cycloidal drive with a lower reduction ratio which could perhaps offer 80 or 100 Nm of total joint torque. If the transmission is rigid enough, the actuator performance would be sufficient to implement gait without the need of a heavy Harmonic Drive.

An another kind of direction could be to shorten even further the stack length. This would result in a reduction of the performance, that could be limited to what was guaranteed by Flipsky 6354, obtaining in this way a motor that is not better performance wise but is for sure a better fit in terms of joint size. With a stack length $L_{stk} = 13.5$ mm it could be possible to achieve 2 Nm of nominal torque, which is what Flipsky 6354 produces.

3.2.2 3624 MkI: 3/2 configuration

A configuration with three stator slots for every couple of rotor poles may be suitable for the motor. Such a design allows a simple and quick FEA analysis. Moreover, an high number of parallel paths may be used, helping to lower the current that flows in each coil and thus lowering the inverter current output. Unfortunately, these motors are highly periodic, and the high periodicity produces much repetition of equal positions between rotor poles and teeth during a rotor rotation. The result is an high torque ripple, as it is highlighted in [18] [19].
Choosing a number of slots $Q_s = 36$, it is computed a number of poles $2p = 24$. The high number of slots and accordingly of poles allows to reduce the flux per pole, and so to tighten the rotor and the back-iron. A design of this motor is carried out with the same size constraints of 1214 MkI, keeping D_e at 100 mm and L_{stk} at 27 mm.
An approximated design is done through a first analytical computation. Beginning from the choice of an air-gap:

$$g = 0.5 \text{ mm}$$

To start a really thick magnet is chosen, such as:

$$t_m = 5 \text{ mm}$$

This is probably to be reduced later because the magnet versus air-gap thickness ratio is quite high. Then, the approximated air-gap flux density B_{g0} is computed as:

$$B_{g0} = \frac{B_{rem}}{1 + \frac{\mu_r \cdot g}{t_m}} = \frac{1.2}{1 + \frac{1.05 \cdot 0.5}{5}} = 1.08 \text{ T}$$

Afterwards, the air-gap stator radius r_g is obtained:

$$r_g = r_e - h_e - g - t_m - h_{so} = 50 - 2 - 0.5 - 5 - 0.5 = 42 \text{ mm}$$

Which checks with a diameter $D = 84$ mm. The slot pitch is simply computed with the equation:

$$p_s = \frac{2 \cdot \pi \cdot r_g}{Q_s} = \frac{2 \cdot \pi \cdot 42}{36} = 7.33 \text{ mm}$$

Making an hypothesis of half of the slot pitch filled by the slot and half filled by the tooth, it can be computed a tooth width of:

$$w_t = 0.5 \cdot p_s = 0.5 \cdot 7.33 = 3.7 \text{ mm}$$

With an estimated slot height of $h_s = 17$ mm, approximated slot and copper sections can be computed considering a slot fill factor $k_{fill} = 0.4$.

$$S_{slot} = 37 \text{ mm}^2$$
$$S_{cu} = k_{fill} \cdot S_{slot} = 0.4 \cdot 37 = 15 \text{ mm}^2$$

Always considering a nominal current density $J_N = 7 \ \frac{\text{A}}{\text{mm}^2}$, an approximated valutation of the torque can be computed as it follows:

$$\hat{K}_s = \frac{\sqrt{2} \cdot I_{slot}}{p_s} = \frac{\sqrt{2} \cdot J_N \cdot S_{cu}}{p_s} = \frac{\sqrt{2} \cdot 7 \cdot 15}{7.33} = 20258 \ \frac{\text{A}}{\text{m}}$$
$$T_{em} = \hat{K}_s \cdot \hat{B} \cdot \frac{\pi}{4} \cdot D^2 \cdot L_{stk} = \hat{k}_s \cdot 1.08 \cdot \frac{\pi}{4} \cdot 0.084^2 \cdot 0.027 = 3.27 \text{ Nm}$$

Finally a FEMM drawing is carried out and critic points where saturation arises are reshaped until a final design is reached.

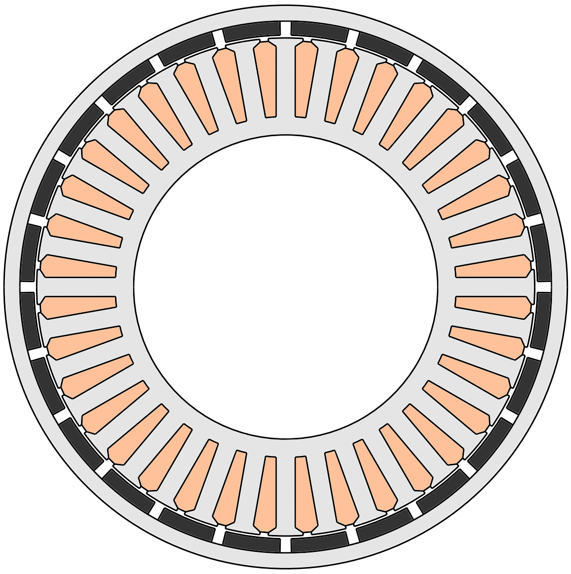

Figure 3.17: 3624 MkI drawing

D_e	D	w_t	h_s	h_{wed}	h_{so}	w_{so}	S_{slot}	L_{stk}
100 mm	88.4 mm	3.4 mm	14 mm	1 mm	0.5 mm	1.5 mm	39.75 mm^2	27 mm

Table 3.6: Stator dimensions of 3624 MkI

D_e	L_{stk}	G_{tot}
100 mm	27 mm	943 g

Table 3.7: Size of 3624 MkI

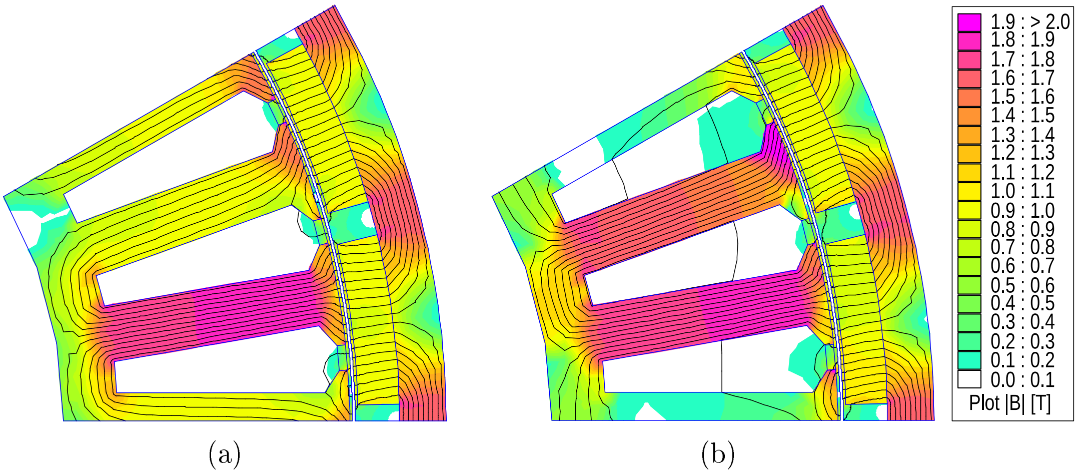
1.9 : > 2.0
1.8 : 1.9
1.7 : 1.8
1.6 : 1.7
1.5 : 1.6
1.4 : 1.5
1.3 : 1.4
1.2 : 1.3
1.1 : 1.2
1.0 : 1.1
0.9 : 1.0
0.8 : 0.9
0.7 : 0.8
0.6 : 0.7
0.5 : 0.6
0.4 : 0.5
0.3 : 0.4
0.2 : 0.3
0.1 : 0.2
0.0 : 0.1
Plot |B| [T]

(a) (b)

Figure 3.18: FEA analysis **(a)** No load conditions **(b)** FOC Overload conditions

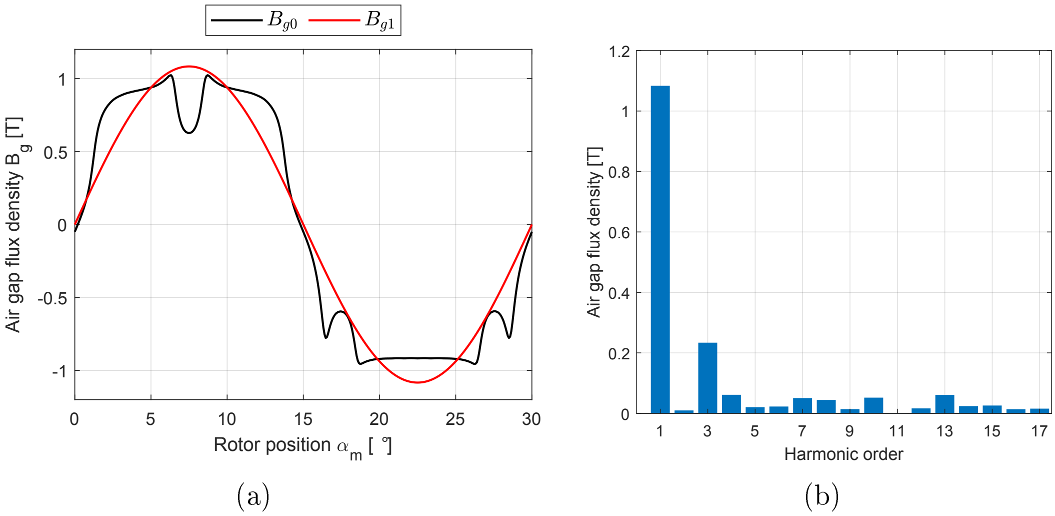

(a) (b)

Figure 3.19: No load induction **(a)** Zero and First order harmonics comparison **(b)** Harmonic spectrum

The drawing of the designed motor is displayed in Figure 3.17 and the main dimensions are presented in Table 3.6. It can be appreciated looking at Table 3.7 a lower motor weight in comparison with 1214 MkI. It is probably linked to the higher number of poles in respect with 1214 configuration.

A FEA analysis that shows magnetization of 3624 MkI is shown in Figure 3.18 in both no load and overload conditions.

An air-gap flux density analysis is shown in Figure 3.19. A slightly more relevant amount of harmonics can be seen as it is shown in Figure 3.19(b) and in Figure 3.20, comparing this motor to the previous ones.

First harmonic peak value appears to be equal to:

$$\hat{B}_{g1} = 1.083 \text{ T}$$

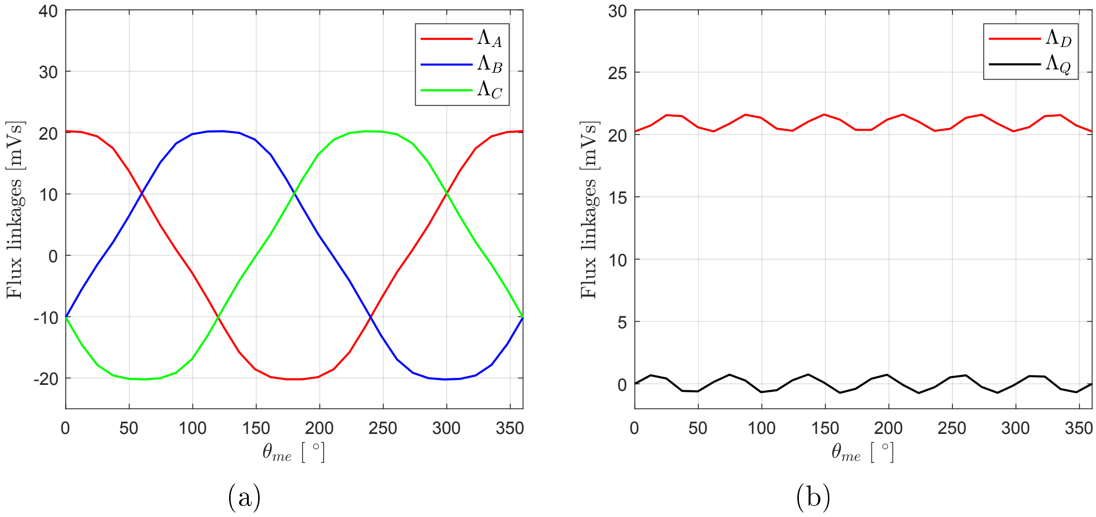

Figure 3.20: No load fluxes **(a)** In abc reference **(b)** In dq reference

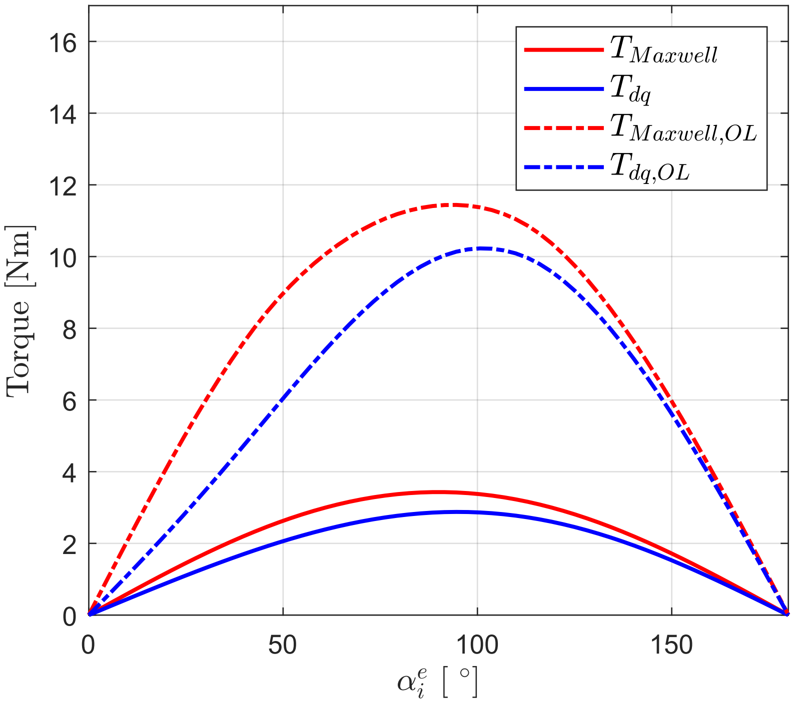

Figure 3.21: MTPA in nominal and overload conditions

With the usual current density of $J_N = 7 \, \frac{\mathrm{A}}{\mathrm{mm}^2}$ it is possible to reach, rotating the current vector, a max nominal torque of 2.877 Nm which is not as much as expected. This could be explained probably by the variation of design dimensions in comparison with the quick and simple analytical computation.

The motor shows a maximum torque in overload conditions similar to 1214 MkI, which is then a good result in the case of an integration with an epicyclic gearbox

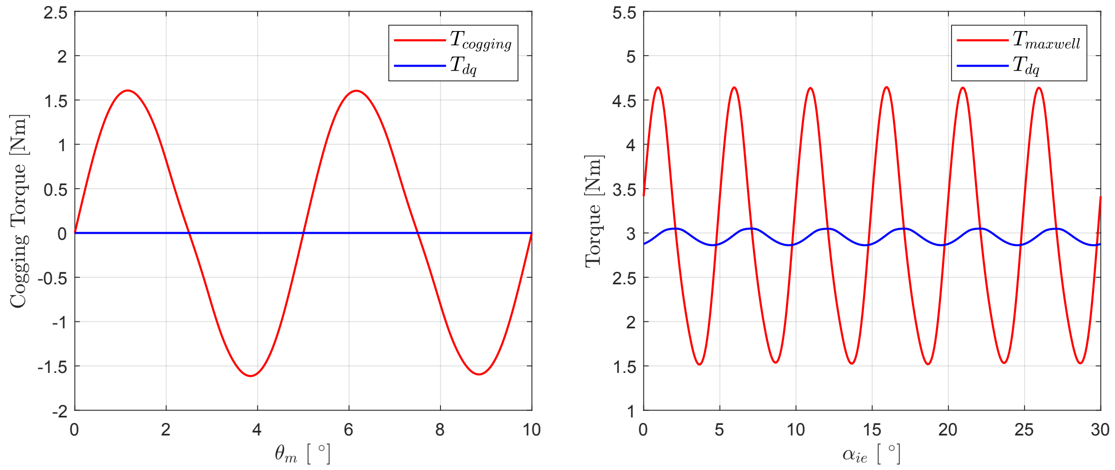

(a) (b)

Figure 3.22: **(a)** Cogging torque **(b)** Torque ripple in nominal conditions

or a cycloidal drive.

From Figure 3.21 it can be appreciated a slight deviation of MTPA point towards 100° probably because of saturation and flux leakages. It must be remembered that this happens with an overload coefficient of $k_{OL} = 3.5$, which means that the motor is absorbing three and a half times the nominal current. This together with the narrow dimensions of the motor explains the phenomenon.

Focusing on torque the mean values obtained are:

$$\overline{T}_{Maxwell} = 2.963 \text{ Nm}$$
$$\overline{T}_{dq} = 2.954 \text{ Nm}$$

Instead cogging torque results:

$$\Delta T_{Maxwell} = 3.221 \text{ Nm}$$

It is important to notice that it is quite an high cogging torque, and as expected the motor shows an high torque ripple. Cogging torque computed in terms of percentage checks:

$$\frac{\Delta T_{Maxwell}}{\overline{T}} = 108.8\%$$

In the end torque ripple computed in both dq and Maxwell stress tensor fashion is:

$$\Delta T_{Maxwell} = 3.13 \text{ Nm}$$

Which matches with an higher torque ripple compared to 12 slots 14 poles motor previously analyzed:

$$\frac{\Delta T_{Maxwell}}{\overline{T}} = 105.7\%$$

In overload conditions the maximum torque estimated is:

$$T_{max,OL} = 10.23 \text{ Nm}$$

In conclusion, comparing 3624 MkI with 1214 MkI, the 3/2 configuration motor has definitely a lower weight, even though the maximum torque in both nominal and overload conditions doesn't match with what is achieved by 1214 MkI. This is the reason why torque density obtained is lower. Moreover, there is also a problem related to torque ripple as it is estimated to be many times higher than it is in 1214 MkI.

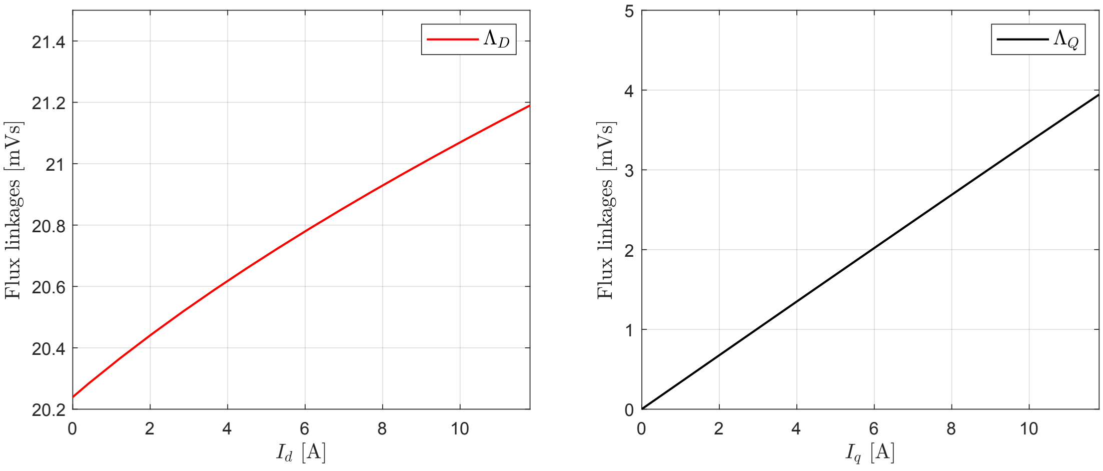

(a) (b)

Figure 3.23: Current range up to $1.5 \cdot I_n$ **(a)** Flux linkage with current vector on d-axis **(b)** Flux linkage with current vector on q-axis

3.2.3 1214 MkII: 12 slots 14 poles with halbach configuration

An another improvement can be achieved by adding to good configurations an halbach array Permanent Magnet disposition. As in [21], [22] and [23] this configuration consists of an array of Permanent Magnets not only put on the rotor in a NS disposition, but adding magnets, which are called *halbach magnets*, with a tangential polarization side by side with them.

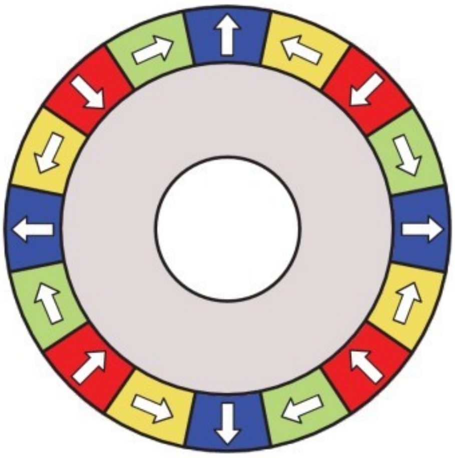

Figure 3.24: Halbach magnets disposition

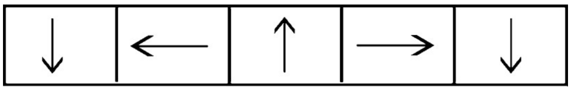

Figure 3.25: Halbach mangets disposition for an Outer Rotor Motor

This particular magnet configuration should improve the power and torque density of the machine by concentrating flux density.
Without changing any of the geometric dimensions of 1214 MkI the motor in Figure 3.26 is designed. The corresponding size and dimensions can be found in Table 3.8 and in Table 3.9. The motor is therefore obtained by only adding halbach magnets in empty spaces near north and south Permanent Magnets.
Looking carefully at the magnetization of the machine both in no load and in overload conditions in Figure 3.27(a) and in Figure 3.27(b), it is possible to see that the magnetic field lines tend to stay closer to the air-gap where the flux is more confined. It happens because of the halbach array implemented.

D_e	D	w_t	h_s	h_{wed}	h_{so}	w_{so}	S_{slot}	L_{stk}
100 mm	83 mm	7 mm	24 mm	4.5 mm	1.25 mm	1.5 mm	155.8 mm^2	27 mm

Table 3.8: Stator dimensions of 1214 MkII

D_e	L_{stk}	G_{tot}
100 mm	27 mm	1322 g

Table 3.9: Size of 1214 MkII

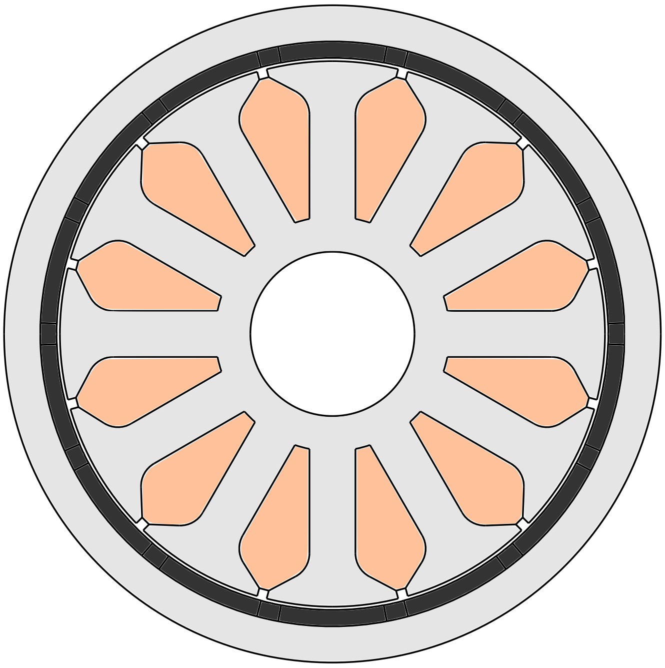

Figure 3.26: 1214 MkII drawing

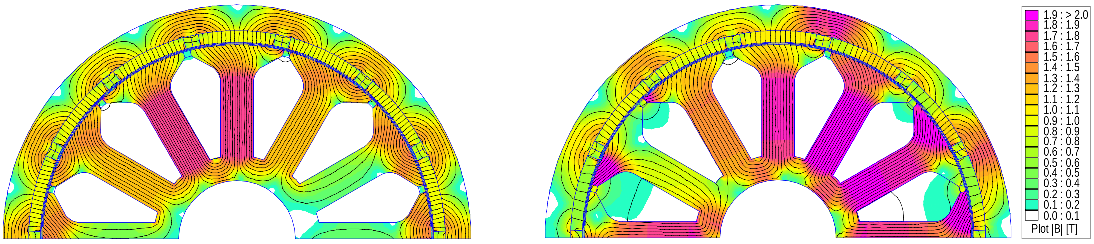

(a) (b)

Figure 3.27: FEA analysis **(a)** No load conditions **(b)** FOC Overload conditions

The result of such a configuration is hence an increase in the peak value of Permanent Magnet induction. This can be easily seen in Figure 3.28(a) where the sides of no load induction look boosted.

In Figure 3.28(b) it is possible to see a peak value of first harmonic equal to:

$$\hat{B_{g1}} = 1.2 \text{ T}$$

Compared to 1214 MkI, where peak value of the first harmonic of the magnetic field was $\hat{B_{g1}} = 1.099$ T, we get an increase of 0.1 T that is roughly 9% more. Increasing first harmonic air gap flux density an increase in torque should be highlighted.

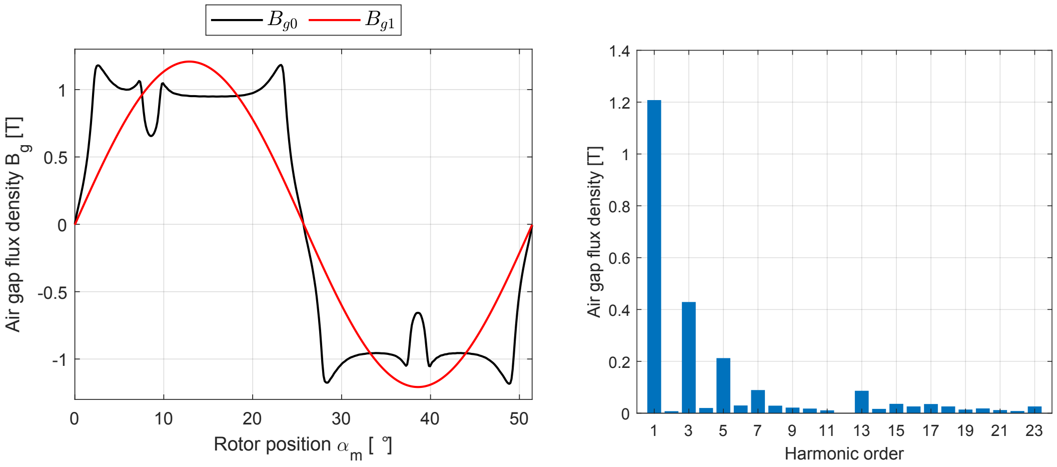

(a) (b)

Figure 3.28: No load induction **(a)** Zero and First order harmonics comparison **(b)** Harmonic spectrum

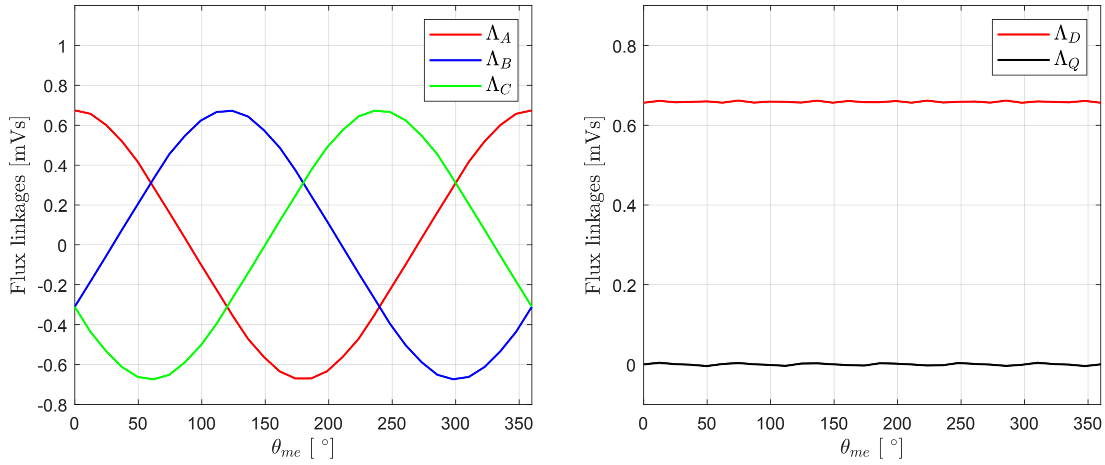

(a) (b)

Figure 3.29: No load fluxes **(a)** In abc reference **(b)** In dq reference

Also in this halbach configuration design the flux linkages are pretty clean and we can see low harmonics in both abc and dq flux linkages showed in Figure 3.29(a) and in Figure 3.29(b).

Torque capability of this halbach array motor is described in Figure 3.30 where torque corresponding to each current vector angle α_i^e is shown.

Comparing 1214 MkI and 1214 MkII it can be highlighted an increase in both nominal and overload torque thanks to the halbach array. With the halbach configuration it is possible to reach a nominal torque value of 4.185 Nm and an overload torque value of 11.85 Nm.

If a comparison with the same motor without halback configuration is carried out

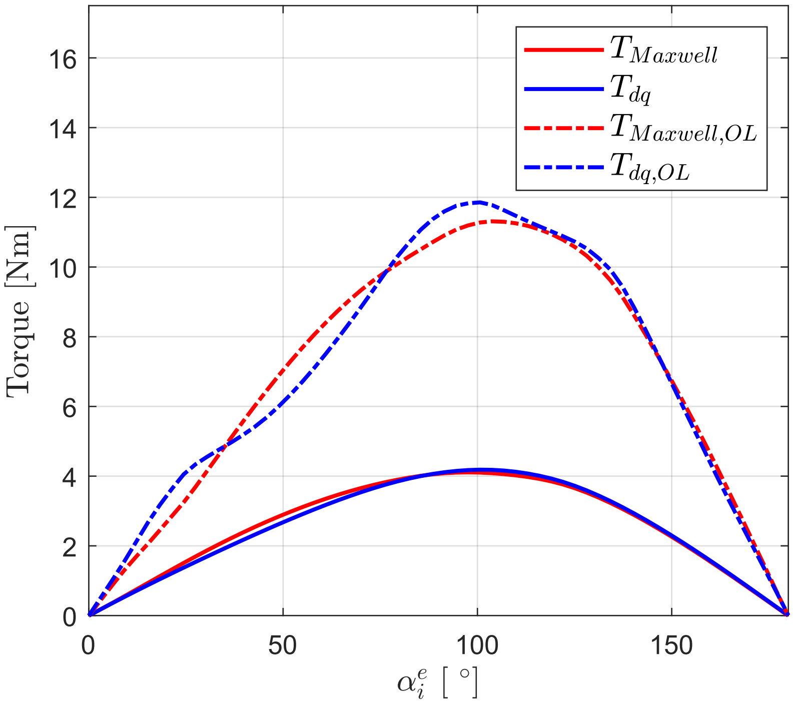

Figure 3.30: MTPA in nominal and overload conditions

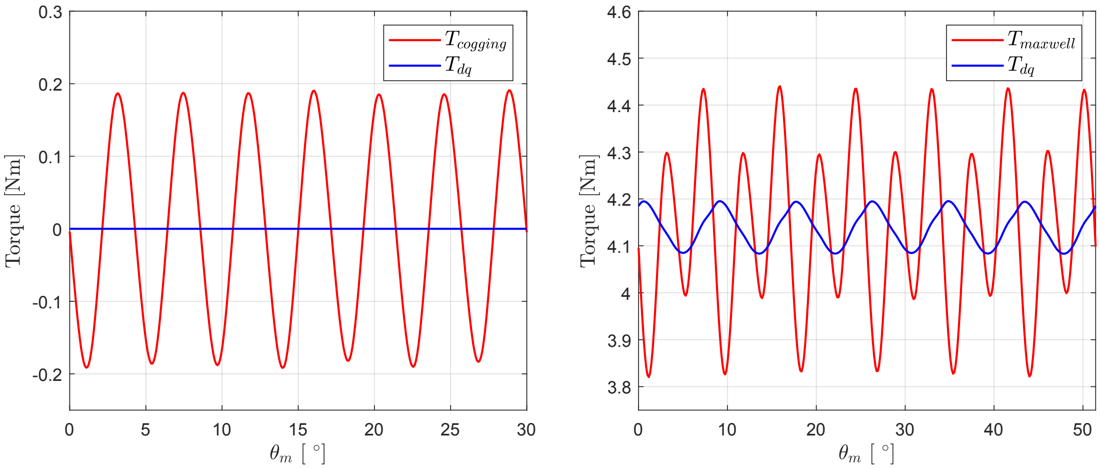

(a)

(b)

Figure 3.31: **(a)** Cogging torque **(b)** Torque ripple in nominal conditions

precisely, it is highlighted an increase of 11.6% in maximum torque which is quite a good result.

Cogging torque and torque ripple are shown in Figure 3.31(a) and Figure 3.31(b).

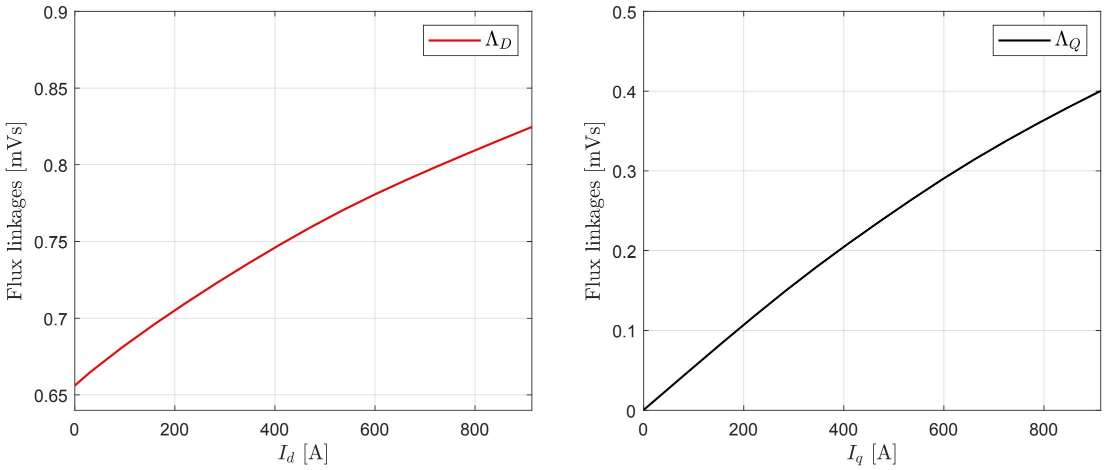

(a) (b)

Figure 3.32: Current range up to $1.5 \cdot I_n$ **(a)** Flux linkage with current vector on d-axis **(b)** Flux linkage with current vector on q-axis

If we focus on mean values it can be written:

$$\overline{T}_{Maxwell} = 4.137 \text{ Nm}$$
$$\overline{T}_{dq} = 4.139 \text{ Nm}$$

In no load functioning it is possible to see a cogging torque equal to:

$$\Delta T_{Maxwell} = 0.383 \text{ Nm}$$

Which compared to nominal torque obtained gives:

$$\frac{\Delta T_{Maxwell}}{\overline{T}} = 9.3\%$$

Instead dealing with torque ripple it can be highlighted an amplitude of:

$$\Delta T_{Maxwell} = 0.62 \text{ Nm}$$

Which compared to nominal torque values give:

$$\frac{\Delta T_{Maxwell}}{\overline{T}} = 14.5\%$$

In conclusion with an halbach configuration torque capability of the motor can be increased in a significant way.

The increase in first harmonic air gap density can also be noticed in Figure 3.32(a) where it can be seen a slight increase in d-axis saturation.

3.3 Outer Rotor SPM Motors Comparison

It is possible to draw a comparison among motors that have been designed. Such a comparison, where both torque capability of every designed motor is reported, is shown in Figure 3.33. The nominal mean torque values during a rotor rotation are reported in continuous stroke. Instead, the overload mean torque values are shown in dashed lines.

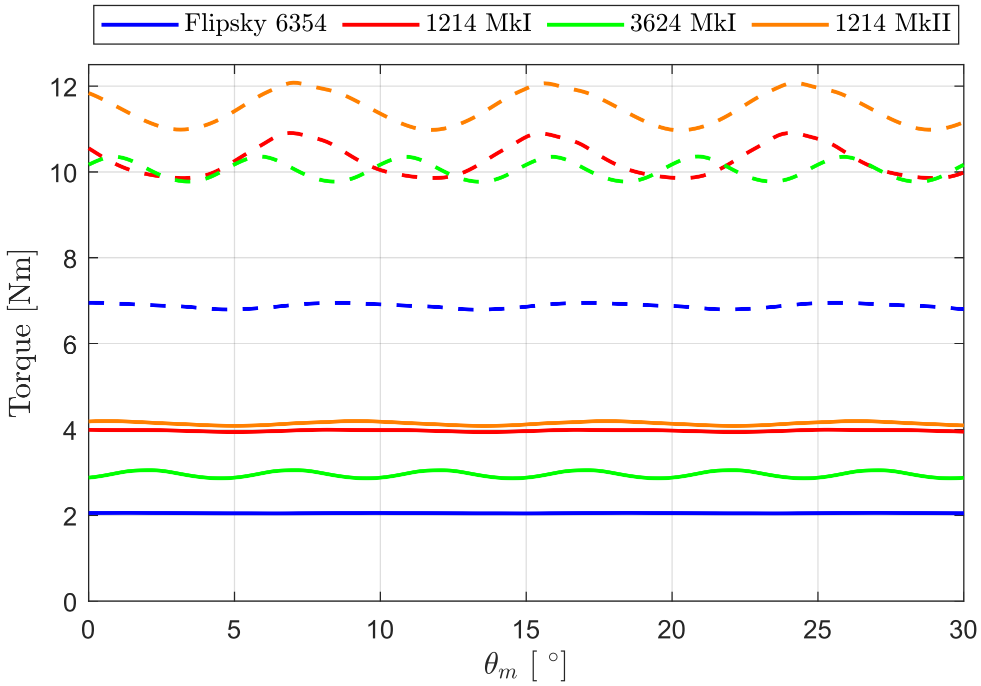

Figure 3.33: dq torque comparison of SPM Outer Rotor Motors designed

Clearly it can be seen that motors in a 12 slots and 14 poles configuration with both stack length reduction and halbach array produce the best results in terms of nominal torque. Instead, the motor with 3 slots for every 2 poles does not produce large nominal torque and, more importantly, has a very high torque ripple, even if only mean torque is considered. Furthermore it must be highlighed that with the torque also the weight of the motors increase. This means that torque to weight ratio is not improved in a remarkable way.

Drawing a comparison between the designed motors looking at torque density it is easy to highlight that each motor does not increase torque more than it increases its own weight. This comparison is shown in Table 3.10.

Despite not improving torque to weight ratio, it is possible to see that in terms of torque to volume ratio the designed motors show quite an improvement. For some of the designed motors torque to volume ratio nearly doubles. They are as heavy as the original motor, but with a much lower volume.

Feature	**Flipsky 6354**	**1214 MkI**	**3624 MkI**	**1214 MkII**
Nominal Torque [Nm]	2	4	2.95	4.13
Overload Torque [Nm]	7	10.6	10.2	11.85
Weight [kg]	0.64	1.265	0.943	1.322
Torque to weight ratio $\left[\frac{\text{Nm}}{\text{kg}}\right]$	3.125	3.162	3.128	3.124
Volume [l]	0.168	0.212	0.212	0.212
Torque to volume ratio $\left[\frac{\text{Nm}}{l}\right]$	11.9	18.86	13.9	19.48
Nominal Ripple [%]	13.3	9.4	105.7	14.5

Table 3.10: SPM Outer Rotor Motors Designed Comparison

Since the maximum overload torques of the designed motors are not high enough to allow a total removal of the gearbox it could be possible to use one of this motors in an implementation such as [24]. So one of this motors could be coupled with an epicyclic gearbox to build an assistive and light Exoskeleton that could help a user carrying some daily tasks out. In order to optimize such a design it could be lowered the overload coefficient and so the overload torque, resulting in the opportunity to tighten even more the teeth and the back irons. In other words it could be possible to reduce the peak torque to have a better performance in working points where there is no need for large torques. Clearly, this would work as an Assistive Exoskeleton, because to make the epyciclic gearbox work properly the maximum output torques must be pretty limited.

The same principle could be used with a cycloidal drive. As it is well explained in [8], such a design might be the right fit whenever size, inertia and efficiency of an Exoskeleton are the most important features.

3.4 Lightweight SPM Motor Design

If the Harmonic Drive, even though a bit heavy, is an unavoidable part of the actuator and the weight and size of the joint are not to be improved removing the gearbox, it may be possible to reduce them by reducing the power and the size of the motor itself. As it was shown in the previous Sections, the 1214 motor configuration has the best performance in terms of nominal torque and torque ripple. Since the good performance is linked to the periodicity of the motor, which is low, a new lighter motor is to be designed with the same periodicity and so a similar teeth-poles configuration.

3.4.1 2428 MkI Design

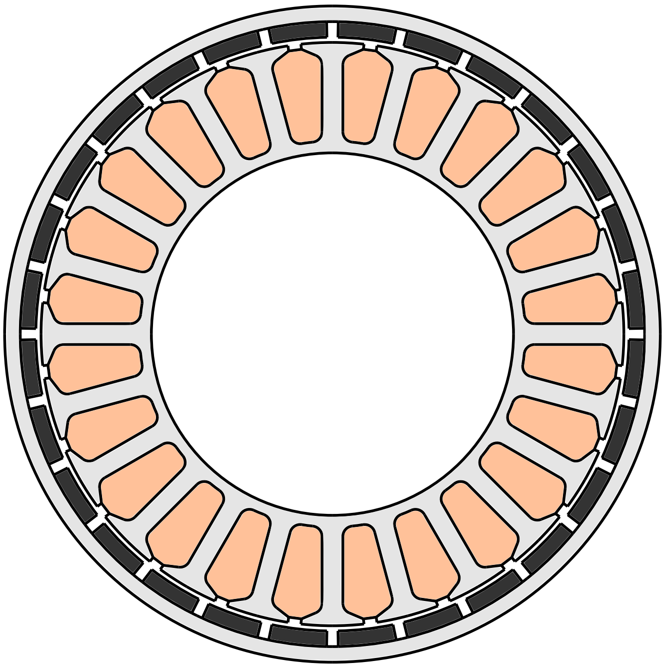

Figure 3.34: 2428 MkI drawing

D_e	D	w_t	h_s	h_{wed}	h_{so}	w_{so}	S_{slot}	L_{stk}
64 mm	56 mm	2 mm	9.5 mm	1 mm	0.5 mm	1.25 mm	33.6 mm^2	20 mm

Table 3.11: Stator dimensions of 2428 MkI

D_e	L_{stk}	G_{tot}
64 mm	20 mm	245 g

Table 3.12: Size of 2428 MkI

To improve both the axial length and the weight of the motor without causing a change in the joint that has already been designed, the lighter motor has the same external diameter of the Flipsky 6354 but the stack is shortened until torque performance is reached. To obtain an even lighter motor, the choice is to increase the number of poles, decreasing flux per pole and allowing to narrow both the rotor and the back-iron.

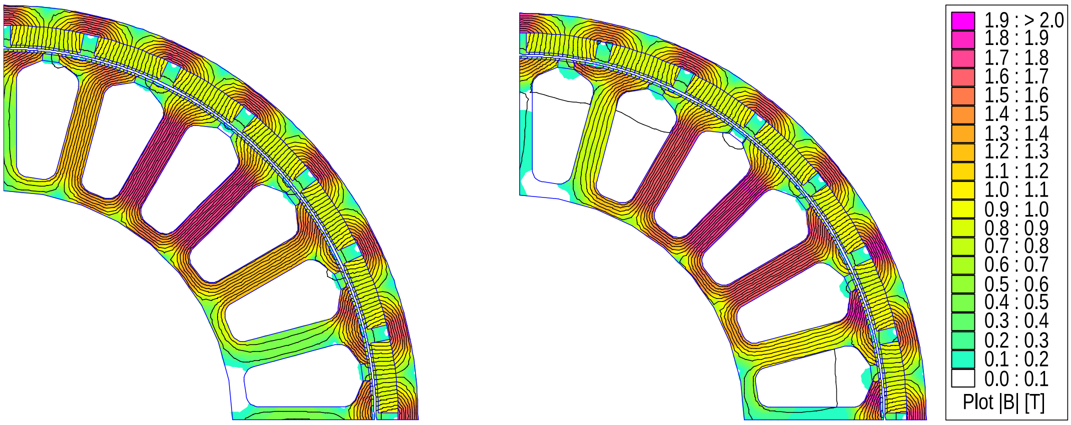

(a) (b)

Figure 3.35: FEA analysis **(a)** No load conditions **(b)** FOC Overload conditions

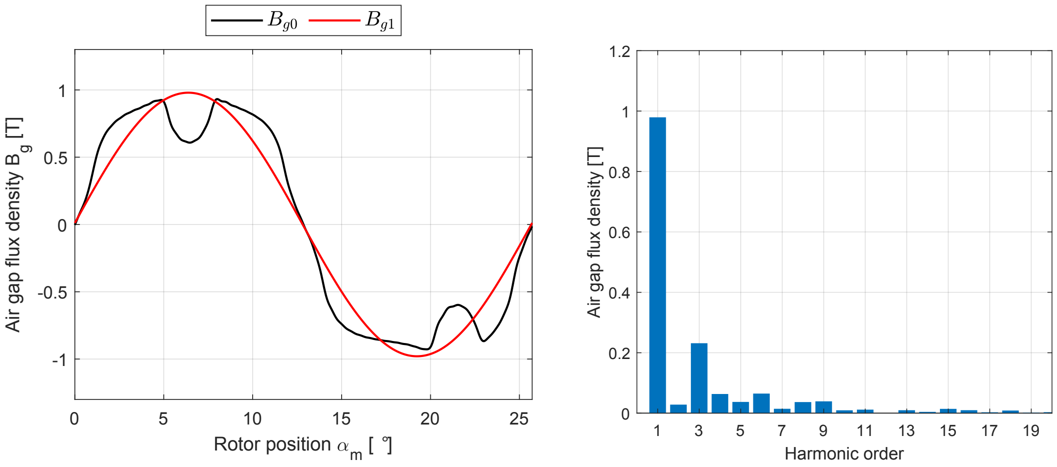

(a) (b)

Figure 3.36: No load induction **(a)** Zero and First order harmonics comparison **(b)** Harmonic spectrum

The motor is designed and a drawing is displayed in Figure 3.34, where the thin back-iron and rotor can be appreciated. The main dimensions of stator, rotor and teeth are shown in Table 3.11, while the size features are to be found in Table 3.12. The stack of the motor is quite flat with a total length of 20 mm, whereas the motor weighs just 245 g.

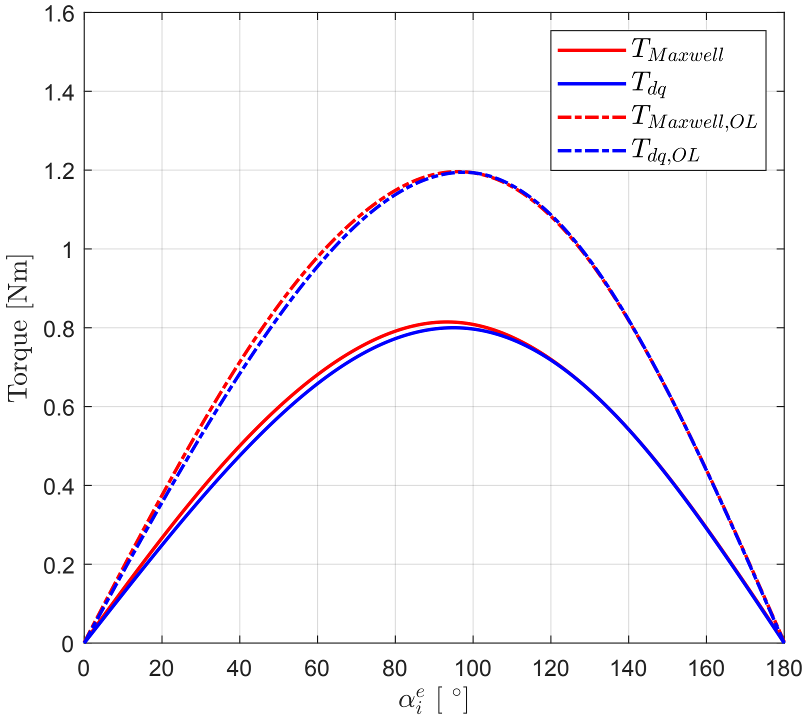

Figure 3.37: MTPA in nominal and overload conditions

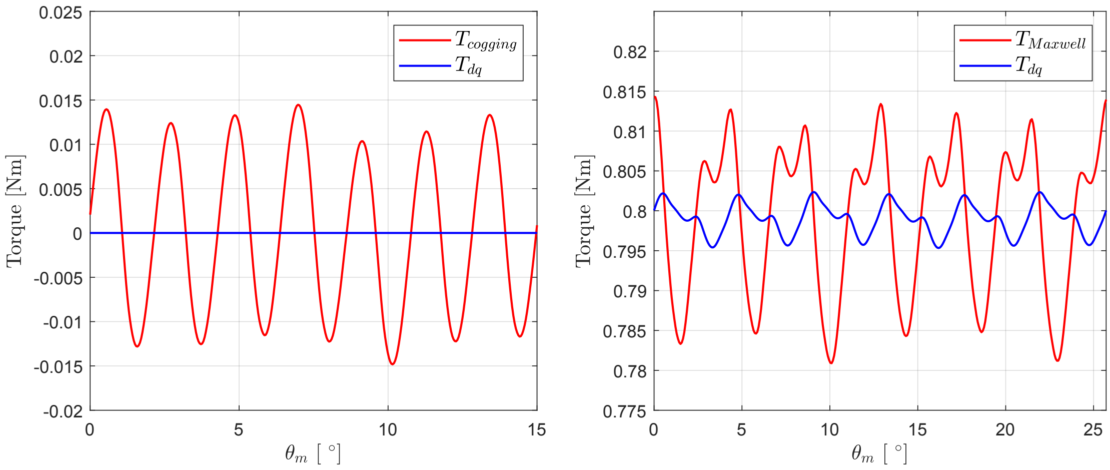

(a)

(b)

Figure 3.38: **(a)** Cogging torque **(b)** Torque ripple in nominal conditions

In Figure 3.35 the FEA analysis of the designed motor is shown and it can be seen a good exploitation of the iron with the motor that in overload conditions is pretty saturated.

In Figure 3.36 the no load air-gap flux density and the relative Fourier analysis is reported. The fundamental of the air-gap flux density has an amplitude of 0.98 T.

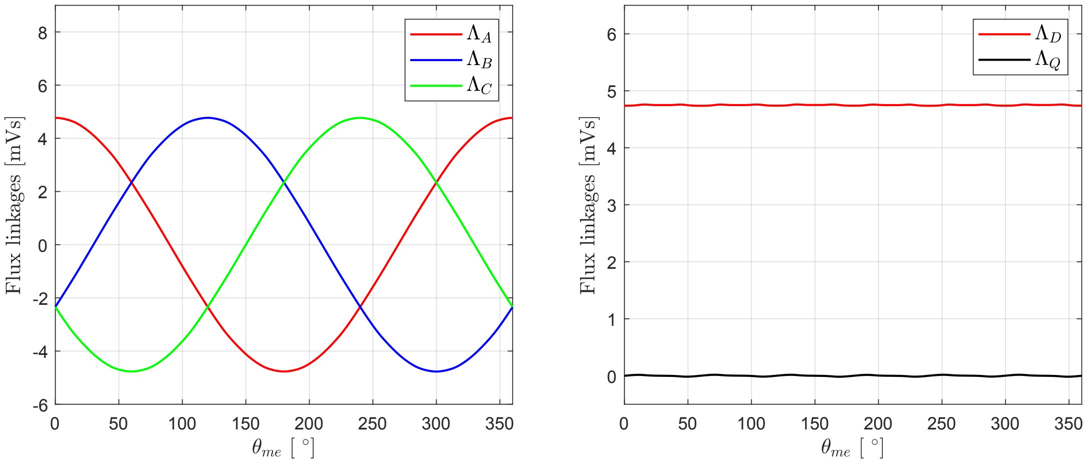

(a) (b)

Figure 3.39: No load fluxes **(a)** In abc reference **(b)** In dq reference

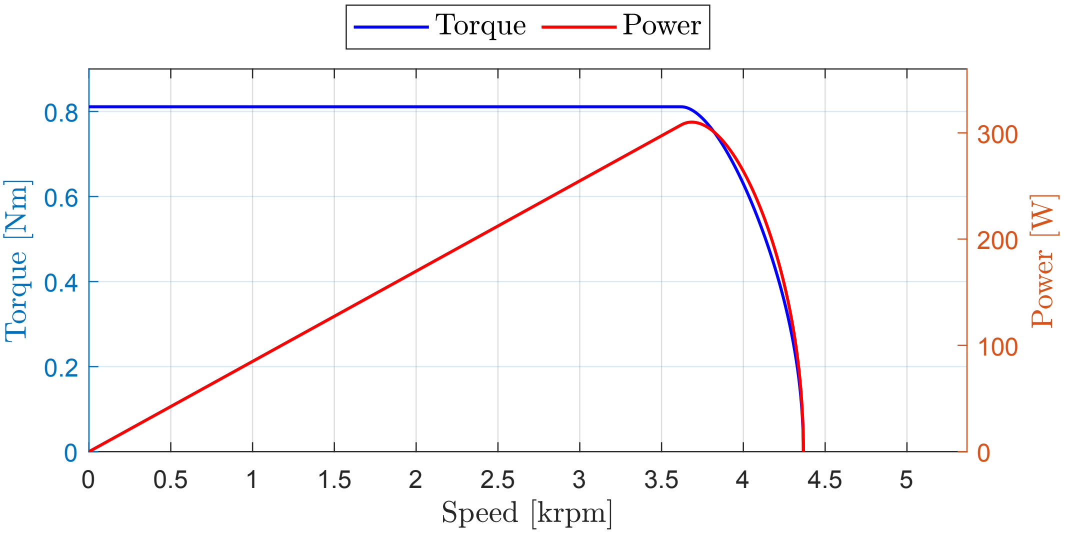

Figure 3.40: Mechanical characteristics reached in nominal current conditions

Even harmonics are present and are probably related to teeth effect.
In Figure 3.37 the torque capability of the motor is investigated. The machine with a current density $J_N = 7.2\ \frac{\mathrm{A}}{\mathrm{mm}^2}$ reaches the requirements of 0.8 Nm. With an overload coefficient of $k_{OL} = 1.5$ the requirement of overload torque are reached with a peak torque in MTPA conditions that reaches 1.2 Nm.
In Figure 3.38(a) the cogging torque of the motor is displayed, the torque ripple is displayed in Figure 3.38(b) instead. The cogging torque amplitude is equal to 0.0293 Nm that computes the 3.7% in respect with the nominal torque. The ripple amplitude is equal to 0.0334 Nm that in respect with the nominal torque gives a value of 4.2%.

The winding is then designed to reach a desired nominal speed. The number of conductors per slot is chosen equal to $n_c = 34$ with a number of parallel paths $n_{pp} = 2$. The no load flux linkages relative to the designed winding are reported in Figure 3.39. Thanks to the designed winding the mechanical characteristics in Figure 3.40 is reached. As it shown, the motor has a base speed of 3600 rpm circa. Then the performance loses quality in typical SPM motor fashion until the max speed is reached at around 4400 rpm.

3.4.2 2428 MkI Analysis

The designed motor is then analyzed in detail through mapping in the dq plane. Multiple simulations are carried out with different d and q axis currents. Torque,

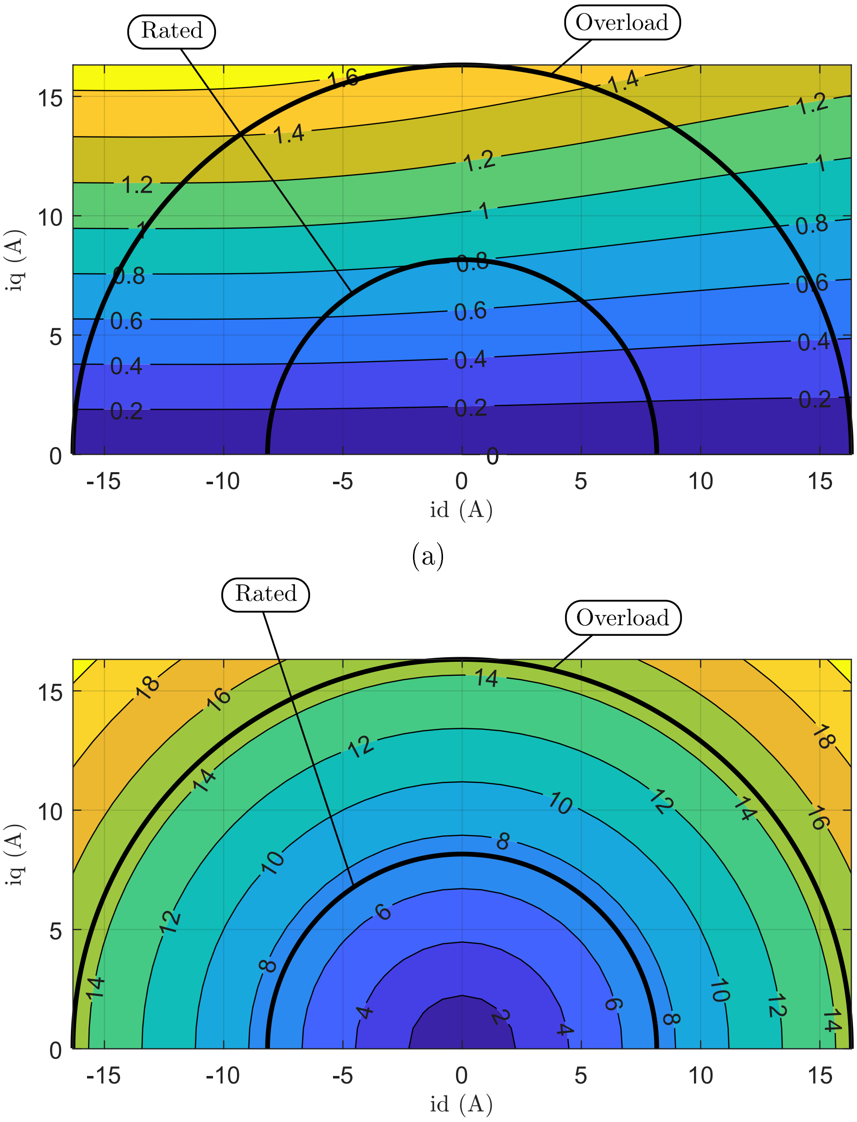

(a)

(b)

Figure 3.41: **(a)** Torque map in [Nm] **(b)** Current density map in $\left[\frac{\text{A}}{\text{mm}^2}\right]$

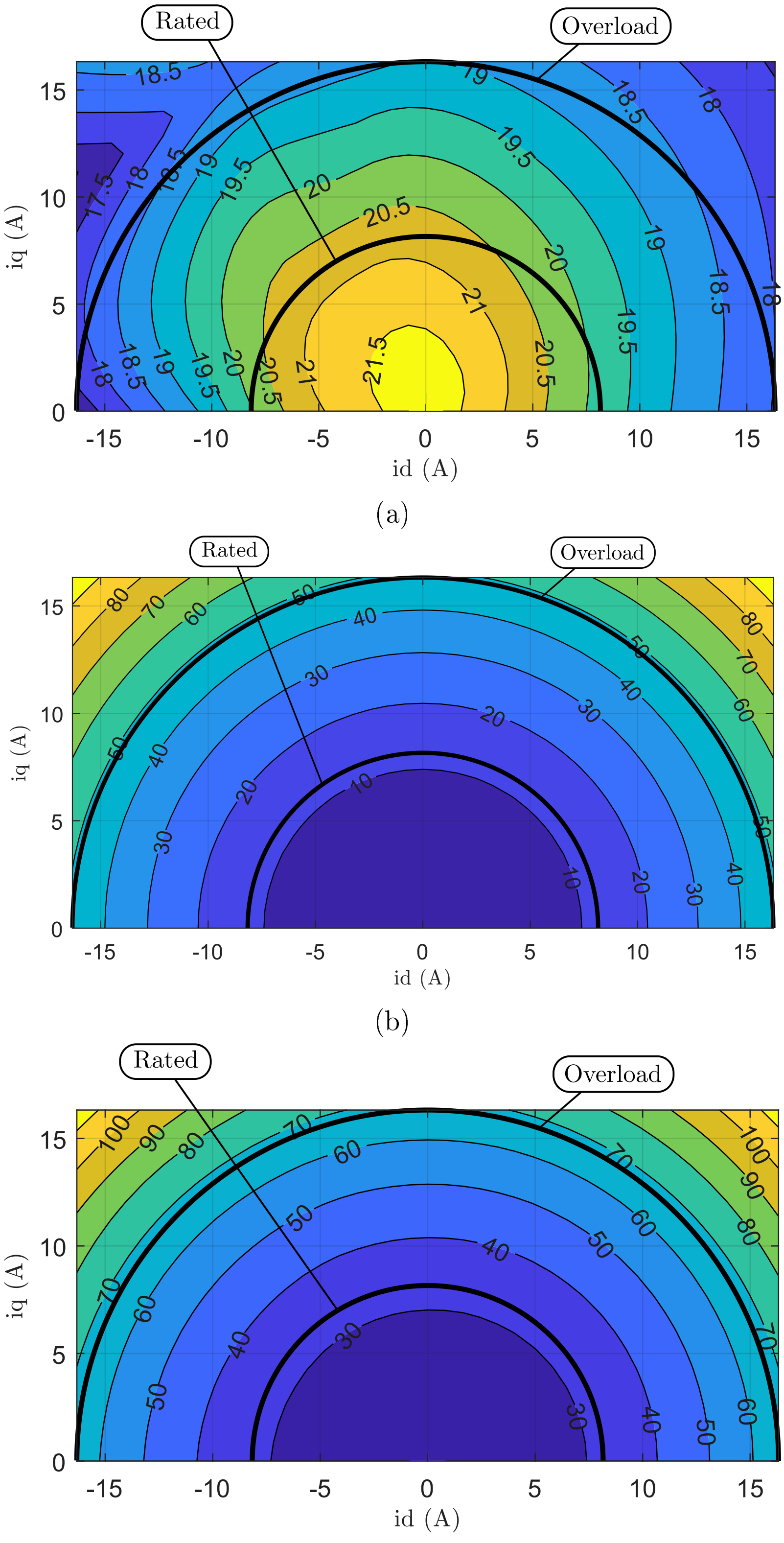

(a)

(b)

(c)

Figure 3.42: Losses map in [W] **(a)** Iron **(b)** Joule **(a)** Total

current density, losses and efficiency are computed. Overload value used for the analysis is increased from $k_{OL} = 1.5$ used in the design to $k_{OL} = 2$ to reach better the limits of the designed motor.

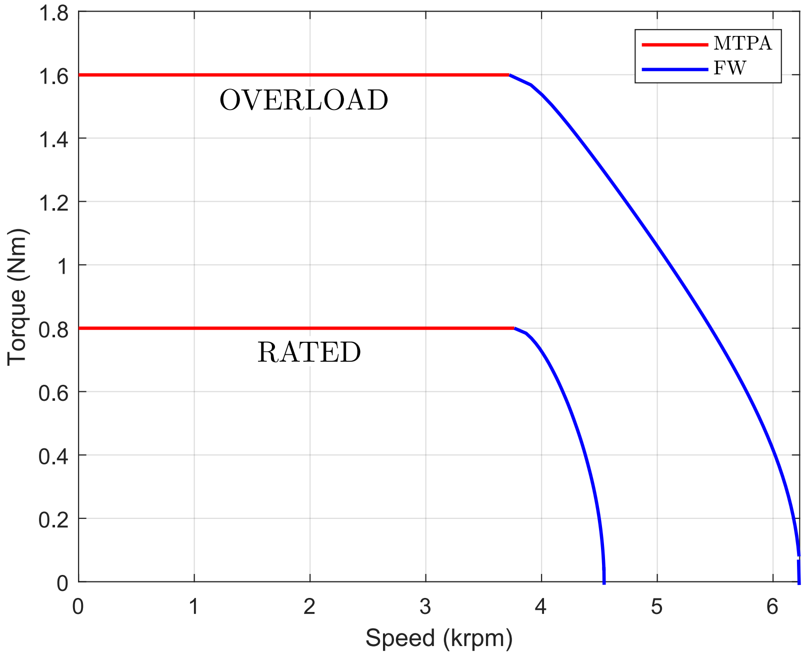

Figure 3.43: Torque versus speed characteristics in both nominal and overload conditions

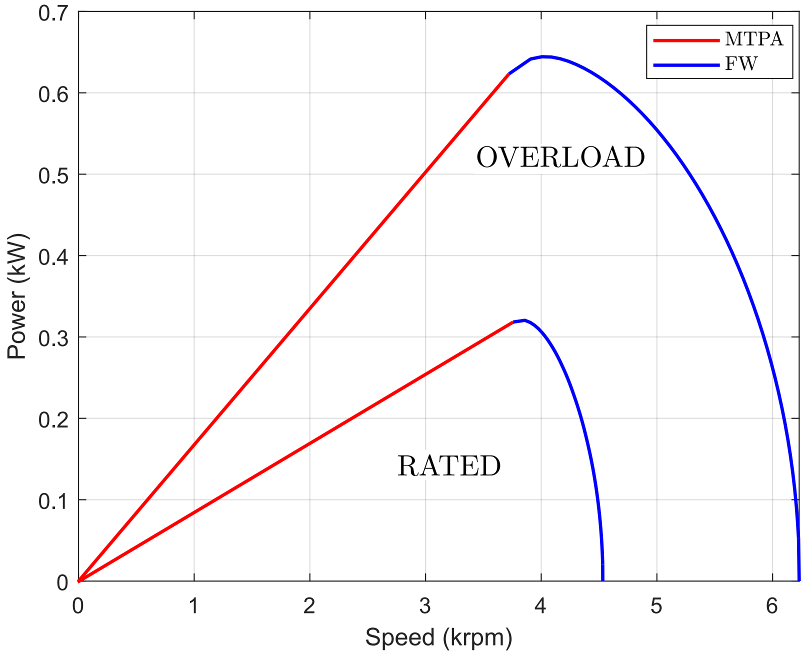

Figure 3.44: Power versus speed characteristics in both nominal and overload conditions

Figure 3.41(a) shows the torque values in the dq plane, whereas Figure 3.41(b) shows current density values in the dq plane. In the Figures the rotating nominal current vector draws the inner black circle. Instead, the outer black circle is drawn by the rotating overload current vector. In the torque map it is possible to see some saturation when the current reaches the overload value near FOC orientation

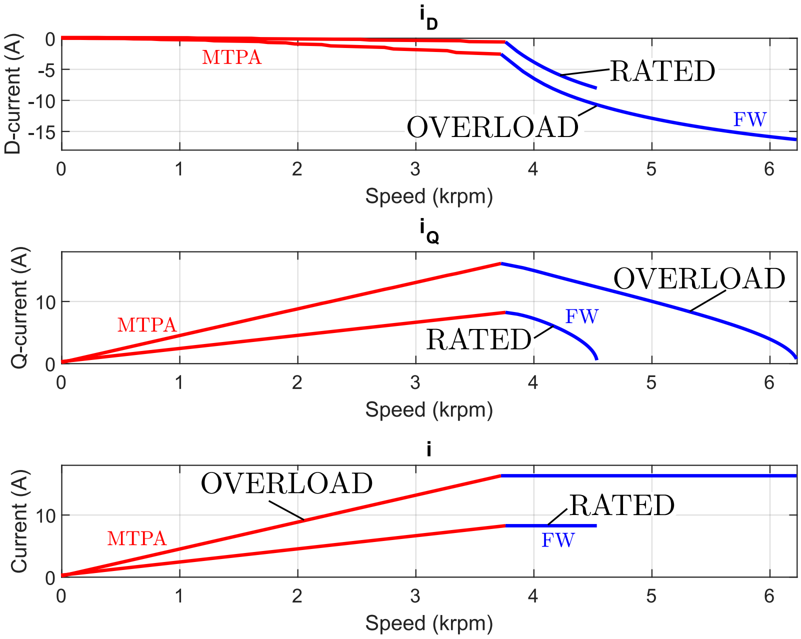

Figure 3.45: Currents versus speed characteristics in both nominal and overload conditions

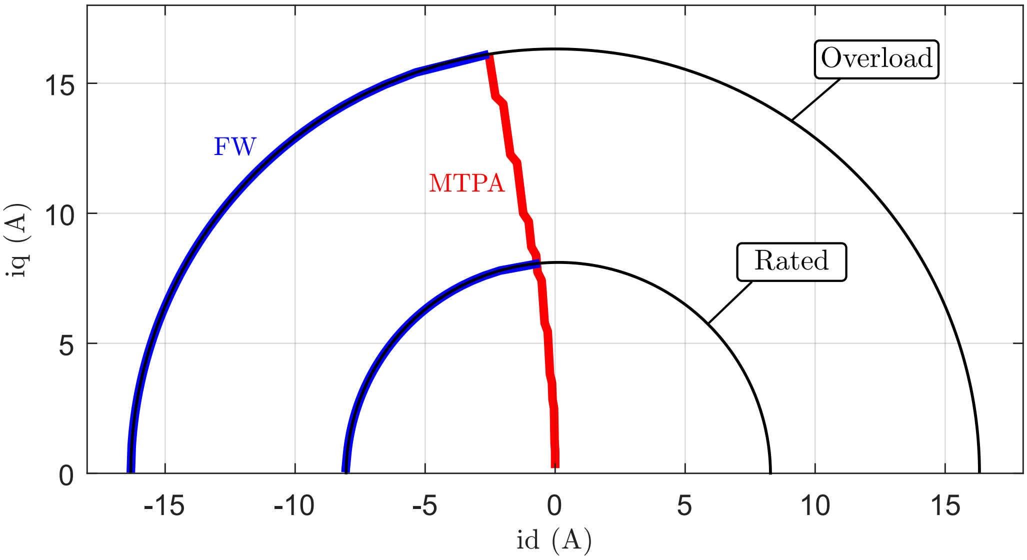

Figure 3.46: Current trajectory of MTPA in both nominal and overload conditions

conditions.

In Figure 3.42 the losses of the motor are investigated. Figure 3.42(a) shows the iron losses that increase with the speed. In Figure 3.42(b) Joule losses, linked to the currents, are reported. Finally, Figure 3.42(c) shows the total losses of the motor. Most of the losses are due to the current.

In Figure 3.43 and in Figure 3.44 the mechanical characteristics of the motor are investigated more deeply than in the design step, adding the behavior of the motor even in overload conditions. The analysis confirms the previous results well for both

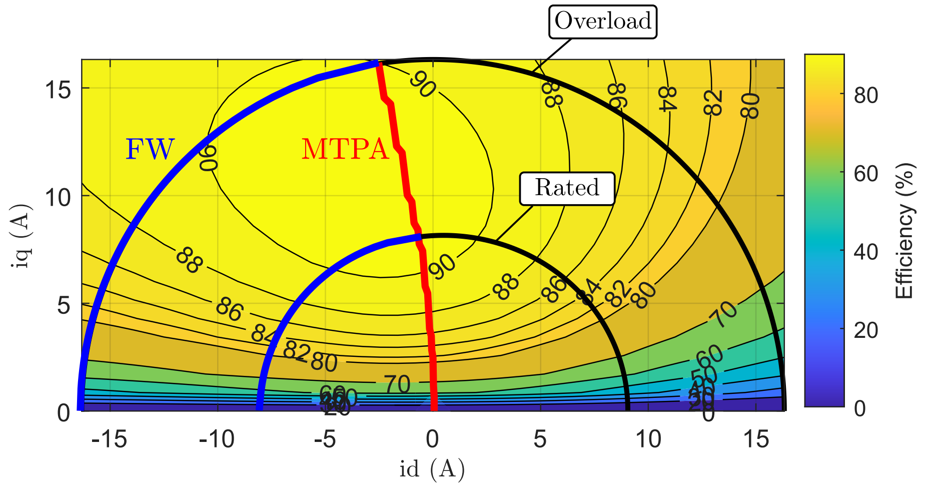

Figure 3.47: Efficiency map

the torque and the power.

In Figure 3.45 the current vector amplitude and his components d and q are depicted. The current vector increases until the max torque is reached, then the flux weakening starts and it is kept constant with only the angle increasing. It is possible to see the low value of the d component until the base speed is reached and the flux weakening begins, whereas the q component increases until the max torque is reached and then gets lower and lower. The behavior of the current vector in MTPA and flux weakening conditions is shown in Figure 3.46 as well.

In the end, Figure 3.47 shows an efficiency map of the motor. In the Figure, MTPA and FW (Flux Weakening) trajectories are highlighted. Moreover, it is possible to see the efficiency of the motor in every possible working point of the current. The MTPA and the first part of the FW trajectories cross the highest efficiency.

Chapter 4

Analysis and Design of Outer Rotor Vernier Motors

Implementing a magnetic gearing effect may help to reach the goals for the Exoskeleton Joint Actuator application, boosting torque and reducing size. If a simple SPM Motor does not have enough torque to allow the removal or substitution of the mechanical gearbox, it may be possible to embed a magnetic one into the motor.

4.1 SPM and Vernier Analysis and Comparison

To better understand the behavior of Vernier Machines and how to best analyze them a first simple design of a $Q_s = 36$ slots with $2p = 12$ poles is done. This motor has a classic winding with distributed overlapped coils. Based on this topology a Vernier Machine is designed through the computation of the rotor poles using (2.19) as it follows:

$$p_r = Q_s \pm p_s = 36 \pm 6 = 30$$

where the minus sign is chosen not to get a too high number of rotor poles. Through iterations a design of both motors to be compared is done.

D_e	D	w_t	h_s	h_{wed}	h_{so}	w_{so}	S_{slot}	L_{stk}
100 mm	83 mm	3.4 mm	14 mm	1 mm	0.75 mm	1.25 mm	32.6 mm^2	20 mm

Table 4.1: Stator dimensions of 3612 MkI

The dimensions and the size of 3612 MkI motor are shown in Table 4.1 and Table 4.2. Instead, the dimensions and the size of the corresponding Vernier Motor are shown in Table 4.3 and Table 4.4. Total and detailed drawings of both motors are

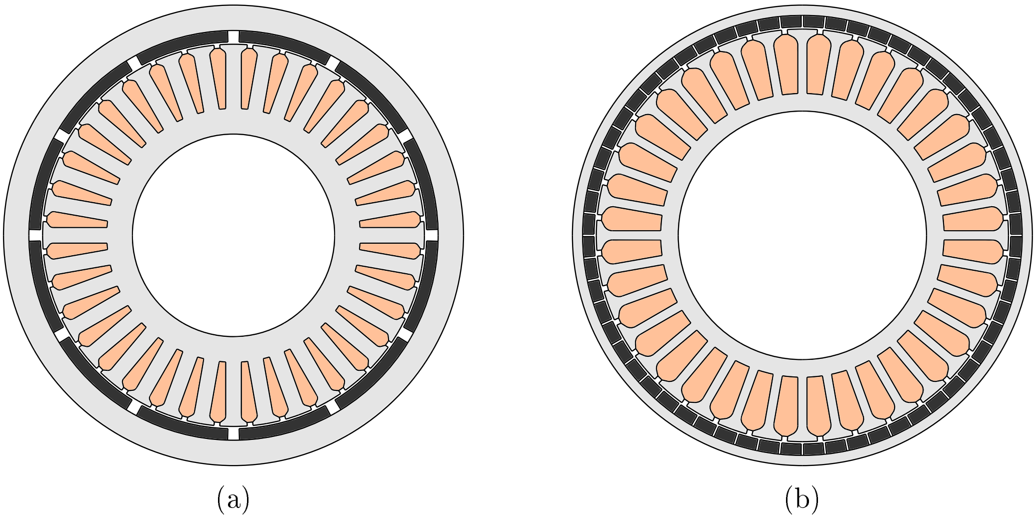

Figure 4.1: **(a)** 3612 MkI SPM Motor with overlapped winding **(b)** 3660 MkI Vernier Machine with overlapped winding

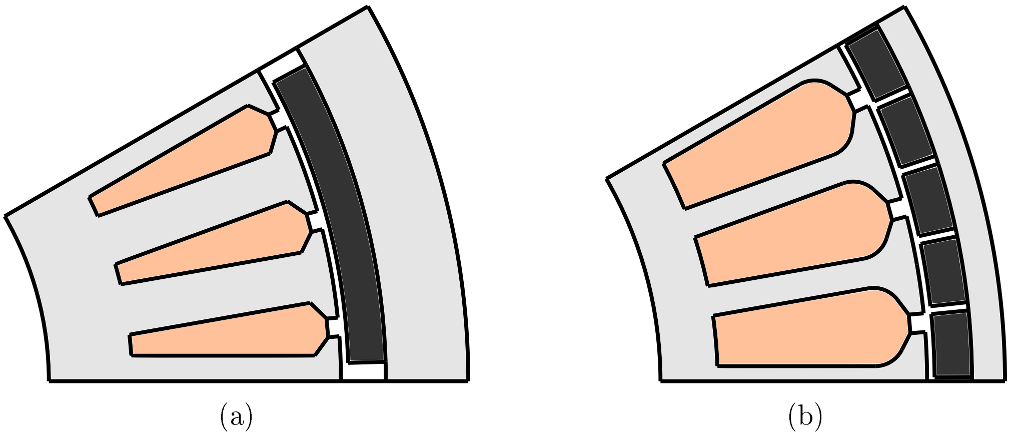

Figure 4.2: Teeth and magnets detail **(a)** 3612 MkI SPM Motor with overlapped winding **(b)** 3660 MkI Vernier Machine with overlapped winding

D_e	L_{stk}	L_{tot}	G_{tot}
100 mm	20 mm	54.6	992 g

Table 4.2: Size of 3612 MkI

D_e	D	w_t	h_s	h_{wed}	h_{so}	w_{so}	S_{slot}	L_{stk}
100 mm	89.6 mm	2.5 mm	14 mm	1.25 mm	1 mm	1.25 mm	55.33 mm^2	20 mm

Table 4.3: Stator dimensions of 3660 MkI

displayed in Figure 4.1 and in Figure 4.2.

In both cases the total length of the motor has been computed. The end winding influence on total motor length is pretty high. If the stack length is a key to optimize

D_e	L_{stk}	L_{tot}	G_{tot}
100 mm	20 mm	57.4	918 g

Table 4.4: Size of 3660 MkI

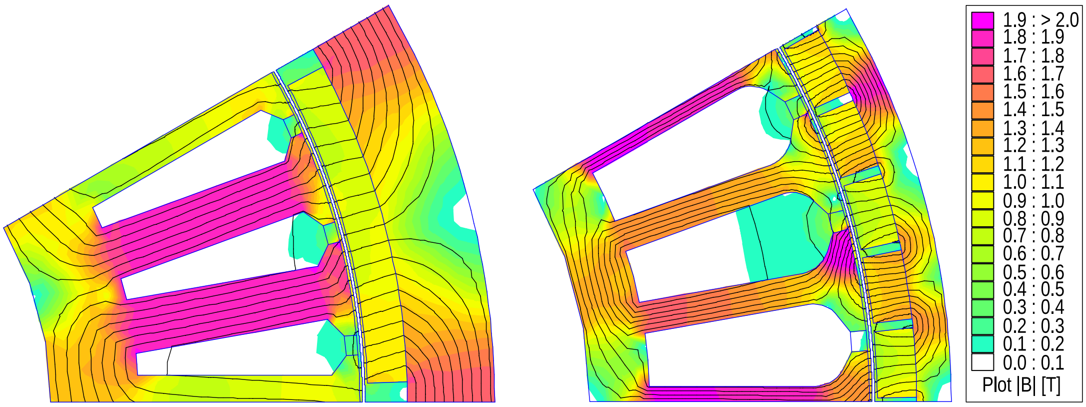
1.9 : > 2.0
1.8 : 1.9
1.7 : 1.8
1.6 : 1.7
1.5 : 1.6
1.4 : 1.5
1.3 : 1.4
1.2 : 1.3
1.1 : 1.2
1.0 : 1.1
0.9 : 1.0
0.8 : 0.9
0.7 : 0.8
0.6 : 0.7
0.5 : 0.6
0.4 : 0.5
0.3 : 0.4
0.2 : 0.3
0.1 : 0.2
0.0 : 0.1
Plot |B| [T]

(a) (b)

Figure 4.3: FEA analysis in FOC overload conditions **(a)** 3612 MkI **(b)** 3660 MkI

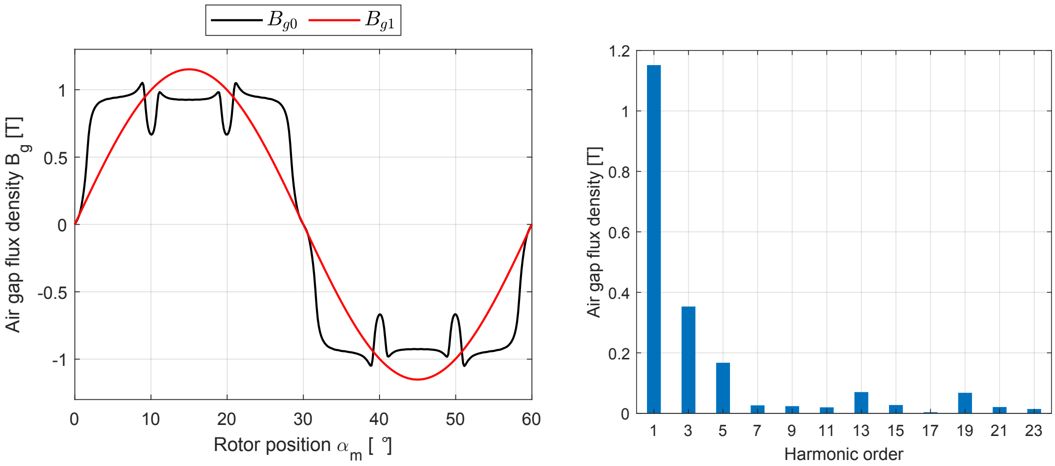

(a) (b)

Figure 4.4: No load induction of 3612 MkI **(a)** Zero and First order harmonics comparison **(b)** Harmonic spectrum

the project, it is clear that a classic distributed overlapped winding is not a feasible solution.

The magnetization of both machines in FOC overload conditions is shown in Figure 4.3. In Figure 4.4 it is shown that a motor with overlapped coils has quite low harmonics. As already said in Chapter 2, this has to do with the winding configuration of the motor. It can be found, comparing Figure 4.4 and Figure 4.5, an increase in harmonics of 3660 MkI Vernier Machine in respect with 3612 MkI motor.

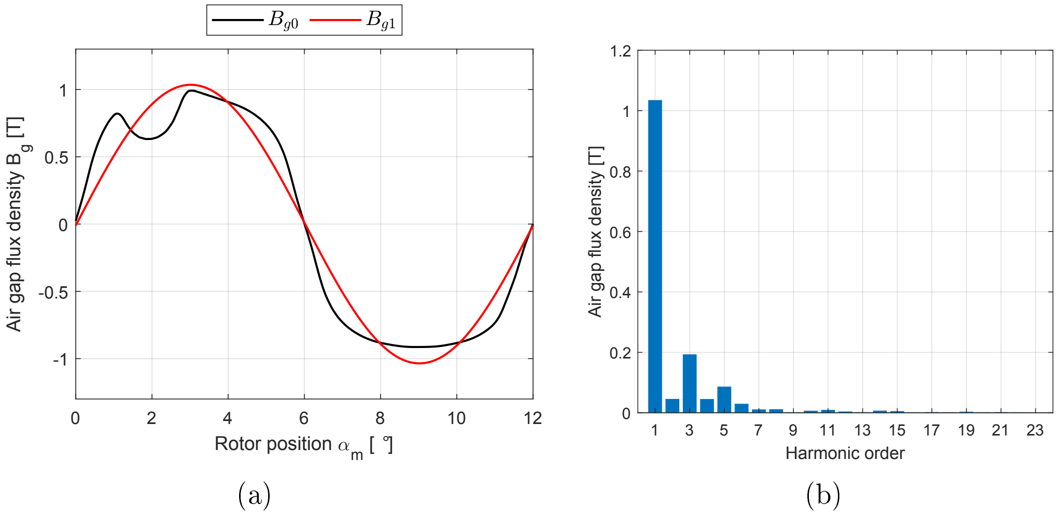

(a) (b)

Figure 4.5: No load induction of 3660 MkI **(a)** Zero and First order harmonics comparison **(b)** Harmonic spectrum

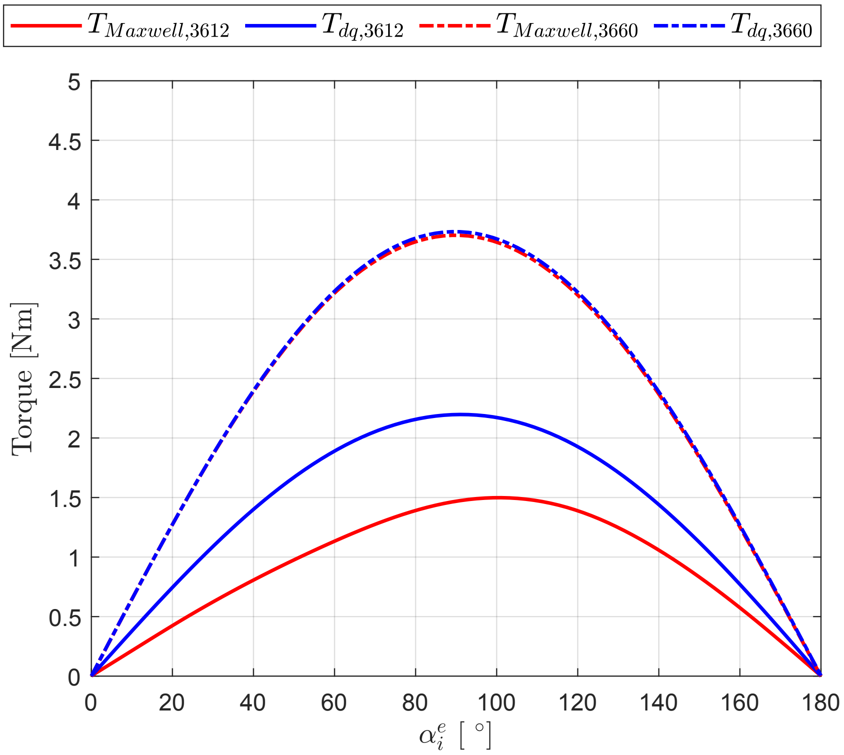

Figure 4.6: MTPA comparison of 3612 MkI and 3660 MkI in nominal conditions

In particular, it is clear that there are also even harmonics which were not present at all in the SPM Motor. These may be due to the teeth.

In Figure 4.6 torque performance is reported. Comparing 3612 MkI SPM Motor with 3660 MkI Vernier Motor it is possible to see that, with a current density of

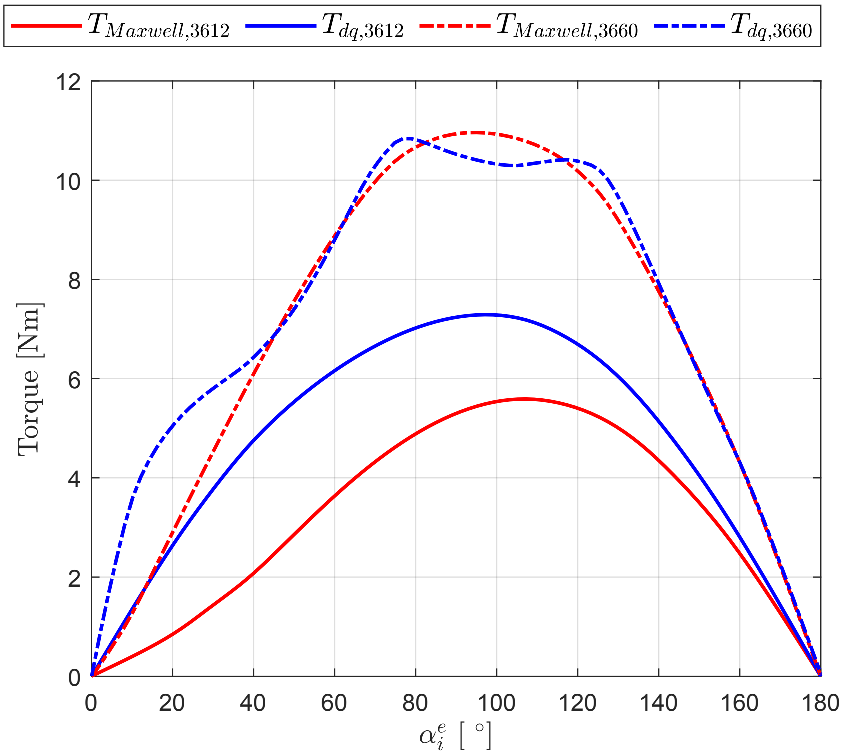

Figure 4.7: MTPA comparison of 3612 MkI and 3660 MkI in overload conditions

$J_N = 7\ \frac{\mathrm{A}}{\mathrm{mm}^2}$, peak torques in nominal conditions are respectively 2.19 Nm and 3.73 Nm. This is because in 3660 MkI a magnetic gearing effect is produced and because it has an higher air-gap diameter as well. With a simple calculation it is possible to see that the torque of the Vernier Motor is about 1.7 times the SPM Motor torque. This is in range with what was expected reading literature such as [16], [17], [25], [26], [27]. The explanation for this phenomenon can be found by looking at Figure 4.8. The Figure shows the winding coefficient of each harmonic of the electric loading. It is easy to see that the winding coefficient, that is equal to 1, is the same for the harmonics with 6 and 30 pole pairs. So the motor works by synchronizing the air-gap flux density produced by the rotor with an harmonic of the electric loading with an high winding coefficient.

However, as it can be seen in Figure 4.7 the Vernier Machine shows some saturation with an overload coefficient of $k_{OL} = 3.5$. MTPA in nominal conditions in both motors and overload conditions in 3612 MkI motor do not show anything like that. Looking at the FEA drawing in Figure 4.3 it can be seen the reason why this happens. In the Vernier Machine a lot of flux leakage is visible in the slot. Moreover, if focus is put on the flux density lines there are some low poles subharmonics that operate the saturation of the machine but do not produce torque.

A Fourier analysis in overload (and FOC) conditions is reported in Figure 4.9. In

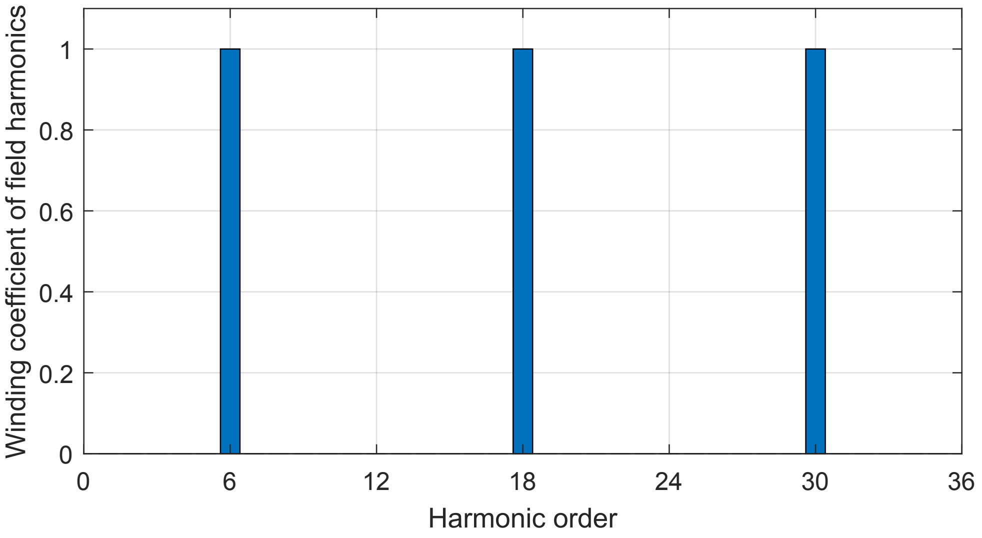

Figure 4.8: Electric loading harmonics of $Q_s = 36$ and $2p = 12$ winding

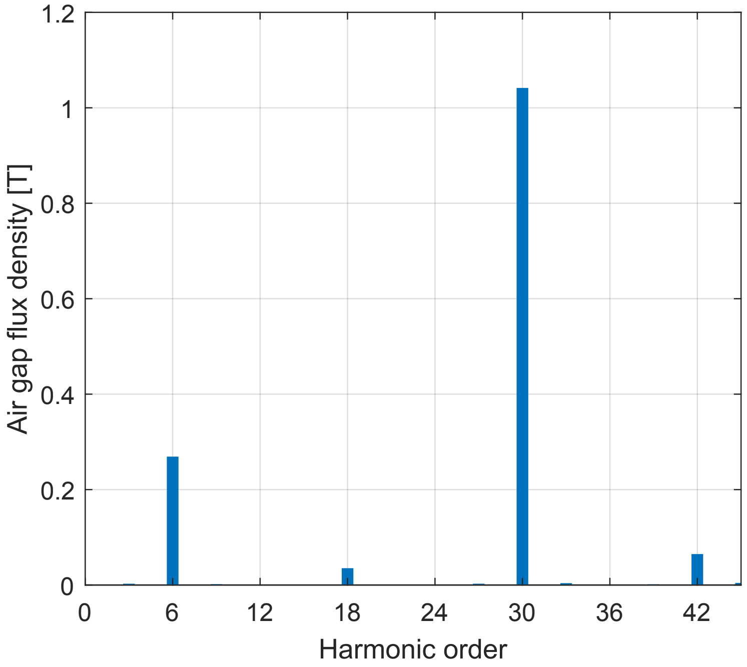

Figure 4.9: Harmonics and subharmonics of 3660 MkI in overload conditions

the Figure the two biggest harmonics are easy to spot. The one with $p = 30$ which is the torque related harmonic, and the smaller one, both in terms of pole pairs and amplitude, which has $p = 6$ and operates a big saturation of the motor without producing any torque. To better understand the phenomenon the harmonics and subharmonics of the motor with different loading conditions are investigated and reported in Figure 4.10. In the Figure the blue bars refer to the harmonics that are due only to the magnets of the motor, the red bars refer to the harmonics that are

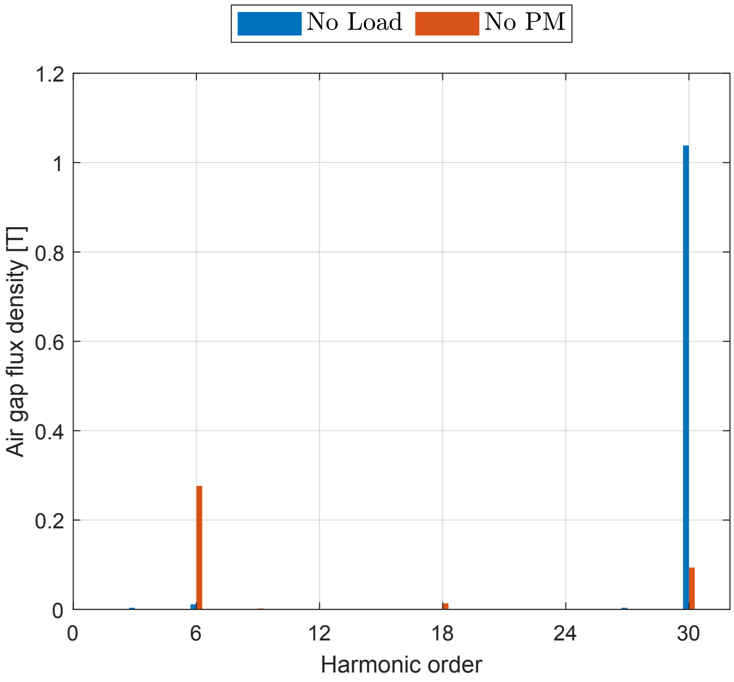

Figure 4.10: Harmonics and subharmonics of 3660 MkI in different electric and magnetic load conditions

due to the electric loading of the machine.

In this particular motor the saturation arises only in the case of a high overload. Once more, this is due to the low pole pairs harmonics and subharmonics related to the overlapped winding.

4.2 Outer Rotor Vernier Motor Prototypes

4.2.1 1238 MkI: Vernier Machine without flux modulator

The design of the Vernier Machine begins with the choice of the same size characteristics of the 1214 configuration motors previously designed and analyzed. So the axial length and the external diameter are reported in Table 4.6. Being this a Vernier Machine without a modulating grill, the number of teeth must operate the flux modulation. A fractional slot winding is preferred to keep a low total length of the motor so a $Q_s = 12$ and $2p_s = 14$ configuration is chosen again, given the high torque and low ripple already demonstrated.

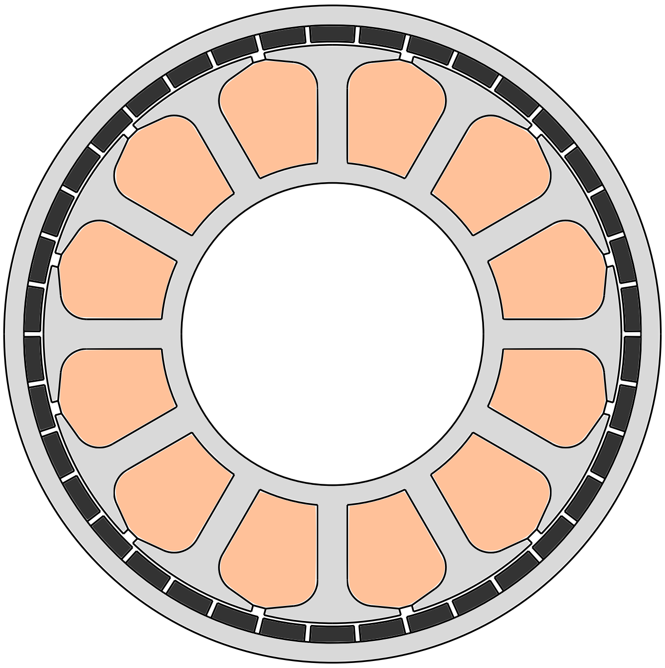

Figure 4.11: 1238 MkI drawing

D_e	D	w_t	h_s	h_{wed}	h_{so}	w_{so}	S_{slot}	L_{stk}
100 mm	88 mm	4.5 mm	18 mm	2 mm	1 mm	2 mm	207 mm^2	27 mm

Table 4.5: Stator dimensions of 1238 MkI

D_e	L_{stk}	G_{tot}
100 mm	27 mm	963 g

Table 4.6: Size of 1238 MkI

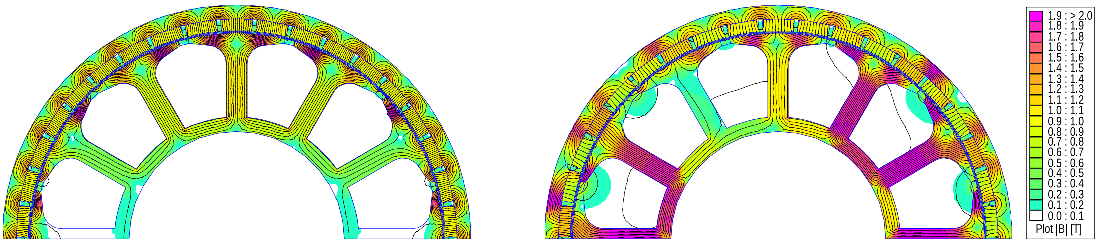

(a) (b)

Figure 4.12: FEA analysis **(a)** No load conditions **(b)** FOC Overload conditions

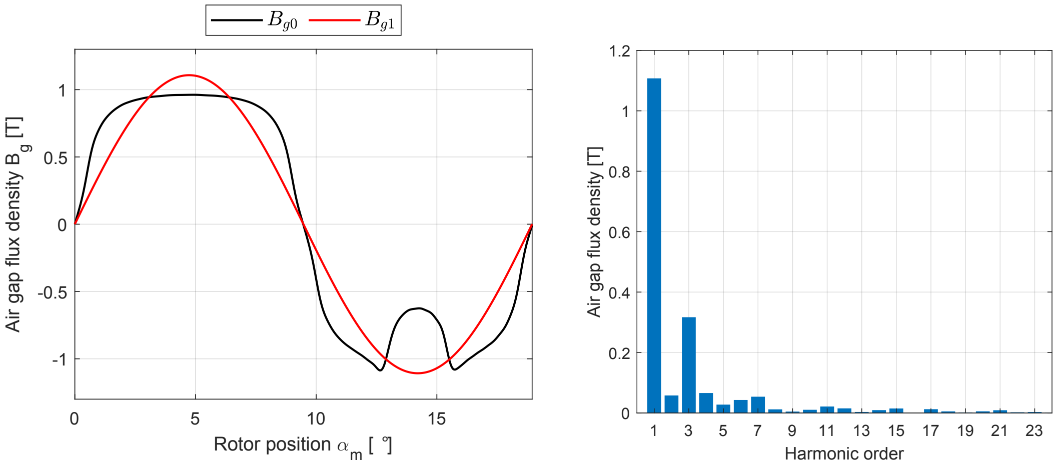

(a) (b)

Figure 4.13: No load induction **(a)** Zero and First order harmonics comparison **(b)** Harmonic spectrum

The number of rotor pole pairs is computed as:

$$p_r = Q_s \pm p_s = 12 \pm 7 = 19$$

where the plus sign is chosen to allow a bigger pole ratio and so to increase torque. Starting from 1214 configuration through some iterations a design is carried out. Much focus is put on minimizing the amount of saturation of teeth and back iron. This is important not to compromise the overload torque performance as already discussed. The ultimate design is reported in Figure 4.11. The final dimensions of the motor are displayed in Table 4.5. It can be appreciated a smaller size of teeth and external rotor diameter. It is because of the higher number of poles. In Table 4.6 the total weight of the motor is displayed as well.

In Figure 4.12 the FEA analysis of the 1238 MkI motor is shown. In particular in Figure 4.12(a) the no load analysis is displayed, in fact all the poles can be appreciated looking at the flux lines. Instead, in Figure 4.12(b) the analysis is carried out in FOC overload conditions, it can be appreciated both the saturation and the flux

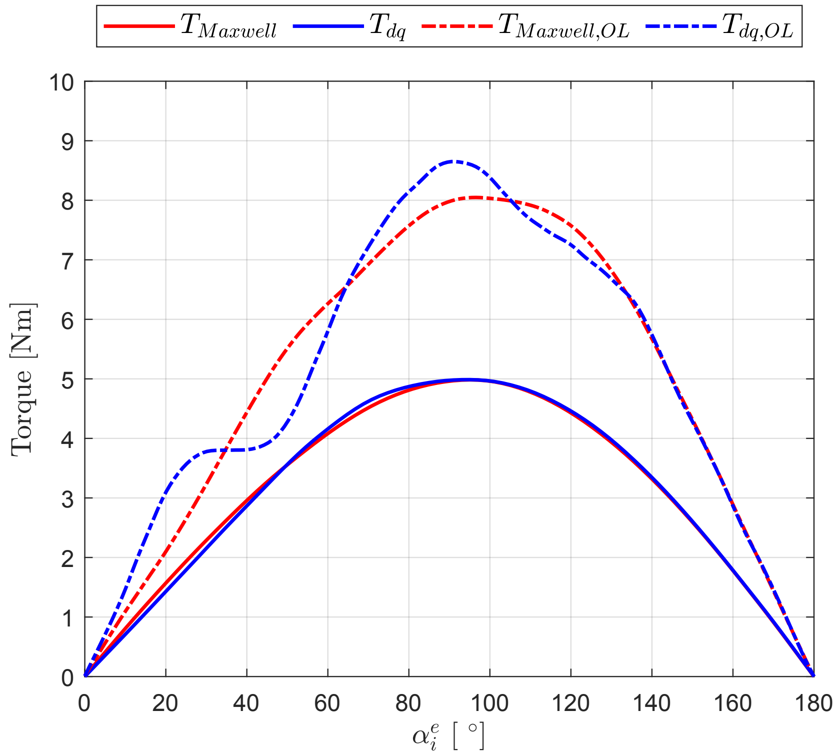

Figure 4.14: MTPA in nominal conditions and overload conditions

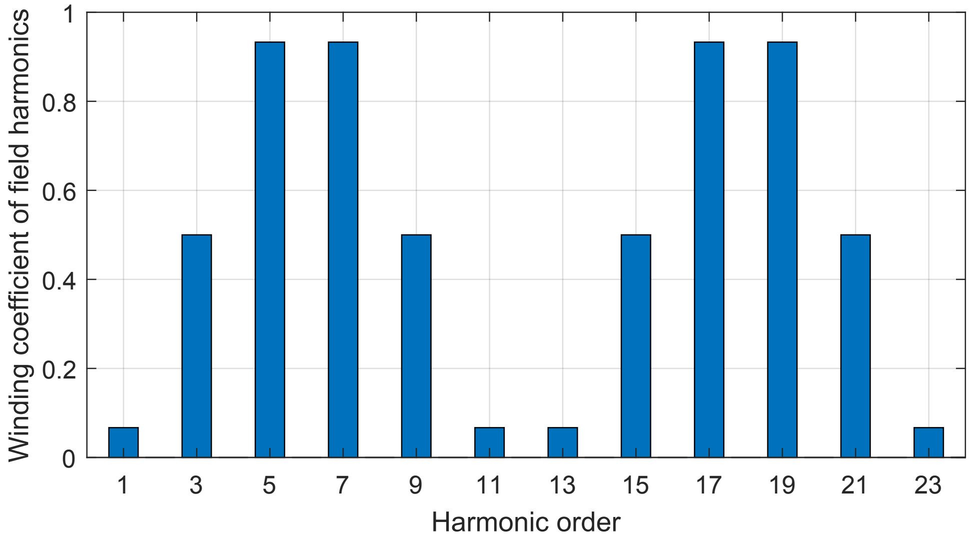

Figure 4.15: Electric loading harmonics of a $Q_s = 12$ and $2p = 14$ winding

leakage that is typical of these motor topologies.

In Figure 4.13 the no load air-gap induction is presented. In Figure 4.13(a) there is the comparison with the first order harmonic and in Figure 4.13(b) there is the main part of the Fourier analysis. There are both even and odd harmonics, with the even ones probably due to the teeth influence.

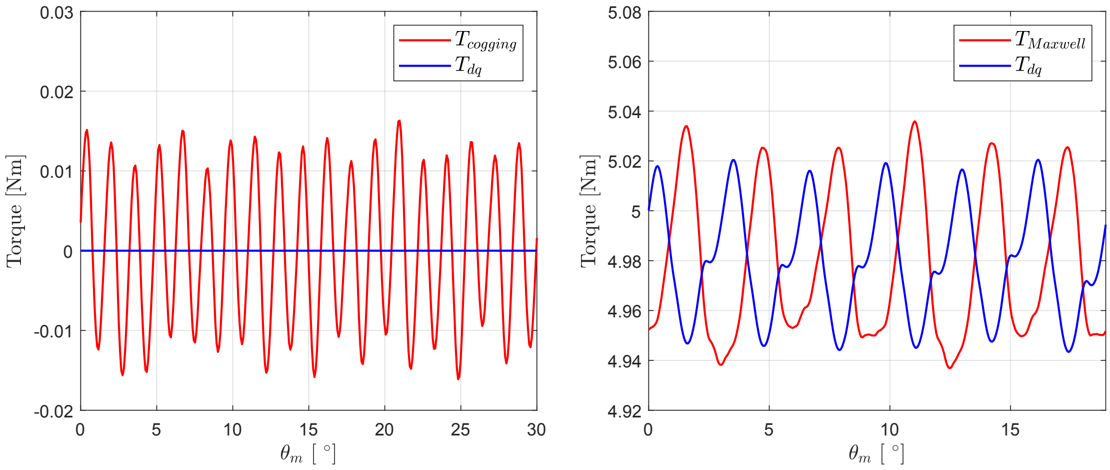

(a)

(b)

Figure 4.16: **(a)** Cogging torque **(b)** Torque ripple in nominal conditions

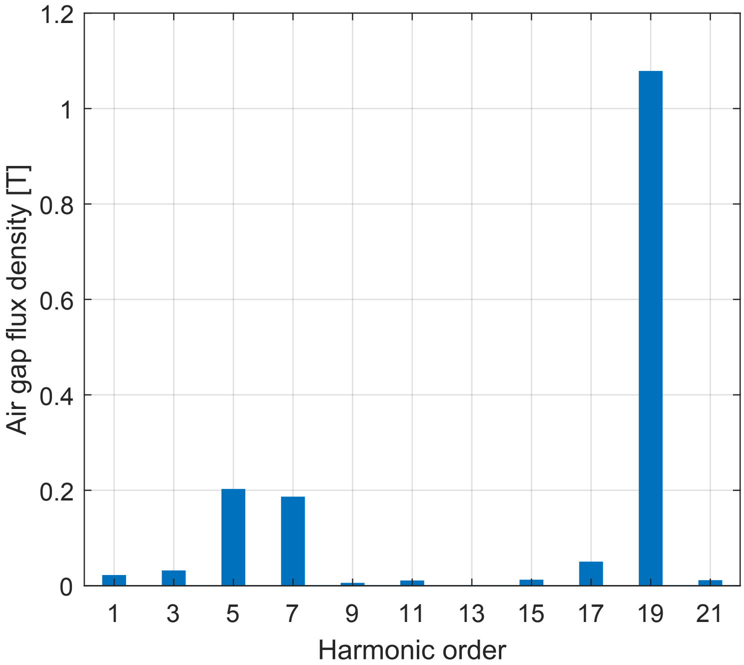

Figure 4.17: Harmonics and subharmonics of 1238 MkI in overload conditions

In Figure 4.14 the torque performance of the motor is displayed. The motor with a current density of $J_N = 7\ \frac{\mathrm{A}}{\mathrm{mm}^2}$ reaches a maximum torque of 5 Nm. The torque to weight ratio is equal to 5.2 $\frac{\mathrm{Nm}}{\mathrm{kg}}$, quite a good result. Looking at Figure 4.15 it is possible to see that, apart from the 7 pole pairs which is the typical rotor configuration, the 19 pole pairs electric loading harmonic has an high winding coefficient as well. The rotor will synchronize on this electric loading harmonic and so it will produce an higher torque.

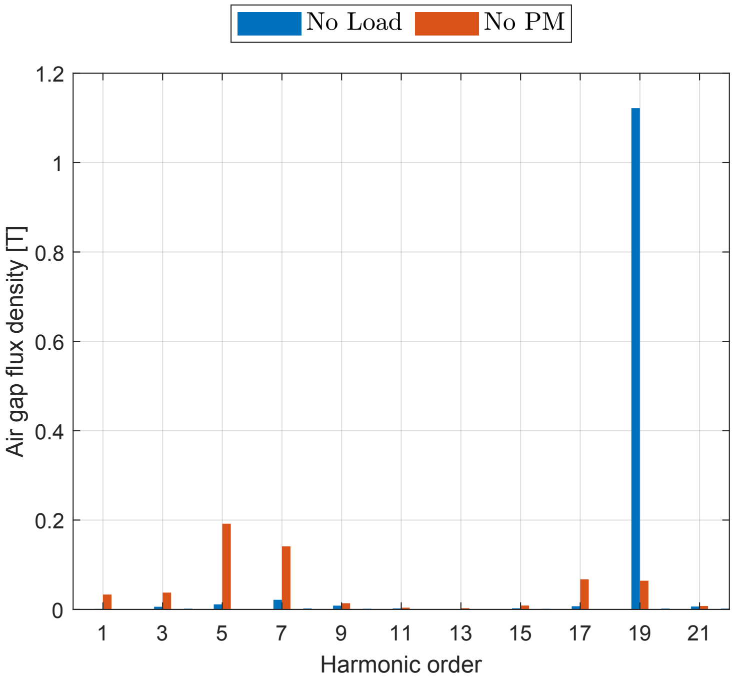

Figure 4.18: Harmonics and subharmonics of 1238 MkI in different electric and magnetic load conditions

Even though the nominal torque is as good as expected it must be highlighted that in overload conditions, even lowering the overload coefficient to $k_{OL} = 2.5$, the torque MTPA curve shows quite some signs of saturation. This is, as explained in the previous Section, due to the amount of subharmonics that are related to this motor topology. In Figure 4.16 the cogging torque and the torque ripple in nominal conditions are displayed. They are both quite low, especially the torque ripple, probably due to the high nominal torque produced by the motor.
To look into the saturation phenomenon the Fourier analysis of the motor air-gap flux density in overload conditions is reported in Figure 4.17. It can be appreciated how there is not only the $p_s = 7$ subharmonic, but there are many others and some of them relevant. This is due to the fractional slot winding, as explained in [10]. All this subharmonics tend to saturate the machine even more than what happened with the overlapped coil Vernier Machine. A more detailed analysis of the phenomenon is given in Figure 4.18, where the blue bars are the harmonics linked to the magnets, intead the red bars are the harmonics linked to the electric loading in overload conditions.

4.2.2 1270 MkI: Vernier Machine with flux modulator

A Vernier Machine with the flux modulator is also designed. It is designed with the same size constraints that were used in the previous Vernier Motor and in the previous Section. They are summarized in Table 4.7. The stator winding is kept the same to have a good fractional slot winding configuration and also to help compare the design with some previous ones. Because of the modulator presence in this case the number of stator teeth can be free and the number of elements of the grill must be computed as:

$$z_g = p_s + p_r = 7 \pm 35 = 42$$

where the number of rotor poles is chosen freely to get an high pole ratio.

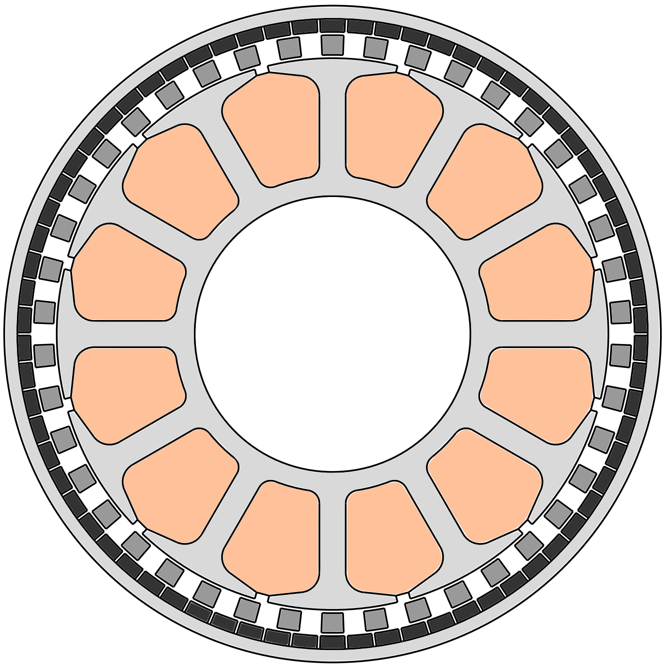

Figure 4.19: 1270 MkI drawing

D_e	D	w_t	h_s	h_{wed}	h_{so}	w_{so}	S_{slot}	L_{stk}
100 mm	84 mm	4 mm	18 mm	2 mm	1 mm	2 mm	199.7 mm^2	27 mm

Table 4.7: Stator dimensions of 1270 MkI

D_e	L_{stk}	G_{tot}
100 mm	27 mm	920 g

Table 4.8: Size of 1270 MkI

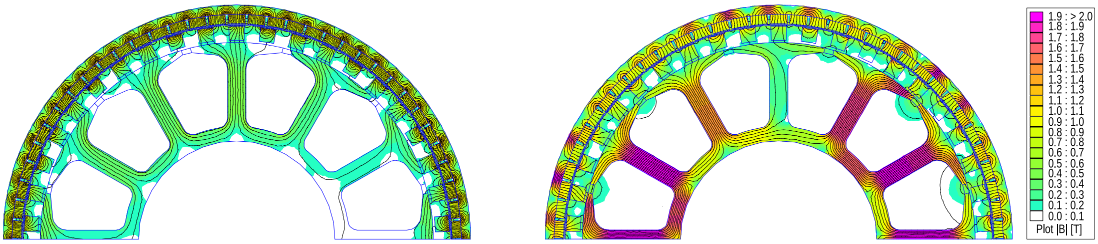

(a) (b)

Figure 4.20: FEA analysis **(a)** No load conditions **(b)** FOC Overload conditions

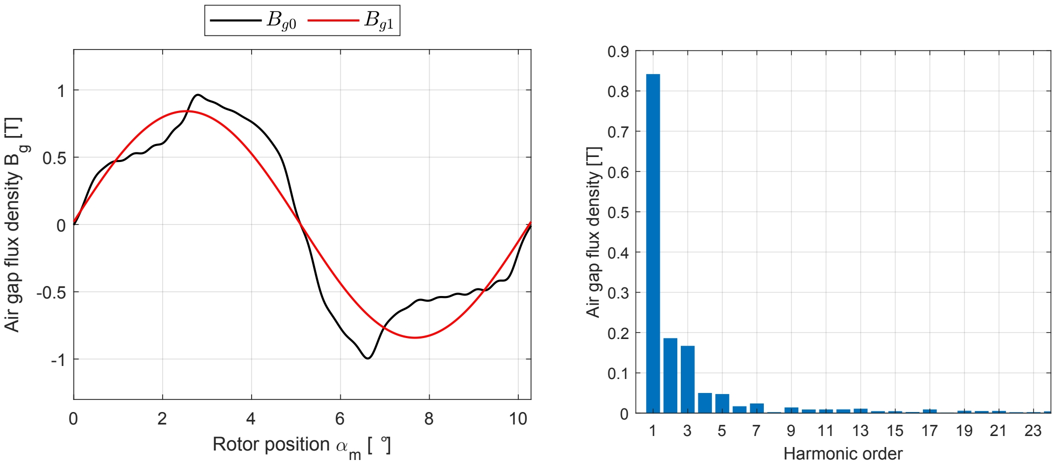

(a) (b)

Figure 4.21: No load induction **(a)** Zero and First order harmonics comparison **(b)** Harmonic spectrum

Through some iterations a design of the motor is carried out. In this case as well the focus is put on not getting too much saturation in the teeth and in the back iron to preserve the torque perfomance. The corresponding dimensions are displayed in Figure 4.7. Also in this case it can be appreciated a lower dimension of the stator teeth and of the external rotor back iron. The weight of the motor is displayed as well in Table 4.8.

In Figure 4.20 it is shown the FEA analysis both in no load and in FOC overload conditions.

In Figure 4.21 it is shown the no load air-gap flux density. As noticeable in Figure 4.21(a) it has a quite strange waveform because of the grill placed in the air-gap. In Figure 4.21(b) the Fourier analysis of the air-gap flux density is displayed. The most important thing though is that the amplitude of the first harmonic of the air-gap flux density is quite low. This may compromise the torque performance.

In Figure 4.22 it is shown the torque perfomance of the motor in both nominal and overload conditions. The nominal torque of 1270 MkI in FOC appears to be lower than it is in 1238 MkI without the flux modulator, with a peak value of 3.23 Nm.

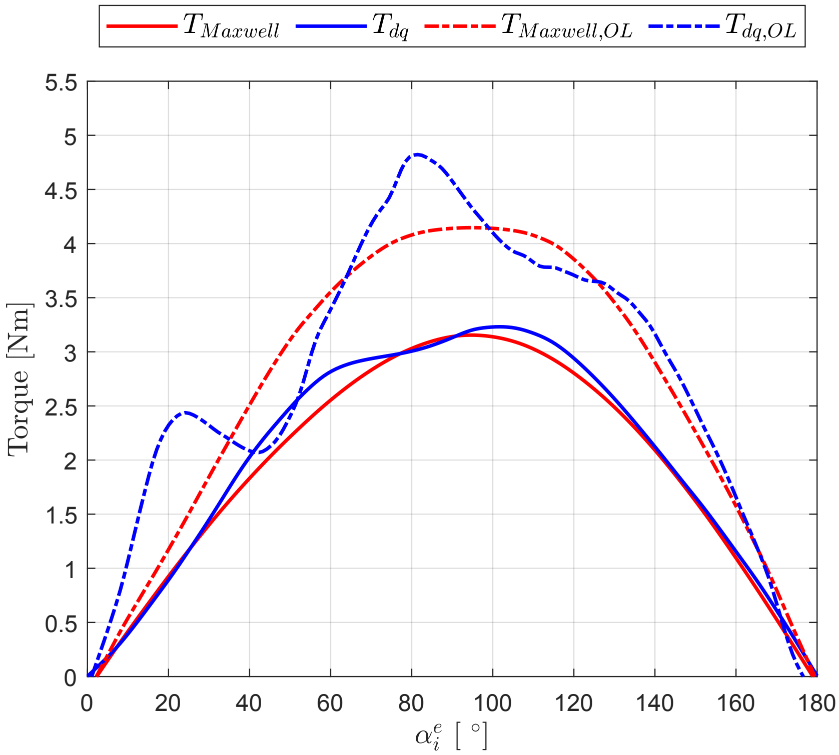

Figure 4.22: MTPA in nominal conditions and overload conditions

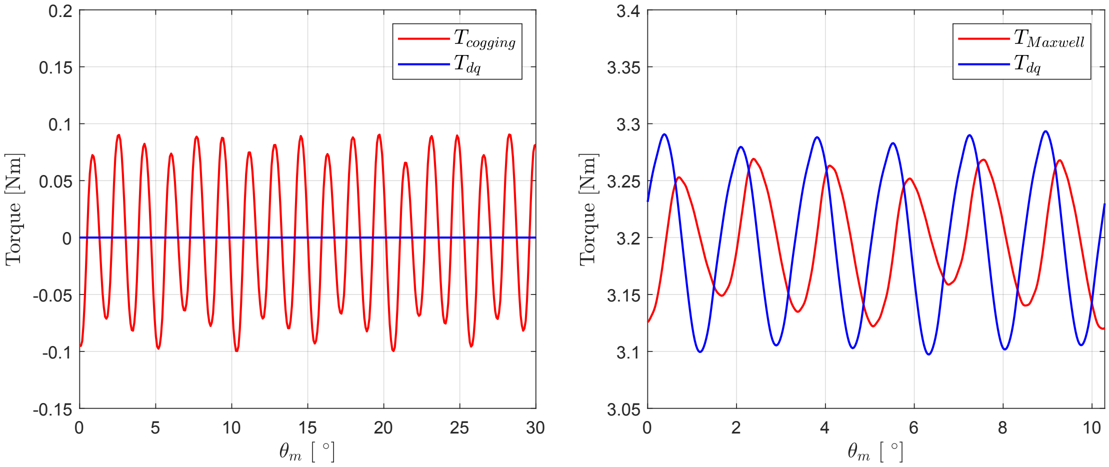

(a)

(b)

Figure 4.23: **(a)** Cogging torque **(b)** Torque ripple in nominal conditions

The torque to weight ratio is 3.51 $\frac{\text{Nm}}{\text{kg}}$. However, even with a low overload coefficient $k_{OL} = 2$, it can be seen that in overload conditions the motor shows a very high saturation. The saturation is so high that the motor reaches in overload conditions a torque value that is comparable to the nominal torque value of the 1238 MkI Vernier Motor. In Figure 4.23 the cogging torque and the torque ripple in nominal

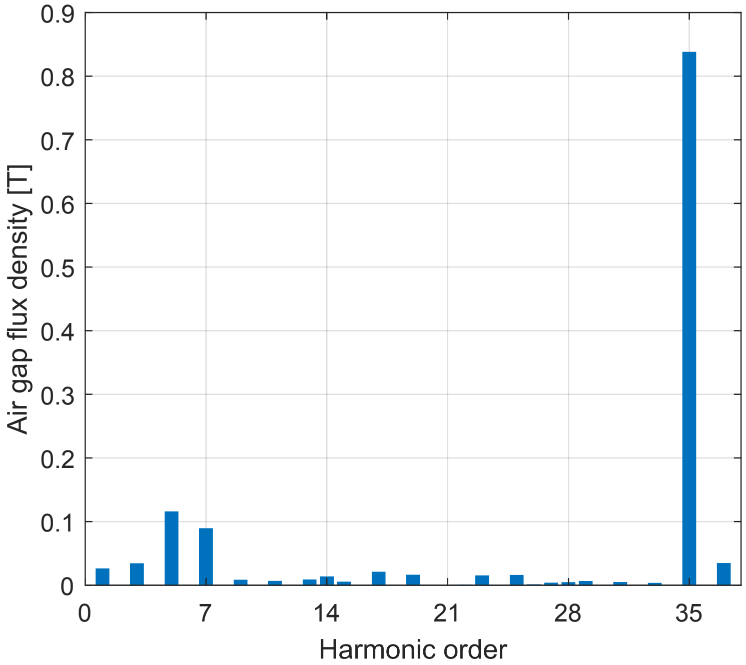

Figure 4.24: Harmonics and subharmonics of 1270 MkI in overload conditions

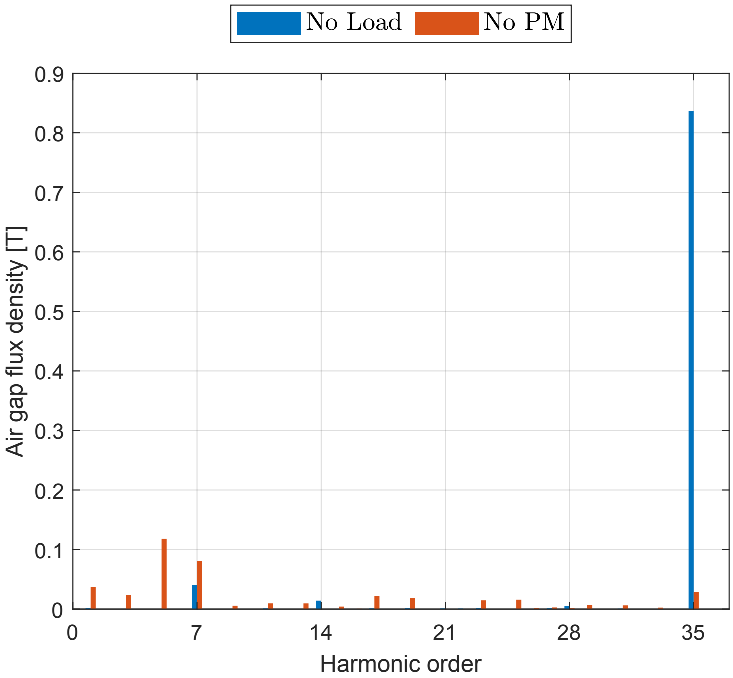

Figure 4.25: Harmonics and subharmonics of 1270 MkI in different electric and magnetic load conditions

conditions are shown, highlighting limited fluctuations.

To better understand the saturation problem a Fourier analysis of the FOC overload air-gap flux density is carried out and displayed in Figure 4.24. It is possible to detect an high amount of subharmonics with especially the one with $p = 5$ and the one with $p = 7$ quite relevant. It is possible to divide the effects of the magnetomotive force and of the magnets on the saturation of the machine as it is shown in Figure 4.18. In blue bars it can be seen the Fourier analysis of the air-gap flux density due to the magnets, instead in red bars it is shown the Fourier analysis of the air-gap flux density due to the electric loading of the machine.

4.3 Vernier Motors Comparison

It can be drawn a comparison of the designed Vernier Motors. In Figure 4.26 both nominal and overload mean torques of the Vernier Machines designed are shown. The nominal values are displayed in continuous lines and the overload values are displayed in dashed lines.

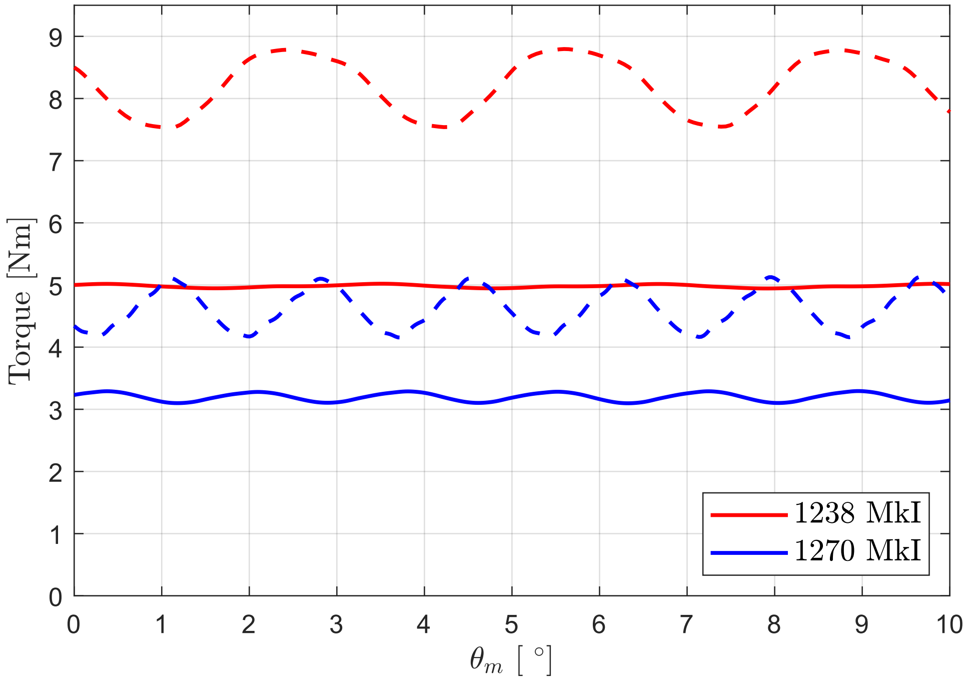

Figure 4.26: dq torque comparison of designed Vernier Outer Rotor Motors

Feature	**1238 MkI**	**1270 MkI**
Nominal Torque [Nm]	5	3.23
Overload Torque [Nm]	8.65	4.82
Weight [kg]	0.963	0.920
Torque to weight ratio $\left[\frac{\text{Nm}}{\text{kg}}\right]$	5.2	3.51
Volume [l]	0.212	0.212
Torque to volume ratio $\left[\frac{\text{Nm}}{l}\right]$	23.58	12.24
Nominal Ripple [%]	1.99	4.67

Table 4.9: Designed Vernier Outer Rotor Machines Comparison

In Figure 4.26 an high nominal torque and a corresponding low ripple for 1238 MkI can be noticed. In contrast, both nominal torque and torque ripple of 1270 MkI do not look satisfactory. The situation becomes even worse in the overload case. As it is shown, the overload torque of 1270 MkI does not even get to the nominal value of 1238 MkI, although their size and weight is comparable.

The reason why the 1270 MkI does not satisfy performance wise is probably related to the high air-gap, the small air-gap diameter and the low value of the first harmonic of no load air-gap flux density. These factors compromise the torque production and the easy saturation of this kind of motors worsen it.

However, the Vernier Machine without the modulator has great performance, with the highest torque to weight ratio and the lowest torque ripple so far.

4.4 Lightweight Vernier Motor Design

Also in this case a motor that allows to reduce axial size of the joint and its weight is designed. The usual configuration with 12 slots and 14 poles is taken and a Vernier Motor with 38 poles is derived from it. In a nutshell, the 1238 configuration of the previous Sections is resized using the Flipsky 6354 external diameter and reducing the stack size until torque requirements are reached.

Even in this case the high number of poles reduces the flux per pole and so it is possible to tighten the back iron and the rotor quite a lot. The results should be a very light motor.

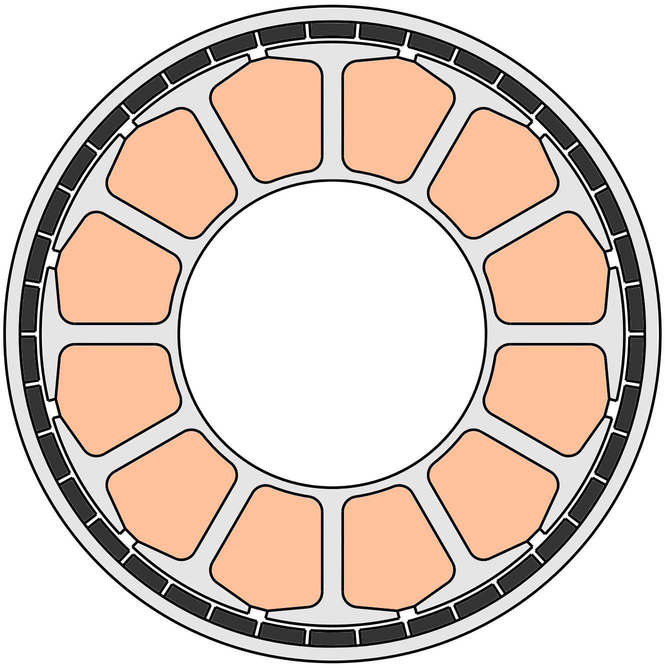

Figure 4.27: 1238 MkII drawing

D_e	D	w_t	h_s	h_{wed}	h_{so}	w_{so}	S_{slot}	L_{stk}
64 mm	57 mm	2 mm	12.5 mm	1.25 mm	0.75 mm	1.75 mm	102 mm^2	15 mm

Table 4.10: Stator dimensions of 1238 MkII

D_e	L_{stk}	G_{tot}
64 mm	15 mm	198.7 g

Table 4.11: Size of 1238 MkII

The motor, whose drawing is reported in Figure 4.27, is designed and the main dimensions are to be found in Table 4.10. The axial size and the weight, shown in

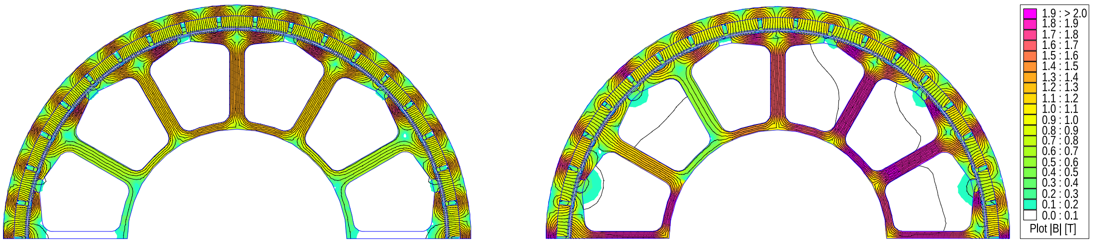

(a) (b)

Figure 4.28: FEA analysis **(a)** No load conditions **(b)** FOC Overload conditions

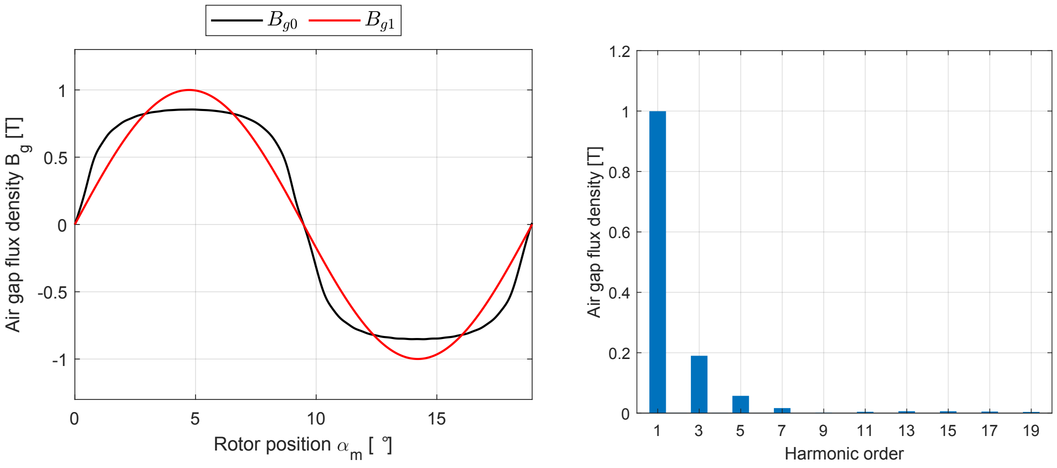

(a) (b)

Figure 4.29: No load induction **(a)** Zero and First order harmonics comparison **(b)** Harmonic spectrum

Table 4.11, are quite good with a very flat stack 15 mm long and with a weight of a bit less than 200 g.

In Figure 4.28 the FEA analysis of both no load and overload conditions of the designed Vernier Motor is displayed.

In Figure 4.29 the no load air-gap flux density is shown with the respective Fourier analysis as well. The fundamental harmonic has an amplitude of 1 T. Furthermore, in Figure 4.29(b) it can be noticed the total absence of even harmonics. It is due to the fact that a couple of poles of the rotor are less wide than a stator tooth, so the permeability is the same in the whole electric period and thus the teeth do not introduce any perturbation on the air-gap flux density.

The torque performance of the designed Vernier Motor is shown in Figure 4.30. As it can be seen the nominal torque requirement is met with a nominal torque value of 0.825 Nm, produced with an RMS current density of $J_N = 7.3\ \frac{\mathrm{A}}{\mathrm{mm}^2}$. The overload torque requirements are reached as well with an overload coefficient equal to $k_{OL} = 2$. The overload coefficient is higher than it was for the light SPM motor because, as it was shown in the previous Sections, this kind of machines suffer much saturation if the current is increased. In the overload torque curve, represented in Figure 4.30, this effect can be seen once again.

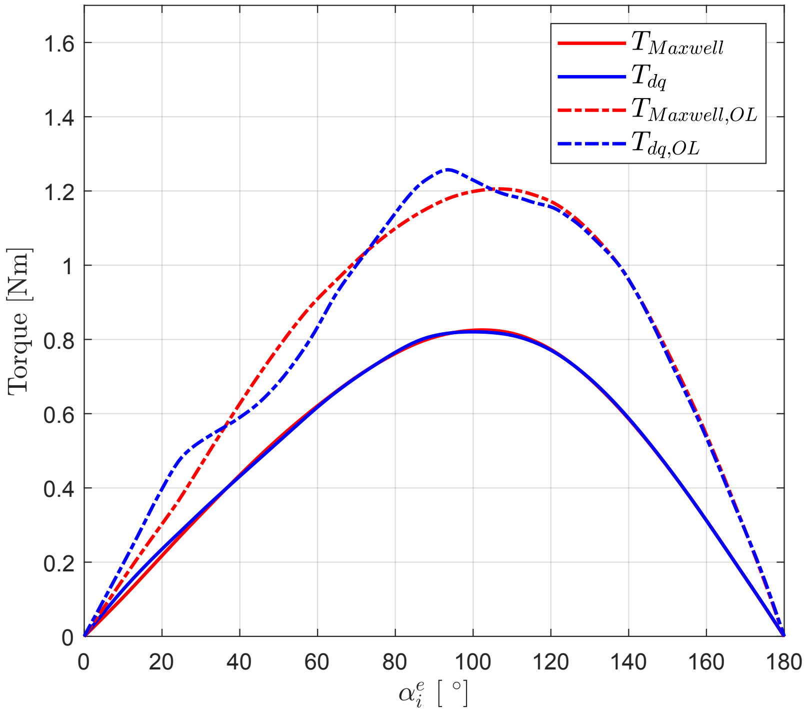

Figure 4.30: MTPA in nominal and overload conditions

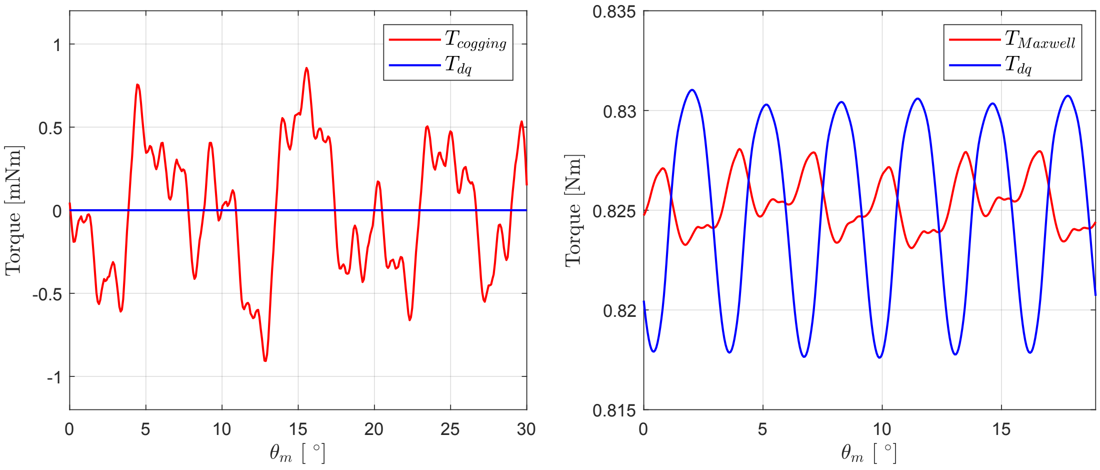

(a) (b)

Figure 4.31: **(a)** Cogging torque **(b)** Torque ripple in nominal conditions

In Figure 4.31(a) the cogging torque of 1238 MkII is reported. The amplitude of the cogging torque is equal to 0.0018 Nm which is 0.2% of the nominal torque. Instead, the torque ripple, displayed in Figure 4.31(b) has an amplitude of 0.005 Nm which

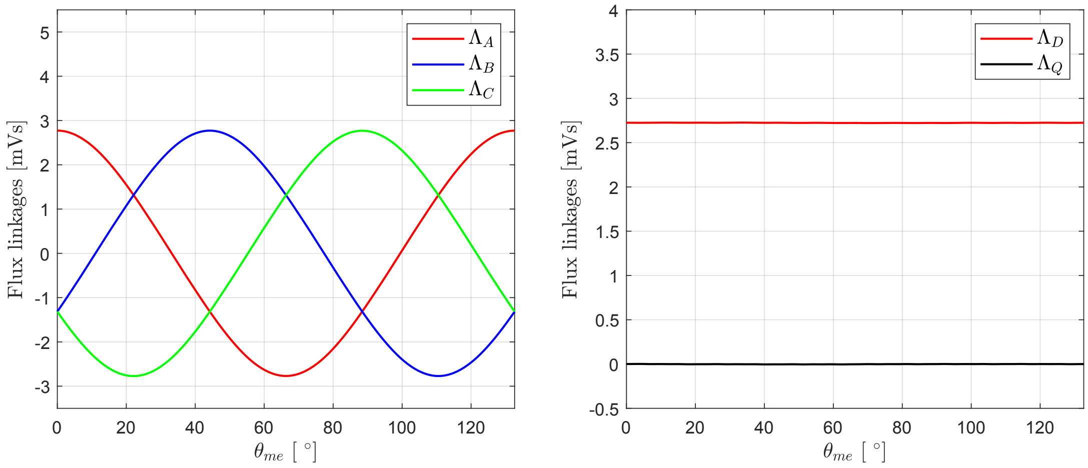

(a) (b)

Figure 4.32: No load fluxes **(a)** In abc reference **(b)** In dq reference

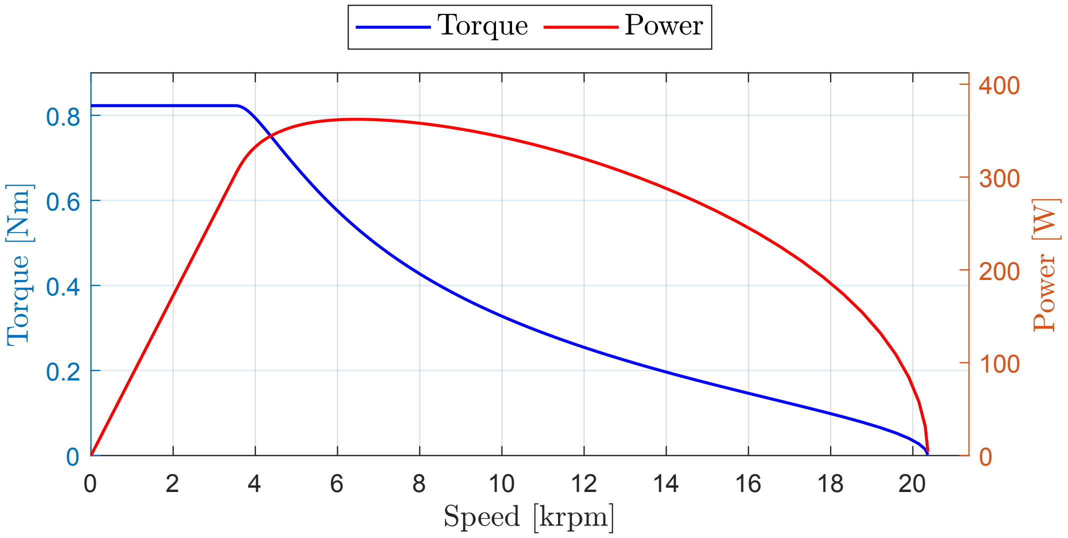

Figure 4.33: Mechanical characteristics reached in nominal current conditions

is equal to the 0.6% of the nominal torque.

For this motor as well a winding is designed to reach a base speed equal to 3500−3600 rpm. The selected condutors per slot are $n_c = 36$, without parallel paths. The no load flux linkages computed with the designed winding are shown in Figure 4.32. Thanks to the designed winding, the mechanical characteristics displayed in Figure 4.33 are reached. The base speed is around 3500 rpm, whereas the max speed is quite high and over 20000 rpm. This is probably due to the high saturation of the machine.

Conclusions

The aim of this work was to improve the design of an Electric Motor for Lower-Limb Exoskeleton. For this purpose, it was necessary to understand perfectly how the Exoskeleton had been designed.
In the first Chapter, the basics of Exoskeletons and their Joint Actuators are explained, including their applications, physical structure and relative engineering challenges.
The second Chapter focuses on the actual power propeller of the joint, which is the Electric Motor. Permanent Magnet Motors are described in detail, with their features, strengths and weaknesses. A basic analytical model, able to help the first sizing of the machine, and the winding design are described. Apart from traditional PM Machines, motors with magnetic gearing effect are introduced and their working principle is explained.
In the third Chapter the motor chosen to build the Exoskeleton is analyzed. Different dimentions and slot/pole configurations are designed and then analyzed. Although a good increase in torque to weight ratio is difficult to achieve, a great increase in torque to volume ratio can be reached and a possible change in the choice of the Mechanical Transmission is suggested.
In the fourth Chapter, motors with magnetic gearing effect are analyzed and designed. In the end they are compared to understand if their employment can provide an improvement to the Joint Actuator. The results are interesting since they show that Magnetically Geared Machines and Vernier Machines can increase the nominal torque of motors. However, they exhibit poor overload torque characteristics, due to the iron saturation caused by MMF subharmonics.
After analyzing different motor topologies, some configurations are selected because of their simple structure, size, weight and performance. The first motor is a 24 slots and 28 poles SPM motor. It features a low periodicity with a high pole number, decreasing the flux per pole and allowing to lighten the rotor and back-iron. The designed motor reaches the requirements described in Chapter 1 with an axial size of 20 mm, a total weight of 245 g and a low overload coefficient. Integrating this motor in the actuator should decrease the weight of a single joint of 24.4%, which means cutting 1.58 kg to the total joints weight. In addition, the axial size of the motor

would be 34 mm shorter, that is a reduction of 63% in respect with the previous motor and of 35.8% in respect with the previous total joint axial size.

The second motor selected as a good solution for such application is a Vernier Motor with the same winding characteristics of a 12 slots and 14 poles but with 38 rotor poles. Synchronizing on the right harmonic the motor can reach the torque requirements described in Chapter 1 with a stack length of 15 mm and a total motor weight of 198.7 g. Choosing this motor reduces the joint weight of 27.2% with an overall Exoskeleton weight reduction up to 1.76 kg. A reduction of 39 mm in axial length is achieved, which is a reduction of 73% circa of motor stack length and an overall axial length reduction of 41% in respect with the total joint axial length. The previously described results are also reported in Table 4.12.

Results	**Flipsky**	**2428 MkI**	**1238 MkII**
Motor axial size [mm]	54	20	15
Motor axial size reduction [%]	-	63	73
Joint axial size [mm]	95	61	56
Joint axial size reduction [%]	-	35.8	41
Weight [kg]	0.64	0.245	0.199
Joint weight [kg]	1.62	1.225	1.18
Joint weight reduction [%]	-	24.4	27.2

Table 4.12: Resulting Joint Actuator Sizes Comparison

The 1238 MkII Vernier Machine offers the best result in terms of weight and axial length reduction. However, it is characterized by a poor overload torque capability. The 24 slots - 28 poles SPM motor shows great results as well. With a simple Permanent Magnet Motor weight and axial length of the Joint Actuator can be reduced. This solution may be the best because the SPM Motor is reliable and has a very high torque density. This motor can be controlled with the same drive used for Flipsky 6354, adapting it to the new configuration. This motor shows great performance even in comparison with an another commercial motor usually chosen in this kind of applications which is Maxon EC60. 2428 MkI has lower axial length and weight and higher nominal output torque.

Future developments include the possibility of reducing rare earth materials volume in the motor. An Interior Permanent Magnet Motor may enhance the output torque, reducing magnet weight and therefore cost.

Furthermore, a more thorough analysis of Axial Flux Motors for this application can be carried out. In fact, their high power and torque density and especially their very flat layout may be optimal features for the Joint Actuator application.

Appendix A: Axial Flux Machines

Axial Flux Permanent Magnet (AFPM) Machines are Synchronous Machines whose working principle is the same of Radial Flux Permanent Magnet Machines. They are mainly divided in Slotless and Slotted Machines, as it is explained in [28]. Their main advantages are the high torque density, as it is shown in [29], and the possibility to put together more than one disk to increase torque, as it is shown in [28]. Among their drawbacks there are the attraction forces between rotor and stator that must be carefully analyzed and the design and manufacturing difficulties. In fact to design AF Machines time-consuming 3D simulations must be used, this is why focus of the research is usually on how to use analytical and 2D simulations to shorten the design process, as it can be read in [30] and [31], [32]. In [33] they looked when it is convenient to use AF Machines compared to RF Machines.
AF Machines have to be investigated as a concrete solution to the Exoskeleton Joint Actuator problem. Some analytical analysis are made for both a Slotless and a Slotted Machine.

Slotless Axial Flux Analytical Design

First of all a dimension is fixed for the motor in terms of diameter. An external radius of $R_e = 45$ mm and an internal one of $R_i = 20$ are chosen. A total diameter of the motor of $D = 100$ mm is chosen, considering also the end winding. The chosen number of poles is $2p = 12$. Usually the number of poles for this kind of motor is chosen respect to the number of coils with a 3/2 or 3/4 configuration, meaning 2 or 4 Permanent Magnets for every 3 coils. So the final chosen configuration is 18 coils and 12 poles.

$$\alpha_{pm} = \frac{360°}{2p} = \frac{360°}{12} = 30°$$
$$h_{pm} = \frac{\pi \cdot D_i}{2p} = \frac{\pi \cdot 40}{12} = 10.47 \text{ mm}$$

The coil width must be shorter than the minimum width of the pole, this is why $h_{bob} = 10$ mm is chosen. The air-gap flux density is computed using the Permanent

Magnet thickness t_m and the equivalent air-gap g:

$$B_{g0} = \frac{B_{rem}}{1 + \frac{\mu_{rec} g}{t_m}} = \frac{1.2}{1 + \frac{1.05 \cdot 6}{6}} = 0.58 \text{ T}$$

At this point, using the height of the coil h_{bob} and the width of the coil w_{bob} it is possible to compute the copper section:

$$S_{bob} = h_{bob} \cdot w_{bob} = 10 \cdot 4 = 40 \text{ mm}^2$$
$$S_{cu} = k_{fill} \cdot S_{bob} = 0.6 \cdot 40 = 24 \text{ mm}^2$$

With a current density of $J = 8 \, \frac{\text{A}}{\text{mm}^2}$ it is possible to compute the coil current:

$$I_{bob} = J \cdot S_{cu} = 8 \cdot 36 = 388 \text{ A}$$

And then the magnetic force on one coil, that with the force radius allows to compute the total torque of the motor as:

$$F_1 = I_{bob} \cdot B_{g0} \cdot L = 288 \cdot 0.58 \cdot 0.025 = 4.176 \text{ N}$$
$$F_{tot} = 2p \cdot F_1 = 12 \cdot 4.176 = 50 \text{ N}$$
$$T_{tot} = F_{tot} \cdot R_{avg} = 50 \cdot 0.0325 = 1.6 \text{ Nm}$$

Using as an approximated density the mean value of the iron, copper and Permanent Magnets it is possible to estimate a rough weight of:

$$G_{tot} \simeq 0.65 \text{ kg}$$

Slotted Axial Flux Analytical Design

Starting from the slotless motor dimensions a design of a slotted motor is done. So the external radius is $R_e = 45$ mm and the internal one is $R_i = 20$ mm are chosen. The rotor and stator back irons are chosen as $h_{bi,r} = h_{bi,s} = 5$ mm. The slot width is $w_s = 5$ mm as it was computed before from the minimum width of the magnet. The slot heigth chosen is $h_s = 15$ mm. The air-gap flux density is computed choosing the magnet thickness t_m and an air-gap diameter g.

$$B_{g0} = \frac{B_{rem}}{1 + \frac{\mu_{rec} g}{t_m}} = \frac{1.2}{1 + \frac{1.05 \cdot 1}{6}} = 1 \text{ T}$$

From the slot dimentions it can be computed the copper section in each slot as:

$$\begin{aligned} S_{slot} &= h_s \cdot w_s = 15 \cdot 5 = 75 \text{ mm}^2 \\ S_{cu} &= k_{fill} \cdot S_{slot} = 0.4 \cdot 75 = 30 \text{ mm}^2 \end{aligned}$$

With a current density of $J = 8 \ \frac{\text{A}}{\text{mm}^2}$, it can be computed the slot current:

$$I_{slot} = J \cdot S_{cu} = 8 \cdot 30 = 240 \text{ A}$$

The force on each coil and on the total rotor is:

$$\begin{aligned} F_1 &= B_{g0} \cdot I_{slot} \cdot L = 1 \cdot 240 \cdot 0.025 = 6 \text{ N} \\ F_{tot} &= 2p \cdot F_1 = 12 \cdot 6 = 72 \text{ N} \end{aligned}$$

Then, computing the mean radius of the machine it is possible to compute the torque:

$$\begin{aligned} R_{avg} &= \frac{R_e + R_i}{2} = \frac{45 + 20}{2} = 32.5 \text{ mm} \\ T &= R_{avg} \cdot F_{tot} = 0.0325 \cdot 72 = 2.34 \text{ Nm} \end{aligned}$$

It can also be computed an approximated weight analysis of the motor such as:

$$\begin{aligned} V_{tot} &= \frac{\pi}{4} \cdot (D_e^2 - D_i^2) \cdot L_{stk} = \frac{\pi}{4}(0.09^2 - 0.04^2) \cdot 0.032 = 163 \times 10^{-6} \text{ m}^3 \\ G_{tot} &= \gamma \cdot V_{tot} \simeq 1.3 \text{ kg} \end{aligned}$$

Appendix B: Materials

$B\,[\mathrm{T}]$	P_s at 50 Hz $\left[\frac{\mathrm{W}}{\mathrm{kg}}\right]$	P_s at 200 Hz $\left[\frac{\mathrm{W}}{\mathrm{kg}}\right]$
1	2.44	13.22
1.5	4.53	32.63
1.7	5.94	43.93

Iron M530 50A specific losses for 0.50 mm metal sheet

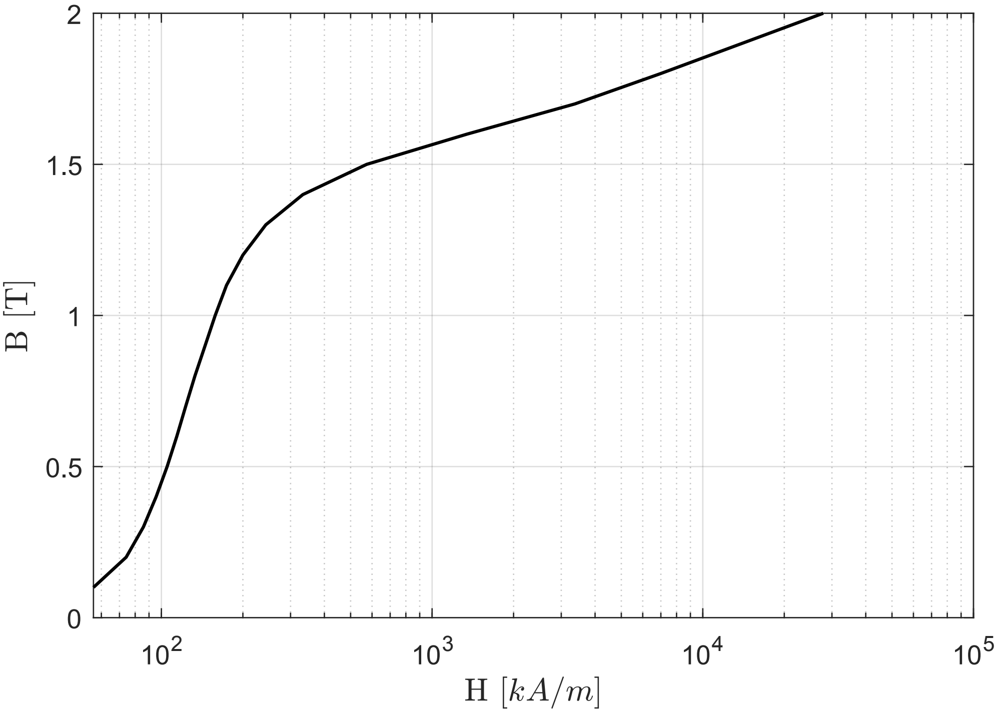

BH curve of iron M530 50A

Properties		**N42SH**
Magnetic	Unit	Value
Residual induction B_{rem}	$[\mathrm{T}]$	1.31
Coercivity H_{cb}	$\left[\frac{\mathrm{kA}}{\mathrm{m}}\right]$	987
Intrinsic coercivity H_{cj}	$\left[\frac{\mathrm{kA}}{\mathrm{m}}\right]$	1592
Maximum energy product BH_{max}	$\left[\frac{\mathrm{kJ}}{\mathrm{m}^3}\right]$	330
Thermal	Unit	Value
$\frac{\Delta B_{rem}}{\Delta T}$	$\left[\frac{\%}{^\circ\mathrm{C}}\right]$	-0.12
$\frac{\Delta H_{cj}}{\Delta T}$	$\left[\frac{\%}{^\circ\mathrm{C}}\right]$	-0.55
Curie Temperature	$[^\circ\mathrm{C}]$	310

NdFeB N42SH features

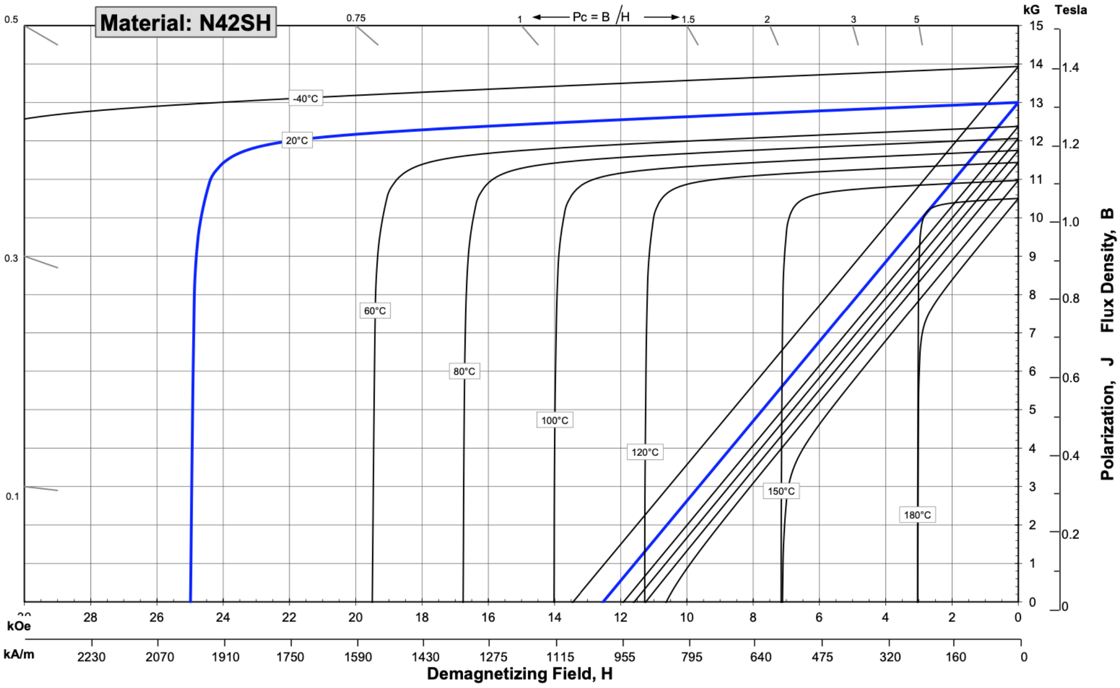

Bibliography

[1] Anthony Goo, Curt A. Laubscher, Ryan J. Farris, and Jerzy T. Sawicki. Design and evaluation of a pediatric lower-limb exoskeleton joint actuator. *Actuators*, 9(4), 2020. ISSN 2076-0825. doi: 10.3390/act9040138. URL `https://www.mdpi.com/2076-0825/9/4/138`.

[2] Ting Zhang and He Huang. A lower-back robotic exoskeleton: Industrial handling augmentation used to provide spinal support. *IEEE Robotics and Automation Magazine*, 25(2):95–106, 2018. doi: 10.1109/MRA.2018.2815083.

[3] Max K. Shepherd and Elliott J. Rouse. Design and validation of a torque-controllable knee exoskeleton for sit-to-stand assistance. *IEEE/ASME Transactions on Mechatronics*, 22(4):1695–1704, 2017. doi: 10.1109/TMECH.2017.2704521.

[4] Rachel L. Hybart and Daniel P. Ferris. Embodiment for robotic lower-limb exoskeletons: A narrative review. *IEEE Transactions on Neural Systems and Rehabilitation Engineering*, 31:657–668, 2023. doi: 10.1109/TNSRE.2022.3229563.

[5] Amy D. Gardner, Johan Potgieter, and Frazer K. Noble. A review of commercially available exoskeletons' capabilities. In *2017 24th International Conference on Mechatronics and Machine Vision in Practice (M2VIP)*, pages 1–5, 2017. doi: 10.1109/M2VIP.2017.8211470.

[6] Anthony Goo, Curt A. Laubscher, Ryan J. Farris, and Jerzy T. Sawicki. Design and evaluation of a pediatric lower-limb exoskeleton joint actuator. *Actuators*, 9(4), 2020. ISSN 2076-0825. doi: 10.3390/act9040138. URL `https://www.mdpi.com/2076-0825/9/4/138`.

[7] David Eguren, Manuel Cestari, Trieu Phat Luu, Atilla Kilicarslan, Alexander Steele, and Jose L. Contreras-Vidal. Design of a customizable, modular pediatric exoskeleton for rehabilitation and mobility. In *2019 IEEE International Conference on Systems, Man and Cybernetics (SMC)*, pages 2411–2416, 2019. doi: 10.1109/SMC.2019.8914629.

[8] Luca Bizzotto. *Study and mechatronic design of a powered lower limb exoskeleton*. PhD thesis, Politecnico di Torino, 2023.

[9] Volker Bartenbach, Marcel Gort, and Robert Riener. Concept and design of a modular lower limb exoskeleton. In *2016 6th IEEE International Conference on Biomedical Robotics and Biomechatronics (BioRob)*, pages 649–654, 2016. doi: 10.1109/BIOROB.2016.7523699.

[10] N. Bianchi, S. Bolognani, M.D. Pre, and G. Grezzani. Design considerations for fractional-slot winding configurations of synchronous machines. *IEEE Transactions on Industry Applications*, 42(4):997–1006, 2006. doi: 10.1109/TIA.2006.876070.

[11] A. El-Refaie. Fractional-slot concentrated-windings: A paradigm shift in electrical machines. In *2013 IEEE Workshop on Electrical Machines Design, Control and Diagnosis (WEMDCD)*, pages 24–32, 2013. doi: 10.1109/WEMDCD.2013.6525162.

[12] Luigi Alberti and Nicola Bianchi. Theory and design of fractional-slot multilayer windings. *IEEE Transactions on Industry Applications*, 49(2):841–849, 2013. doi: 10.1109/TIA.2013.2242031.

[13] P. M. Tlali, R-J. Wang, and S. Gerber. Magnetic gear technologies: A review. In *2014 International Conference on Electrical Machines (ICEM)*, pages 544–550, 2014. doi: 10.1109/ICELMACH.2014.6960233.

[14] Stiaan Gerber and Rong-Jie Wang. Design and evaluation of a magnetically geared pm machine. *IEEE Transactions on Magnetics*, 51(8):1–10, 2015. doi: 10.1109/TMAG.2015.2421474.

[15] C. H. Lee. Vernier motor and its design. *IEEE Transactions on Power Apparatus and Systems*, 82(66):343–349, 1963. doi: 10.1109/TPAS.1963.291362.

[16] Yue Liu and Z. Q. Zhu. Comparative study of magnetic gearing effect in integral slot, fractional slot winding and vernier pm machines. In *2017 20th International Conference on Electrical Machines and Systems (ICEMS)*, pages 1–6, 2017. doi: 10.1109/ICEMS.2017.8056384.

[17] Kangfu Xie, Dawei Li, Ronghai Qu, Xiang Ren, Manoj R. Shah, and Yuan Pan. A new perspective on the pm vernier machine mechanism. *IEEE Transactions on Industry Applications*, 55(2):1420–1429, 2019. doi: 10.1109/TIA.2018.2880144.

[18] Chiara Contò and Nicola Bianchi. A guideline for selecting motors for electric bikes based on magnetic analysis and measurements. *IEEE Transactions on Energy Conversion*, pages 1–10, 2023. doi: 10.1109/TEC.2023.3297844.

[19] Enrico Carraro, Nicola Bianchi, Sunny Zhang, and Matthias Koch. Design and performance comparison of fractional slot concentrated winding spoke type synchronous motors with different slot-pole combinations. *IEEE Transactions on Industry Applications*, 54(3):2276–2284, 2018. doi: 10.1109/TIA.2018.2807382.

[20] Chiara Contò and Nicola Bianchi. Overload capability test of a permanent magnet synchronous motor for e-bike application. In *2023 IEEE International Electric Machines & Drives Conference (IEMDC)*, pages 1–7, 2023. doi: 10.1109/IEMDC55163.2023.10238908.

[21] Yeji Park, Hyunwoo Kim, Hyungkwan Jang, Sang-Hawn Ham, Ju Lee, and Dong-Hoon Jung. Efficiency improvement of permanent magnet bldc with halbach magnet array for drone. *IEEE Transactions on Applied Superconductivity*, 30(4):1–5, 2020. doi: 10.1109/TASC.2020.2971672.

[22] R. P. Praveen, M. H. Ravichandran, V. T. Sadasivan Achari, V. P. Jagathy Raj, G. Madhu, and G. R. Bindu. A novel slotless halbach-array permanent-magnet brushless dc motor for spacecraft applications. *IEEE Transactions on Industrial Electronics*, 59(9):3553–3560, 2012. doi: 10.1109/TIE.2011.2161058.

[23] Xintong Zhang, Chengming Zhang, Jikun Yu, Pengcheng Du, and Liyi Li. Analytical model of magnetic field of a permanent magnet synchronous motor with a trapezoidal halbach permanent magnet array. *IEEE Transactions on Magnetics*, 55(7):1–5, 2019. doi: 10.1109/TMAG.2019.2902988.

[24] Shuangyue Yu, Tzu-Hao Huang, Xiaolong Yang, Chunhai Jiao, Jianfu Yang, Yue Chen, Jingang Yi, and Hao Su. Quasi-direct drive actuation for a lightweight hip exoskeleton with high backdrivability and high bandwidth. *IEEE/ASME Transactions on Mechatronics*, 25(4):1794–1802, 2020. doi: 10.1109/TMECH.2020.2995134.

[25] Dawei Li, Tianjie Zou, Ronghai Qu, and Dong Jiang. Analysis of fractional-slot concentrated winding pm vernier machines with regular open-slot stators. *IEEE Transactions on Industry Applications*, 54(2):1320–1330, 2018. doi: 10.1109/TIA.2017.2778686.

[26] Tianjie Zou, Ronghai Qu, Dawei Li, and Dong Jiang. Synthesis of fractional-slot vernier permanent magnet machines. In *2016 XXII International Conference on Electrical Machines (ICEM)*, pages 911–917, 2016. doi: 10.1109/ICELMACH.2016.7732634.

[27] Ken Chen and Bulent Sarlioglu. Vernier machine analysis and analytical design for traction applications. In *2021 International Aegean Conference on Electrical Machines and Power Electronics (ACEMP) & 2021 International Conference on Optimization of Electrical and Electronic Equipment (OPTIM)*, pages 426–431, 2021. doi: 10.1109/OPTIM-ACEMP50812.2021.9590078.

[28] Rundong Huang, Zaixin Song, Hang Zhao, and Chunhua Liu. Overview of axial-flux machines and modeling methods. *IEEE Transactions on Transportation Electrification*, 8(2):2118–2132, 2022. doi: 10.1109/TTE.2022.3144594.

[29] A. Di Gerlando, G. Foglia, and C. Ricca. Analytical design of a high torque density in-wheel yasa afpm motor. In *2020 International Conference on Electrical Machines (ICEM)*, volume 1, pages 402–408, 2020. doi: 10.1109/ICEM49940.2020.9270998.

[30] Maarten J. Kamper, Rong-Jie Wang, and Francois G. Rossouw. Analysis and performance of axial flux permanent-magnet machine with air-cored nonoverlapping concentrated stator windings. *IEEE Transactions on Industry Applications*, 44(5):1495–1504, 2008. doi: 10.1109/TIA.2008.2002183.

[31] Asko Parviainen et al. Design of axial-flux permanent-magnet low-speed machines and performance comparison between radial-flux and axial-flux machines. 2005.

[32] A. Parviainen, M. Niemela, and J. Pyrhonen. Modeling of axial flux permanent-magnet machines. *IEEE Transactions on Industry Applications*, 40(5):1333–1340, 2004. doi: 10.1109/TIA.2004.834086.

[33] A. Cavagnino, M. Lazzari, F. Profumo, and A. Tenconi. A comparison between the axial flux and the radial flux structures for pm synchronous motors. *IEEE Transactions on Industry Applications*, 38(6):1517–1524, 2002. doi: 10.1109/TIA.2002.805572.